

RICE UNIVERSITY

**Surface Studies of C₆₀ on Ferromagnetic Ni/Cu(100) and Co/Ru(0001)
Thin Film Systems**

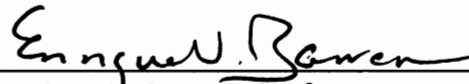
By

Marvin L. Cummings Jr.

A THESIS SUBMITTED
IN PARTIAL FULFILLMENT OF THE
REQUIREMENTS FOR THE DEGREE

Doctor of Philosophy

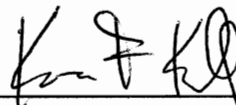
APPROVED, THESIS COMMITTEE:



Dr. Enrique V. Barrera, Professor
Mechanical Engineering & Materials Science
Rice University



Dr. Eric I. Altman, Professor
Chemical & Environmental Engineering
Yale University



Dr. Kevin Kelly, Associate Professor
Electrical and Computer Engineering
Rice University



Dr. Jun Lou, Assistant Professor
Mechanical Engineering & Materials Science
Rice University

HOUSTON, TEXAS
November 2010

Abstract

Surface Studies of C₆₀ on Ferromagnetic Ni/Cu(100) and Co/Ru(0001)

Thin Film Systems

By

Marvin L. Cummings Jr.

This dissertation determined how the electronic and atomic structure of Ni/Cu(100) and Co/Ru(0001) thin films affect C₆₀-metal bonding and local magnetic properties at the surface. In-situ spin-averaged and spin-polarized scanning tunneling microscopy and spectroscopy techniques were used in this study. Homoepitaxial growth studies of Ni(100) and Co(0001) films investigated the influence of C₆₀ on film growth. On 7.6 ML Ni films, C₆₀ showed no obvious effect on the continued crystalline growth of Ni. The low mobility of C₆₀ on the Ni surface and high Ni diffusion barrier limited the occurrence of Ni-C₆₀ collisions during growth. On 1.84 ML Co films, crystalline growth with moiré reconstructions continued with C₆₀ present at the surface. However, Co islands were observed only nucleating and growing from step edges and around C₆₀ suggesting the Co-C₆₀ bond is stronger than the Co-Co bond on Co terraces. C₆₀ mobility was also observed to vary across the Co film surface due to local variations in film reconstruction and dislocation networks. The results show that the nature of the C₆₀-metallic bond at the surface can effect film growth and morphology.

Scanning tunneling spectroscopy (STS) studies suggest that the spin-averaged and spin-polarized Co(0001) electronic structure is influenced by a number of factors: (i) sequential layer stacking (fcc/hcp), (ii) strain-induced reconstruction (moiré), (iii) Co film thickness, and (iv) dislocations and defects at the surface. Spin-polarized STS measurements resolved spectral contributions from Co layer stacking and opposite perpendicular magnetic spin-orientations. The magnetic domain regions identified were fcc $\uparrow\uparrow$ /fcc $\uparrow\downarrow$ and hcp $\uparrow\uparrow$ /hcp $\uparrow\downarrow$ stacked domains, respectively. No evidence of an in-plane magnetic spin-orientation or spin re-orientation transition was observed at the Co surface; however magnetic domain walls showed evidence of pinning at dislocation lines. Spin-polarized STM/STS measurements did not reveal any affect of C₆₀ on the local magnetic properties of Co. However, an internal structure of C₆₀ molecules adsorbed on the Co(0001) film surface was observed, corresponding to a 3-fold (symmetry) molecular-orientation; and in the near-region where C₆₀ clusters were adsorbed, Co surface state peaks were observed to be absent, suggesting the local electronic structure of Co is perturbed by the presence of C₆₀.

Acknowledgements

I would like to start by thanking the many wonderful people who have made my journey possible. To my advisor Dr. Enrique V. Barrera and Committee members, to Dr. Eric Altman, Dr. Matthias Bode, and Dr. Volker Rose, thank you for your earnest dedication and support of my professional development and research. To the Alliances for Graduate Education and the Professoriate (AGEP), Rice University, thank you for providing me with a community of support. To family and friends who have walked with me, stood with me and held up my spirit on this journey, I dedicate this work to and for you.

Table of Contents

CHAPTER 1: Introduction.....	1
CHAPTER 2: Experimental Background and Theory.....	7
2.1 STM.....	7
2.1.1 STM Theory.....	8
2.1.2 Spin-Polarized STM Theory.....	10
2.2 Co(0001) Electronic Structure.....	13
2.2.1 Magnetic Moment of Co.....	13
2.2.2 Magnetic Orientation of Co Films.....	14
2.2.3 Surface State Electronic Structure of Co Films.....	16
2.3 The C ₆₀ Fullerene's Physical & Electronic Properties and Interactions with Metallic Surface.....	19
2.3.1 Chemical Interactions of C ₆₀ at Metal Surfaces.....	20
2.3.2 The Ordering of C ₆₀ at the Surface of Metals.....	25
2.3.3 Resonant Tunneling Mechanism for Molecular Adsorbates.....	30
CHAPTER 3: Influence of Molecular C ₆₀ on Ni(100) and Co(0001) Film Growth.....	37
3.1 Introduction.....	37
3.2 Experimental Procedures.....	38
3.3 Results & Discussion.....	41

3.3.1 Sub-ML C ₆₀ coverage on annealed Ni(100) Films.....	41
3.3.2 Ni Island Growth with 0.03 (Low) C ₆₀ Coverage.....	44
3.3.3 Auger Spectral Analysis of Ni Growth.....	48
3.3.4 Co Film Growth & Morphology on Ru (0001) Substrate.....	50
3.3.5 Sub-ML C ₆₀ coverage on annealed Co(0001) Films.....	56
3.3.6 Co Island Growth with Low C ₆₀ Coverage.....	60
3.4 Summary.....	64

CHAPTER 4: Spin-Average & Spin-Polarized Scanning Tunneling Microscopy /

Spectroscopy of Bare Co Films & C₆₀-Adsorbed Co Films Grown on

Ru(0001).....	66
4.1 Introduction.....	66
4.2 Experimental.....	67
4.3 Results and Discussion.....	68
4.3.1 Co(0001) Film Growth & Morphology.....	68
4.3.2 Spin-Average Electronic Structure of Co Films on Ru(0001)	69
4.3.2.1 Spin-Polarized Electronic Structure of Co Films on	
Ru(0001) Results.....	74
4.3.2.2 Spin-Polarized Electronic Structure of Co Films on	
Ru(0001) Discussion.....	90
4.4 Summary.....	92

CHAPTER 5: Spin-Averaged & Spin-Polarized STM Studies of Molecular C ₆₀ on	
Co/Ru(0001).....	93
5.1 Spin-Averaged Intra-Molecular Structure of C ₆₀ on Co.....	93
5.2 Molecular C ₆₀ Spin-Polarized Interactions with Co(0001)	94
5.3 Summary.....	102
CHAPTER 6: Conclusions.....	103
REFERENCES.....	106
Appendix A.....	116
Appendix B.....	117
Appendix C.....	122
Appendix D.....	124

List of Tables

Table 3.1. C ₆₀ C-peak position and height.....	49
Table 4.1. Summary of SP- <i>dI/dV</i> Results (Fe-coated tip).....	89

List of Figures

Figure 1.1. Images highlighting technological innovations of hard drives.....	1
Figure 1.2. SEM image of right/left Ni electrodes.....	2
Figure 1.3. TEM of T7 bacteriophage.....	5
Figure 2.1. Scanning tunneling microscope (STM) device.....	7
Figure 2.2. (a) Bulk electronic structure of Co(0001).....	17
Figure 2.3. Diagram comparing the electronic DOS of Ni(110).....	23
Figure 2.4. A 183Å × 196Å STM topograph of C ₆₀ -induced reconstruction on the Ni(110).....	25
Figure 2.5. Energy diagram and atomic structures showing the motion of an adsorbate.....	29
Figure 2.6. STM image of C ₆₀ molecules at the surface of Cu(111).....	31
Figure 2.7. Diagram showing MO contribution to tunneling.....	32
Figure 2.8. Tunneling (transmission) resonances of Au-C ₆₀ -Au.....	33
Figure 2.9. STM images of C ₆₀ on the Si(111)(7×7).....	34
Figure 2.10. In STM topograph, two Gd@C ₈₂ molecules.....	36
Figure 3.1. Topograph of (a,c) of Cu(100) and Ru(0001) substrate surfaces.....	40
Figure 3.2. (a) Topograph of pre-annealed 7.6 ML Ni film.....	41

Figure 3.3. Topograph of 0.03 ML C ₆₀ adsorbed onto an annealed Ni(100).....	42
Figure 3.4. Topograph of (a) 0.03 ML C ₆₀ on Ni(100) film surface after depositing.....	45
Figure 3.5. Topograph of (a) C ₆₀ on Ni(100) film surface after depositing – sequential line section.....	46
Figure 3.6. Topograph (200 Å × 400 Å) of 3.8 ML Ni grown 0.2 ML C ₆₀ pre-covered Ni(100) film surface	47
Figure 3.7. AES plots showing shifts in C ₆₀ C-peak as 1 to 3 ML Ni.....	49
Figure 3.8. Topograph of the pre-annealed Co(0001) film.....	50
Figure 3.9. Topography of 3rd-ML Co terrace with moiré reconstruction.....	54
Figure 3.10. Topograph of 1.84 ML Co film annealed at 660 K.....	55
Figure 3.11. Topograph of 0.04 ML C ₆₀ deposited onto an annealed Co(0001).....	57
Figure 3.12. Topograph of non-uniform C ₆₀ distribution on Co(0001).....	58
Figure 3.13. Topograph of 0.23 ML Co deposited on C ₆₀ pre-covered annealed Co film surface.....	61
Figure 3.14. Topograph of large Co islands with {111}, {100} step edge microfacets...	62
Figure 3.15. Topograph of Co film surface after 1.6 ML Co deposited.....	63
Figure 4.1. STM topographs of post-annealed Co films grown at (a) RT and (b) 77 K...	68
Figure 4.2. (a) Topograph of the pre-annealed Co(0001).....	69
Figure 4.3. (a) Spin-averaged <i>dI/dV</i> -map of hcp and fcc regions on Co surface.....	70
Figure 4.4. (a) 250nm×250nm STM topograph of post-annealed Co grown at 77 K.....	74
Figure 4.5. Spin-Polarized <i>dI/dV</i> -map of hcp _{↑↓} (hcp _{↑↑}) regions on Co surface.....	77
Figure 4.6. Topograph of atomically-flat 2 ML Co terrace across substrate step.....	79

Figure 4.7. Spin-polarized dI/dV -map of $hcp_{\uparrow\downarrow} / hcp_{\uparrow\uparrow}$ region on Co surface near a dislocations.....	81
Figure 4.8. Spin-Polarized dI/dV -map of $fcc_{\uparrow\downarrow}(fcc_{\uparrow\uparrow})$ region on Co surface.....	84
Figure 4.9. Spatially-averaged spin-polarized dI/dV -curves taken from $fcc_{\uparrow\uparrow}$ region on Co surface across 2,3-ML substrate step.....	86
Figure 4.10. dI/dV -map of a dark contrast hcp region on Co surface.....	87
Figure 4.11. 250nm×250nm spin-polarized dI/dV -map of 1.84 ML post-annealed Co(0001) film.....	88
Figure 4.12. Fourier Transform taken from (b) moiré pattern.....	91
Figure 5.1. Intramolecular structure of C_{60} on Co(0001) surface.....	93
Figure 5.2. Topograph of C_{60} clusters deposited to Co substrate below room temperature.....	95
Figure 5.3. (a) Topograph showing C_{60} atop 3 ML fcc region on the Co.....	96
Figure 5.4. Contour plot of dI/dV -curves from line section taken across C_{60} cluster atop a $fcc_{\uparrow\downarrow}$ region on Co film.....	98
Figure 5.5. Spin-polarized conductance (dI/dV) curves from $fcc_{\uparrow\downarrow}$ region	100
Figure 5.6. Spin-polarized spectral-maps (at different V_b) of C_{60} atop $fcc_{\uparrow\downarrow}$ and $fcc_{\uparrow\uparrow}$ regions on the Co(0001) film.....	101

CHAPTER 1: INTRODUCTION

Fullerene-based metallic nanosystems show great potential for application in next generation technologies, such as field-effect transistor (FET) devices and spintronic devices which take advantage of the electron's spin degree of freedom.[1,2,3,4,5]

Today, as short-channel leakage current effects are limiting the utility of semiconductor

based transistor devices and

as superparamagnetic

effects are limiting hard

drive data storage capacity,

these fullerene-based

nanosystems offer a unique

alternative due to their

functionality at small

dimensions. However as the

dimensions (surface-to-volume ratio) of these devices become increasingly smaller

down to the nanoscale, the properties and functionality of these devices become ever

more dependent on interface and surface effects.

Planar tunneling magnetoresistance (TMR) junction devices (shown in figure 1.1) are a good example. These devices are used to retrieve magnetically-stored information from hard drives and operate on the simple principle of magnetic alignment.[6,7] In TMR

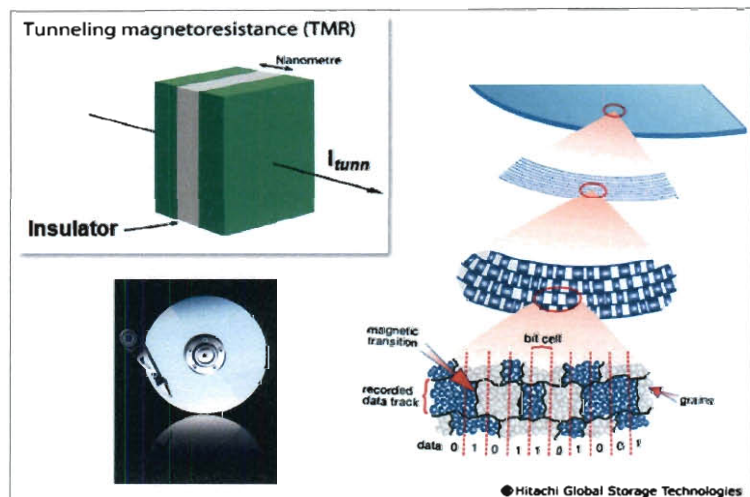


Figure 1.1. Images highlighting technological innovations of hard drives. Upper left: planar TMR junction used to retrieve magnetic information, magnetic layer (green) separated by insulator (white). Lower left: image of hard drive arm hanging over platter storing magnetic information. Right: data layout on platter. Image modified from [6,7].

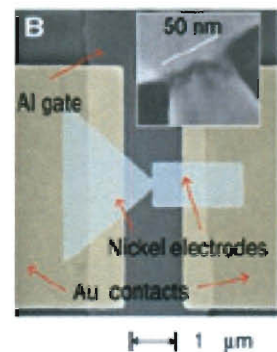
junction devices, two ferromagnetic thin film layers are separated by an insulating layer. A bias is placed across the three-layer junction, and when the magnetization (moment-alignment) in each ferromagnetic layer is aligned parallel, the current through the junction is high; when the magnetization (moment alignment) in each ferromagnetic layer is anti-parallel, current through the junction is low. The magnitude and sensitivity of this TMR effect, however, is critically dependent on the interface electronic density of states (DOS) at the ferromagnetic metal-insulator interface.[8,9,10,11,12] The density of electronic states (DOS) at the interface, and thus spin-polarized tunneling current, is significantly affected by the electronic/atomic structure and bonding at the interface.

The functionality of tunneling magnetoresistance junctions based on single molecules, like the Ni-C₆₀-Ni nanosystem (figure 1.2), is also subject to quantum mechanical effects at the interface. The Ni-C₆₀-Ni system (also known as a spin-polarized molecular electronic break junction) has demonstrated an enhanced TMR effect as high as 80% compared with Ni-Ni break junction devices, which report only a 19% TMR effect.[13]

As reported by Pasupathy and co-workers, the enhanced TMR

effect observed experimentally for Ni-C₆₀-Ni is directly attributable to bonding (coupling) at C₆₀-Ni interface. The coupling breaks the degeneracy of

Figure 1.2. SEM image of right/left Ni electrodes of molecular break junction (inset) where C₆₀ would be placed to produce TMR effect. Image was modified from [13].



electron spin and produces Kondo-type resonances near the Fermi surface. The resonances increase the tunneling conductance (TMR effect) for this system.

Hard drive technology also utilizes magnetic thin film media to record and store information. The most widely used thin film materials are four- and five-element CoCr-alloys. These alloys are used for their high magnetic coercivity, magnetic anisotropy and saturation magnetization.[14] The role of Cr in these alloys is to segregate itself from the polycrystalline grains and concentrate at the grain boundaries of the thin film.[15,16] The impurity segregation of Cr at the grain boundaries acts to decouple and reduce the quantum mechanical “exchange” interactions, h_e (h_e interactions work to align the magnetic moments of individual grains parallel to one another), between the grains to an optimal level. This exchange decoupling increases bit stability in the film and reduces signal noise in hard drives.[17,18,19]

Composite Co-C₆₀ and Fe-C₆₀ nanocrystalline thin film media have molecular impurities (C₆₀) instead of elemental impurities concentrated at the grain boundaries. These composite films have also been investigated for their potential use in magnetic media applications, due in-part to the C₆₀ molecule’s ability to stabilize nanosize grain formation within the film.[20] Recent experimental work by Zheng and co-workers has shown that the bulk magnetic properties (magnetic anisotropy, coercivity) of the composite films can be manipulated with C₆₀ concentration at the grain boundary; changes in bulk magnetic properties were attributed to the C₆₀ fullerene’s ability to influence film grain size and structure.[21,22] To-date, it remains unclear how the electronic interactions and atomic structure at C₆₀-grain boundary interface affect local

magnetic properties – as the interactions at the C₆₀-grain boundary interface may also influence the bulk magnetic properties of the film.

Photoemission studies of O-adsorption at the surface of Ni have also shown that the Ni surface magnetic moment is suppressed by the presence of oxygen. However, oxygen adsorption has no effect on the Co surface moment and tends to enhance the Fe surface moment.[23] Other studies utilizing x-ray magnetic circular dichroism (XMCD) have also been used to investigate the magnetic interactions of CO and NO at the surface of Co.[24] While the information gained from photoemission and XMCD analysis techniques cannot be understated, the magnetic properties obtained are “averaged” properties over large surface areas; few studies address the local effects of adsorbates at magnetic surfaces or at interfaces such as grain boundaries.[25] The subject matter of this dissertation is to determine how the electronic and atomic structure at the Ni(100) and Co(0001) film surfaces effect the bonding and local magnetic properties at the C₆₀-metal interface.

As the use of magnetic materials becomes more prevalent in nanoscale device applications, such as the C₆₀- based TMR junctions or Fe-based nanoparticulate clusters for targeted drug delivery (shown in figure 1.3), developing a solid understanding of how the molecular environment and interactions influence the magnetic properties at the surface becomes essential.[26] In chapter 2, a theoretical development of spin-averaged and spin-polarized scanning tunneling microscopy/spectroscopy analysis

techniques are presented along with a discussion of relevant C_{60} studies at the surface of metals and semiconductors.

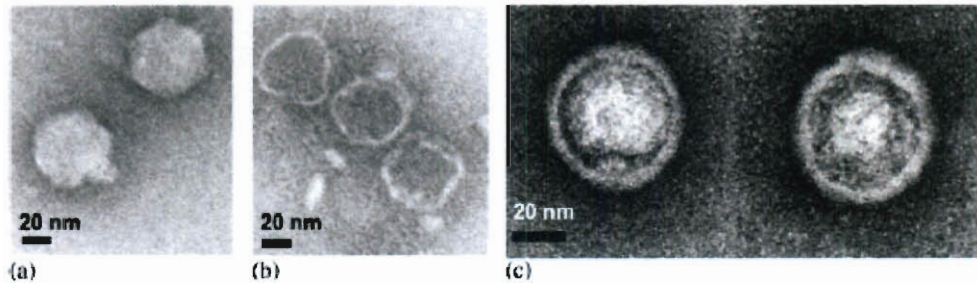


Figure 1.3. TEM of T7 bacteriophage (a) normal viruses, (b) ghost virus particles after osmotic shock, and (c) "magnetic viruses" with iron oxide nanoparticles at their center. Image modified from [26]

In chapter 3, in-situ scanning tunneling microscopy and spectroscopy (STM/STS) and Auger electron spectroscopy (AES) were used to determine the effect of C_{60} on film growth and morphology of Ni/Cu(100) and Co/Ru(0001) systems. In these studies, it was determined that despite the presence of C_{60} , C_{60} had no obvious effect on the crystalline (pseudomorphic) growth of Ni(100) films. During Ni film growth, the low mobility of C_{60} at the surface of Ni and relatively high Ni diffusion barrier limited the occurrence Ni- C_{60} collisions at the surface. AES results suggest the C_{60} molecules maintain their chemical integrity during Ni growth.

During Co film growth, Co islands only nucleated and grew from step edges or locally around C_{60} molecules. The strength of the Co- C_{60} bond interaction appeared stronger than the Co-Co bond on Co film terrace. The findings indicate that the nature of the C_{60} -metallic bond at the surface may influence film nucleation during film growth and the resultant film morphology.

In Chapter 4, spin-polarized scanning tunneling microscopy and spectroscopy (SP-STM/STS) studies were used to determine the local spin-polarized electronic structure of bare Co/Ru(0001) films and Co/Ru(0001) films with C_{60} adsorbed at the surface. SP-STS measurements found four distinct domains present at surface of Co: (i) fcc $\uparrow\uparrow$ and fcc $\uparrow\downarrow$ domains and (ii) hcp $\uparrow\uparrow$ and hcp $\uparrow\downarrow$ domains with a perpendicular magnetic spin-orientation at the surface. Magnetic domain walls at the surface also showed evidence of pinning at dislocation lines, indicating the spin-polarized electronic structure of Co(0001) is influenced by a number of factor: (i) sequential layer stacking (fcc/hcp), (ii) strain-induced reconstruction (moiré), (iii) Co(0001) atomic layer thickness, (iv) and surface defects.

For C_{60} adsorbed at the Co surface, a 3-fold (symmetry) molecular-orientation was observed. No local affect of C_{60} was detected on the surface magnetic properties of Co. However in the near-region of C_{60} clusters, the absence of surface state peaks was observed; these results suggest that C_{60} molecules induce local electronic perturbations on the Co(0001) film surface. In Chapter 5, the conclusions of this dissertation are presented along with suggestions for future work.

CHAPTER 2: EXPERIMENTAL BACKGROUND AND THEORY

2.1 STM

The scanning tunneling microscope (STM) is a surface probe technique which provides information about the surface (topography) and electronic structure of atomic and

molecular systems with

atomic resolution, via

detection of conduction

electrons. The STM (shown in figure 2.1[27]) operates based

on the principle of quantum

mechanical tunneling, in which

electrons from the sample (e^- source) have some probability of penetrating an

electronic barrier potential (vacuum) of finite height (V) and thickness into the tip (e^- detector).[28]

When the conducting tip (i.e., W or PtIr) is brought into close proximity with a sample surface, which is also conductive, and a bias is applied across the small vacuum gap,

electrons near the Fermi surface of the sample attain enough energy to overcome the potential barrier across the vacuum gap and tunnel into the tip. The electronic

tunneling is detected as current at the tip. As the tip is scanned across the surface, the electronic tunneling current is monitored and controlled by an external feedback loop

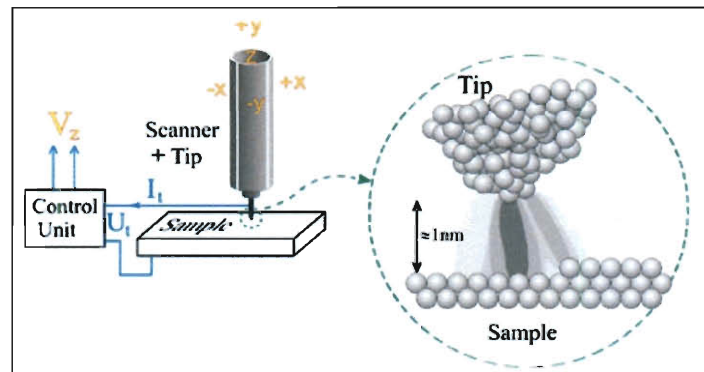


Figure 2.1. Scanning tunneling microscope (STM) device with corresponding control unit. (inset) Shows tip within tunneling range near sample surface. Image modified from [27]

(circuit). The external feedback loop seeks to maintain a constant tunneling current, using a piezo to adjust the tip-sample distance. In this regard, the real-space topography for an electronically homogeneous sample material is traced.

2.1.1 STM Theory: The theoretical approximation as reported by Tersoff and Hamann, treats the sample surface exactly and models the tip as a localized spherical potential well.[29,30] Here, the tunneling current is expressed using Bardeen's formalism:

$$I = \frac{2\pi e}{\hbar} \sum_{u,v} f(E_u) \cdot [1 - f(E_v + eV)] \cdot |M_{uv}|^2 \cdot \mathcal{D}(E_u - E_v), \quad (2.1)$$

$$M_{uv} = \frac{\hbar^2}{2m} \int d\vec{S} \cdot (\psi_u^* \vec{\nabla} \psi_v - \psi_v \vec{\nabla} \psi_u^*), \quad (2.2)$$

which describes the tunneling process as the probability of an electron tunneling through a barrier, giving equal consideration to both surface (localized) and bulk (de-localized) states.[31,32] In Bardeen's formalism, the assumption is that in order for surface state electrons to hop between leads (tip-sample), they must couple via extended states in both leads, via through inelastic tunneling processes (i.e., impurity-induced random potentials; electron-phonon coupling; electron-electron scattering). The inelastic tunneling phenomena are rate limiting in the surface state tunneling transport across the barrier. The $f(E)$ represents the Fermi function, M_{uv} is the tunneling matrix which contains all relevant information pertaining to the electron interactions and electronic states between that of the tip (ψ_u) and the sample surface (ψ_v) – the component of the equation (2.2) in the parenthesis is the current

operator, V is the applied voltage, and E_u is the energy of the tip state (ψ_u) in the absence of tunneling.

For simplicity Tersoff and Hamann make the assumption that the tip and sample are the same material. Approximating the tip wavefunction as a spherically symmetric s-wave and expanding equation (2.1) becomes:

$$I(\vec{r}_0, V) = 32\pi^3 \hbar^{-1} e^2 V \phi^2 D_t(E_F) R^2 \kappa^{-4} e^{2\kappa R} \times \sum_v |\psi_v(\vec{r}_0)|^2 \delta(E_v - E_F), \quad (2.3)$$

$$\rho(\vec{r}_0, E) \equiv \sum_v |\psi_v(\vec{r}_0)|^2 \delta(E_v - E), \quad (2.4)$$

where $\rho(\vec{r}_0, E)$ is the density of electronic states (DOS) at the surface, $D_t(E_F)$ is the electronic DOS of the tip at E_F , R is defined as the radius of curvature of the tip, and κ is the decay length of the wavefunction through the vacuum barrier.

Equation (2.3) shows that when a metallic STM tip is scanning across a surface, the tunneling current (constant current) is probing the contour of a constant electronic DOS at the surface. Given the fact that the amplitude of the wavefunction at the sample surface $|\psi_v(\vec{r}_0)|^2$ is proportional to $e^{-2\kappa(R+d)}$ at low bias, the tunneling current becomes a simple exponential function of tip-sample separation, $I = e^{-2\kappa d}$; here, the STM (tunnel current) is able to trace the real-space topography of atoms at the surface. Taking the derivative of the tunneling current with respect to the voltage yields a tunneling conductance in which directly proportional to the DOS of the surface material

$\sigma = dI/dV \propto \rho(\vec{r}_0, E)$ at a given energy, $\varepsilon_F + eV$, where V is the bias voltage. By adjusting the V (i.e., electron energy in the system with respect to ε_F), the STM is able to map the electronic structure of the material, known as scanning tunneling spectroscopy (STS). These surface probe techniques, STM and STS, have proven extremely useful in the thin film growth studies of various metallic and semiconductor systems; STS surface studies have also been used to demonstrate the presence of such surface phenomena as Friedel oscillations at surface of $\text{Be}(10\bar{1}\bar{0})$ and to observe changes induced in the electronic DOS of a substrate due to the presence of an adsorbate at the surface. [33,34,35,36]

2.1.2 Spin-Polarized STM Theory: In the model described below, Wortmann *et al.* develop a generalized formalization of the Tersoff-Hamann STM model to describe the presence of contrast in spin-polarized scanning tunneling microscopy experiments (SP-STM). For a more rigorous development of the model, please reference [37, 38, 39, 40, 41]. To apply the Bardeen formalism to the case of SP-STM, the tunneling matrix element, M_{uv} , must be written in a more generalized form to account for spin using a two-component spinor for the tip wavefunction:

$$\Psi_u^T = \begin{pmatrix} \psi_{u\uparrow}^T \\ 0 \end{pmatrix} \quad \text{or} \quad \Psi_u^T = \begin{pmatrix} 0 \\ \psi_{u\downarrow}^T \end{pmatrix}. \quad (2.5)$$

Assuming the sample surface has many different magnetic spin structures (spin-mixed) and defining the magnetic quantization axis (magnetic moment) for the system with respect to the STM probe tip, the sample surface wavefunction is defined as:

$$\Psi_v^S = \begin{pmatrix} \psi_{v\uparrow}^S \\ \psi_{v\downarrow}^S \end{pmatrix}. \quad (2.6)$$

To determine the appropriate normalization for the sample surface wavefunction, Ψ_v^S , the tip wavefunction is modeled as a single atom contained at the tip apex. Similar to the T-H model assuming the spin-up, $n_T^\uparrow(\varepsilon)$, and spin-down, $n_T^\downarrow(\varepsilon)$, tip DOS is constant with respect to energy near E_F but possess a different magnitude to account for magnetization within the tip, $\vec{m}_T = (n_T^\uparrow(\varepsilon) - n_T^\downarrow(\varepsilon))\vec{e}_M^T$, where \vec{e}_M^T is the magnetization (quantization) axis of the tip. Based on the assumptions stated above, the spin-polarized tunneling current becomes:

$$I(\vec{r}_0, V, \theta) = \frac{8\pi^3 C^2 \hbar^3 e}{\kappa^2 m^2} \int d\varepsilon \cdot g_V(\varepsilon) \sum_v \delta(\varepsilon_v - \varepsilon) \times \left(n_T^\uparrow |\psi_{v\uparrow}^S(\vec{r}_0)|^2 + n_T^\downarrow |\psi_{v\downarrow}^S(\vec{r}_0)|^2 \right) \quad (2.7)$$

Where $g_V(\varepsilon) = f_u(\varepsilon - \varepsilon_F) - f_v(\varepsilon + eV - \varepsilon_F)$ and $\theta(r_0, V)$ represents the angle magnetic moment of the tip and the sample surface. For the general case of a surface with multiple different magnetic spin structures (spin-mixed), the tunneling current, $I(\vec{r}_0, V, \theta)$, can be divided into an unpolarized (I_0) contribution and a spin-polarized tunneling contribution (I_p), which is typically very small) such that:

$$I(\vec{r}_0, V, \theta) = I_0(\vec{r}_0, V) + I_p(\vec{r}_0, V, \theta) \quad (2.8)$$

$$= \frac{8\pi^3 C^2 \hbar^3 e}{\kappa^2 m^2} [n_T \tilde{n}_S(\vec{r}_0, V) + \mathbf{m}_T \tilde{\mathbf{m}}_S(\vec{r}_0, V)]$$

where the C is a normalization constant typically close to unity, κ is the decay length of the wavefunction through the potential barrier (vacuum), and where $\tilde{n}_S(\vec{r}_0, V)$ is the integrated local DOS (ILDOS), and $\tilde{\mathbf{m}}_S(\vec{r}_0, V)$ is the integrated local magnetic DOS vector for the sample surface. As can be seen from equation (2.8), the spin-polarized portion of the tunneling contribution, $I_p(\vec{r}_0, V, \theta) \propto \mathbf{m}_T \tilde{\mathbf{m}}_S(\vec{r}_0, V)$, is essentially a projection of the sample magnetization in the vicinity of the tip onto the tip's magnetic moment. So similar to tunneling magnetoresistance devices (used in computer hard drives), the spin-polarized tunneling between the tip and sample displays a magnetoresistive effect. When the tip-sample magnetic moments are aligned parallel ($\uparrow\uparrow$) to one another, the tunneling current increases; when the moments are anti-parallel ($\uparrow\downarrow$), the tunneling current decreases. The SP-STM technique is sensitive to sample spin-polarization polarization at the surface.

In a similar manner, taking the derivative of the tunneling current with respect to voltage bias, V , the differential conductance at small biases becomes:

$$\frac{dI}{dV}(\vec{r}_0, V, \theta) \propto [n_T n_S(\vec{r}_0, \varepsilon_F + eV) + \mathbf{m}_T \mathbf{m}_S(\vec{r}_0, \varepsilon_F + eV)] \quad (2.9)$$

where the dI/dV is directly proportional to the n_S and \mathbf{m}_S at a given energy, $\varepsilon_F + eV$, and V is chosen to maximize the magnetic contrast of the system. In the remainder of

this study all magnetic contrast imaging is obtained using spatially-resolved dl/dV -maps, as these provide the best conditions for identification of magnetic contrast in the Co/Ru(0001) system.

SP-STM has proven to be an extremely useful technique for resolving the magnetic structure and properties of various magnetic thin film and nano-particulate systems down to the atomic scale.[42] Electrochemically-etched W-tips coated with thin films of ferromagnetic (Fe, Gd) or antiferromagnetic (Cr, Mn-alloy) materials are most often fabricated in-situ for use in SP-STM experiments. These magnetically-coated tips reduce stray H-field emission and reduce tip-sample magnetic dipole interactions during measurement, and the tips can be fabricated to be sensitive to in-plane or either perpendicular magnetic orientations at the film surface.[43] Fe-coated W-tips sensitive to in-plane sample magnetization were used in this study to collect spin-polarized conductance measurements discussed in Chapter 4. As will be shown, these measurements were used to determine the magnetic domain structure of 1.84 ML post-annealed Co films grown on a Ru(0001) substrate, and observe the impact of a large molecular adsorbate, C_{60} , on the local electronic structure of Co at the surface.

2.2 Co(0001) Electronic Structure

2.2.1 Magnetic Moment of Co: The hexagonal close-packed crystalline form of Co has been reported to have a bulk magnetic moment (\mathbf{M}) of $1.708 \mu_B$. [44]; in other systems, such as fcc Co/Cu(001), the Co was measured to be $1.68 \mu_B$. [45] The existence of

ferromagnetism (a many-body effect) in metallic elemental materials such as Co (also Fe, Ni, Gd) is linked to the Coulombic interaction that exist between neighboring atoms within the crystal and the Pauli exclusion principle, resulting in quantum mechanical exchange interactions between electrons. Given the sensitivity of ferromagnetism to changes in the electronic wavefunction overlap of nearest-neighbor atoms, local changes in the atomic lattice spacing, structure, and symmetry and the chemical environment can have a dramatic effect on the magnetic properties.[46]

Due to a reduced symmetry at the surface of ultra-thin magnetic films, enhanced magnetic moments have been observed in various films. For fcc Co films grown on Cu(100), a 5-6% enhanced surface orbital- $\mathbf{M} \langle L \rangle$ ($0.26 \mu_B$) and spin- $\mathbf{M} \langle S \rangle$ ($1.82 \mu_B$) have been experimentally measured and predicted.[47,48,49] Enhancements in the surface- \mathbf{M} have also been reported in other systems, i.e. Cr(001)& Ni(111) surface]. [50,51]

2.2.2 Magnetic Orientation of Co Films: The reduced dimensions of magnetic ultra-thin films can also lead to changes in the magnetocrystalline anisotropy energy (MAE) of the film. For bulk hcp-Co, the easy axis of magnetization is the $[000]$ -direction.[52]

However, atomic structure, strain and interface and surface effects often lead to an MAE in thin films away from what is observed in bulk materials. The fcc structure of Co is stable only above 700°C in bulk. However, it is well-known that a stable fcc-phase of Co grows pseudomorphically on the Cu(001) substrate surface at room temperature.[53,54] In these Co films, Weber *et al.* and others show that the magnetic

orientation (MAE) of the 12 ML Co films are in-plane with the easy-axis of the film directed along the $[1\bar{1}0]$ -direction and the $[1\bar{1}0]$ -direction. [55,56,57] At larger film thickness, the Co film undergoes a spin reorientation transition (SRT) and magnetic orientation (easy-axis) switches to perpendicular-orientation with respect to the surface. These spin reorientation have also been observed in other systems as well. In a similar Ni/Cu(100) system, pseudomorphic Ni is observed to have an in-plane spin orientation for film thicknesses < 7 ML; for thicker films, the easy-axis of magnetization switches to a perpendicular direction; at 75 ML the magnetization switches again back to an in-plane orientation [58,59,60]

A similar double SRT is observed in ultra-thin Co films grown on a Ru(0001) substrate surface. In a recent in-situ spin-polarized low-energy electron microscopy study, Gabaly *et al.* demonstrate that 1.5 ML Co films grown at 460 K show an in-plane orientation in the 1 ML regions of the Co surface and an out-of-plane orientation in the 2 ML regions of the Co surface.[61] For thicker Co films, the 3 ML islands and greater show an in-plane magnetic orientation. These observations have been attributed to competing surface (shape anisotropy) and interface effects (strain, substrate hybridization).[62,63] However, film growth and annealing conditions may also influence the resultant magnetic properties of the Co film.[64] In Chapter 4, results from the SP-STM analysis show that post-annealed Co films grown at 77 K have a slightly different magnetic structure, which can be directly attributed to the film stacking and strain relaxation.

2.2.3 Surface State Electronic Structure of Co Films: The physical properties (electrical, thermal, magnetic, atomic structure) and chemical (bonding, reactivity) properties of bulk 3-dimensional solids are governed by the electronic band structure of the material. However due to the reduced symmetry at the surface of solid state materials, the 3-dimensional Bloch waves (bulk states) of bulk the periodic solids become a 2-dimensional Bloch wave (surface states) at the surface with an imaginary component. The changes observed in the electronic structure at the surface also alter physical properties, such as magnetism and chemical reactivity at the surface.[65]

The presence of surface states in the electronic structure of solids has been a well-known physical phenomena since their discovery by Russian physicist Igor Tamm in 1932. Surface states exist because the infinite periodicity of a solids material is interrupted by a surface where the 3-dimensional (bulk) Bloch waves are now scattered forming standing waves within the crystal.[66] As a result 2-dimensional Bloch waves (electronic surface states) are created whose wavefunction amplitude is physically bound at the surface. [67,68,69] These states primarily reside in the band gap regions of the solid and a have k_{\parallel} – dispersion to the surface.

Primarily two types of surface states exist: (i) image potential surface states and (ii) crystal-induced surface, also known as Shockley surface states. Image potential states derive from a long range Coulomb-like tail behavior of the surface potential toward the vacuum potential. These states have energies that sit close to vacuum, typically high

above E_F . On the other hand, crystal-induced surface states derive from the bulk bands of the crystal and have a tendency to take on the characteristics of the bulk band states that they sit close to within the band gap. Crystal-induced states sit closer to E_F . For a more comprehensive discussion and theoretical development of surface state electronics, please reference Norbert Memmel's Surface Science Reports.[70]

In the bulk electronic structure of ferromagnetic materials, the bulk d -bands are

exchange split. These exchange split bulk band states are the result of a solids material meeting the condition known as the "Stoner criterion," $N \cdot I > 1$, where N is the DOS of the material at the Fermi level,

E_F , I is the Stoner molecular-field constant (material-dependant) and contains some

form of the exchange-correlation integral.[71] When $N \cdot I > 1$, ferromagnetic ordering (magnetization) is stable within the system and derives from the spin-imbalance (difference in the number of e^- in d -bands with spin-up versus spin-down) that exists between the exchange-split states from bulk d -bands (spin-up/down).

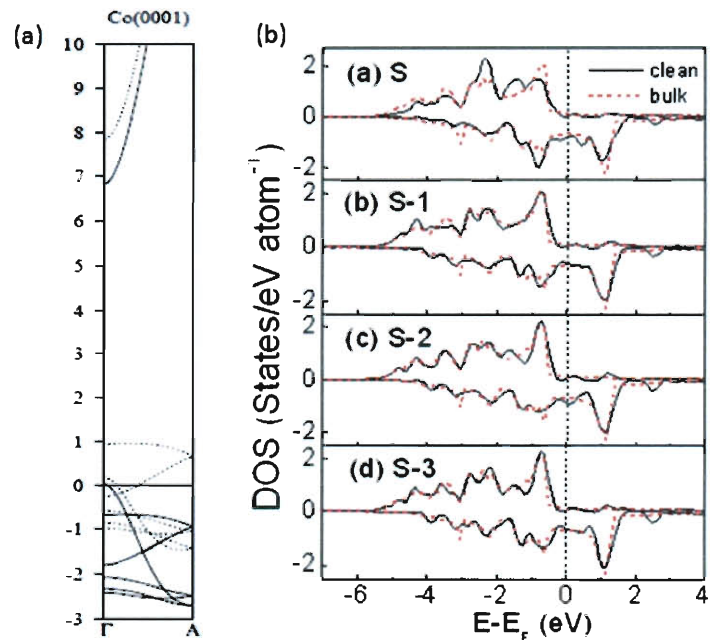


Figure 2.2. (a) Bulk electronic structure of Co(0001) along symmetry points Γ -A {reference Appendix [A]}. Solid lines represent majority bands and dotted lines represent the minority bands. (b) Density of states for clean Co surface (S is surface atomic layer of Co; S - i represents lower atomic layer). Images modified from [72, 73].

The result is a solid material with a spin polarization in the bulk and at the surface, where spin polarization is defined as $P = (n_{\uparrow} - n_{\downarrow}) / (n_{\uparrow} + n_{\downarrow})$. Cobalt has a negative spin-polarization, as the number of electrons with spin-down near the Fermi surface outweighs the spin-up electrons. A model of the Co(0001) electronic band structure is shown in figure 2.2(a), along with a calculation of the DOS for a clean Co surface, figure 2.2(b).[72,73]

It is well-known that the surface states of ferromagnetic materials are also exchange split (spin-polarized). In the remainder of this discussion, only crystal-induced surface states will be discussed as surface states derived from the image potential do not influence the magnetic properties of solids at the surface.[74] For the Co(0001) surface, Himpsel and Eastman in angle-resolved photoemission studies were able to confirm the existence of an intrinsic surface state 0.3 eV below Fermi with Λ_1 -symmetry near the Γ -point {where Γ is the center of the hcp Brillouin zone in reciprocal space as defined in Appendix [A]}.[75] Spin-polarized STM measurements of Co films on Cu(100) and Cu(111) substrates have also experimentally confirmed the existence of these surface states with minority (spin-down) spin character, along with the existence of another unoccupied state with majority character at 0.1 eV above Fermi.[76,77,78,79]

However, discrepancies exist in the literature regarding the exact origins of the spin-polarized surface state peak observed from spin-averaged and SP-STM of Co/Cu(100)

and Co/Cu(111) systems. Some of these experimental discrepancies have been attributed to interface mixing and strain. In chapter 4 of this dissertation, results from the SP-STM measurements of the Co/Ru(0001) system will be discussed. To-date little spin-polarized tunneling measurements have been collected for this system. In this dissertation, it will be shown how magnetization at the Co(0001) surface responds to local changes in atomic structure and substrate interface effect.

2.3 The C₆₀ Fullerene's Physical & Electronic Properties and Interactions with Metallic Surfaces

As discussed in Chapter 1, the C₆₀ fullerene has recently received much attention because of its potential for use in magnetic data storage and transistor device applications.[80] These applications include C₆₀-based molecular transistor junctions (MTJ), and tunneling magnetoresistance (TMR) devices, and molecular-based voltage oscillators. Recent studies by Zheng *et al.* investigated the applicability of C₆₀-based fullerene composite thin films (Fe-C₆₀, Co C₆₀) for application in magnetic data storage.[81] In these composite films, it was observed that (i) C₆₀ molecules tended to aggregate at the grain boundaries within the composite film and (ii) the bulk magnetic properties of the film could be altered by the concentration of C₆₀ within the film. In each device, the characteristics of the molecular-interface with a metallic or semiconducting surface are crucial in the device's operation.

In the remainder of this chapter, the nature of the electronic interactions and structural properties of C_{60} at the surface of metals will be discussed. In section 2.3.1, the nature of the chemical interaction of C_{60} at the surface will be discussed. Section 2.3.2 C_{60} ordering at the surface of metals and its influence on surface reconstruction will be discussed; and in section 2.3.3, the resonant tunneling mechanism observed during STM measurement in the near-region of adsorbates at the surface will be discussed.

2.3.1 Chemical Interactions of C_{60} at Metal Surfaces: The C_{60} molecule has the shape of a truncated-icosahedron (nearly-spherical). C_{60} in its single crystalline form has an fcc crystalline phase ($Fm\bar{3}m$) at room temperature.[82,83] In this phase, the molecules have nearly free rotation (ratchet) about their positions within the fcc lattice, due to weak van der Waal interactions between the individual molecules in the crystal lattice.[84] Upon cooling the molecular crystal below 261 K, the lattice undergoes a first-order phase transformation from fcc ($Fm\bar{3}m$) to a simple cubic ($Pa\bar{3}$) structure.[85] Below this temperature the rotations (ratcheting) of the C_{60} molecules are slowed in the $Pa\bar{3}$ lattice and limited to one of the four symmetry $\langle 111 \rangle$ -symmetry axes in the simple crystal. At even lower temperatures (< 90 K), only two orientations of C_{60} exist within the crystal lattice (P -, H -configuration), in which a molecular pentagon or hexagonal of one molecule faces a double bond of a nearest-neighbor molecule, respectively [86]. At the surface of metals, these intermolecular rotational (librational) modes of C_{60} are greatly impeded or ceased, depending on the strength of the C_{60} -metal bond at the surface.

When C_{60} is adsorbed onto the surface of a metal, charge is donated from the metal surface to the C_{60} molecule. In a study by Hunt and co-workers, high-resolution electron energy loss spectra (HREELS) measurements are used to correlate downshifts in the C_{60} molecule's vibrational modes to the amount of electron charge transfer from the metallic surfaces of Au, Ag, and Ni.[87] The amount charge transferred to molecule from the surface does not correlate with metal workfunction(ϕ); a correlation between the amount of charge transferred with metal workfunction would indicate that an initial imbalance in chemical potential (misaligned E_f) drives charge transfer between the metal surface and C_{60} . For Au ($\phi = 5.37$ eV), Ag ($\phi = 4.60$ eV), Pt ($\phi = 6.12$ eV) and Ni ($\phi = 5.04$ eV), the calculated charge transferred to C_{60} is 0.4, 0.9, 0.8 and 2.3 e^- /molecule, respectively. Since e^- charge transfer is not mediated by alignment of E_f – levels at the C_{60} -metal interface, this indicates a chemisorptive bond is formed, in which the chemical identity (charge state) of both molecule and substrate change locally.[88]

When adsorbates (i.e., H_2 , O_2 , N_2 , CO , C_{60}) approach the surface of a metal, there is an interaction between the molecular orbitals of the molecule and the orbitals (bands) of the metal surface. The interaction between molecule and substrate can proceed through physisorptive or chemisorptive processes. If the adsorbate physisorbs at the surface, the adsorbate-substrate interaction is governed by dipole-dipole (i.e., fluctuating molecular dipoles and image dipoles at the solid surface) interactions at the surface. [89] If the adsorbate is chemisorbed at the surface as is the case C_{60} on the

surface of transition metals, the interaction is governed by the band-orbital alignment between the two respective species – the transition metal and adsorbate.

As mentioned above, chemisorptive bonds change the identity of the adsorbate and metal species involved; they weaken the bonds within the adsorbate and locally weaken the bonds at the transition metal surface.[90] In the C₆₀ molecules adsorbed at the surface of transition metals result in shortening of the longer 1.433 Å bond and slight lengthening of the shorter 1.378 Å bond. [91,92] The adsorbate-metal bond at the surface tends to be a compromise between the bond formed between the two species and the weakened bonds of the molecule and substrate.

For molecules like C₆₀, the frontier orbitals (highest-occupied-molecular-orbital, HOMO; lowest-unoccupied molecular orbital, LUMO) are most important in determining the chemical reactivity and behavior of a molecule at the surface. For transition metals, the d-bands near the Fermi surface play the most important role in adsorbate-substrate interactions. When an adsorbate approaches a metallic surface, two factors determine the strength of the adsorbate interaction: (i) the filling of anti-bonding states in the molecule and (ii) the degree of orbital overlap. The strength of the bond formed and the amount of charge donated can be correlated to the net energy gained, as estimated by the one electron energy term, E_{el} , from 2nd-order perturbation theory:

$$E_{el} = -2f_d \frac{|V_{ad}|^2}{\epsilon_d - \epsilon_a} + \alpha \cdot V_{ad}, \quad (2.10)$$

where f_d is the degree or partial filling of d-bands in the metal, V_{ad} is the coupling matrix element, ε_d is the position of the d-band center with respect to E_f , and ε_a is the energy the level of the molecular orbital.[93] The first term in equation (2.10) accounts for adsorbate-substrate attraction due to hybridization; the second term is a Pauli repulsion term, induced by the orthogonalization of overlapping molecular-orbital and d-band wavefunctions. Since, alpha in the second term is relatively small, the second term can be generally be neglected.

The relatively high binding energy of C_{60} at the Ni surface compared with other transition and noble metal surfaces has been directly attributed to C_{60} -Ni hybridization at the surface.[94] As shown in figure 2.3, the d-band states of Ni sit very close to Fermi

and fairly close to the LUMO orbitals of C_{60} . [95] As a result a relatively strong binding energy (chemisorptive bond) formed at the Ni surface as compared with Cu whose d-band states sit much

lower. As we will see in Chapter 3, the higher binding energies of C_{60} and Ni result in a lower mobility of C_{60} at the Ni(100) surface. Nickel's

electronic interactions with C_{60} are also stronger than Pd (which like Ni is a group VIII d-

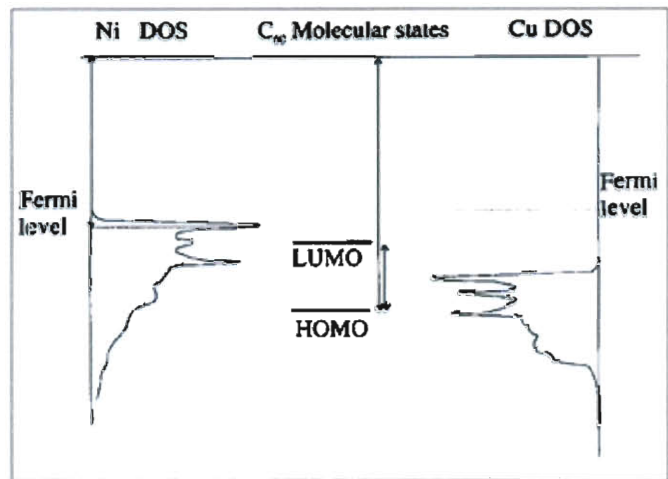


Figure 2.3. Diagram comparing the electronic DOS of Ni(110), left, and Cu(110), right, to the molecular-orbital levels of C_{60} . The close proximity of the Ni d-band and LUMO states of C_{60} leads to a stronger Ni- C_{60} hybridization and bonding interaction compared with the Cu surface. Image modified from [95].

band metal and has a very similar electronic structure) – a direct consequence of palladium's d-band center sitting further below the Fermi surface like Cu.

Comparing the d-band centers of Ni and Co, as calculated by Ruban *et al.*, the bulk values for Ni and Co are -1.29 eV and -1.17 eV below Fermi, respectively.[96] Going a step further, Ruban *et al.* also calculated d-band center of unrelaxed metal overlayers (monolayer films) on close-packed surfaces. As expected, the d-band center of both metal overlayers Ni/Cu(111) and Co/Ru(0001) shifted closer to the Fermi level: Ni/Cu(111) +0.12 eV above Fermi, Co/Ru(0001) -0.70 eV below Fermi (substrate hybridization effects not included). These values indicate that ultrathin films of Co, compared with Ni, have a weaker interaction with C₆₀ at the surface. As mentioned above the effects of (i) film strain relaxation and (ii) substrate hybridization with the overlayer were not included in the calculation. Each of these factors impact the band structure of film overlayer and shift the d-band center with respect to the Fermi level.

In Chapter 3 of this dissertation, a discussion of results from STM analysis are used to determine how binding energy impacts C₆₀ adsorption on the Ni(100) and Co(0001) film surfaces. For Ni, it is observed that the C₆₀ is fairly immobile and uniformly distributed across the Ni film surface. For Co, it will be shown that strain relaxation, film stacking and defects at the surface (i.e., dislocations) greatly affect the C₆₀-Co bond at the surface, resulting in a very non-uniform coverage of C₆₀ across the Co film surface.

Growth studies of Ni(100) and Co(0001) films pre-adsorbed with C_{60} are also highlight the effect of the C_{60} -metal interaction on film growth.

Section 2.3.2 The Ordering of C_{60} at the Surface of Metals: As discussed in section

2.3.1, the adsorbate bond strength at a metal surface plays a pivotal role in determining how a molecule like C_{60} may behave at the surface. However, other factors may also

influence C_{60} adlayer (adsorbate layer) behavior at the surface. Some of the other influences on the C_{60} adlayer are (i) the orientation of C_{60} at the substrate surface, (ii) the inter-molecular nearest-neighbor interactions of C_{60} at the surface, (iii) and

the physical and electronic properties of the substrate, such as the atomic structure, step density & direction, and surface

reconstruction / dislocations. In the remainder of this section, the effect of each of these factors on the C_{60} adlayer will be discussed from experiments reported in

literature. Hunt *et al.* conclude from LEED studies that sub-monolayer growth of C_{60} onto the Ni(110) surface is disordered below 540 K. However at substrate growth

temperatures above 600K, the three ordered quasi-hexagonal phases of C_{60} appear on the Ni(110) fcc surface, each phase either fully or partially commensurate with the

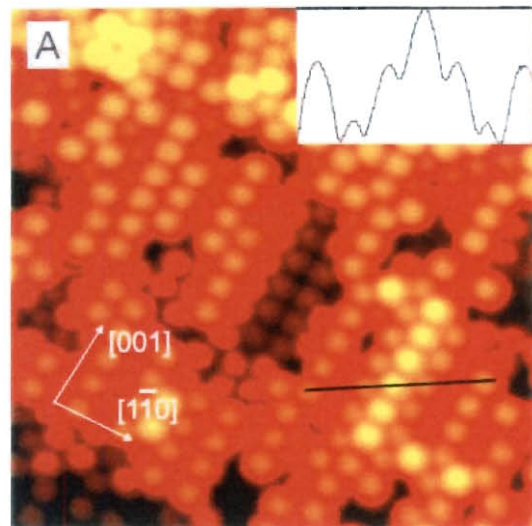


Figure 2.4. A $183\text{\AA} \times 196\text{\AA}$ STM topograph of C_{60} -induced reconstruction on the Ni(110) surface. The inset is a line section taken from the topograph, location indicated by black line. Image modified from [98].

substrate lattice.[97] A 'QH1'-phase is identified in the temperature range between 630 K and 660 K in which C₆₀ molecules show preferential diffusion along the $[1\bar{1}0]$ troughs in the $[100]$ -direction. This preferential diffusion is attributed to the limited mobility of C₆₀ on the Ni surface and increased diffusion barrier along the $[1\bar{1}0]$ -direction on the Ni(110) surface.

In a STM study by Murray *et al.*, C₆₀ was observed to order commensurately with the Ni(110) substrate surface along the $[100]$ -direction only at elevated temperatures, as well.[98] However in addition to this ordering, the C₆₀ was observed to induce reconstruction on the Ni(110) surface, forming microfacets along the $[100]$ -direction (C₆₀-induced reconstructions were also observed on Pd).[99] Figure 2.4 shows an STM image of C₆₀-induced reconstructions at Ni(110). The observed variations in C₆₀ height (1.3 Å) across the surface correspond to the monolayer step height of fcc Ni. Effective-medium theory (EMT) calculations show that the Ni surface reconstructions lower the overall energy of the system by increasing coordination between the C₆₀ and Ni; the energy gained from increased C₆₀-Ni binding outweighing the cost of breaking metal bonds.

For C₆₀ deposited on the Pd(110) surface, C₆₀ is observed to show anisotropic diffusion across the Pd surface with the C₆₀ diffusion barrier lower in the $[1\bar{1}0]$ -direction compared with the $[100]$ -direction.[100] Weckesser *et al.* rationalize a modified diffusion mechanism in which the C₆₀ rolls across the Pd surface changing its molecular

orientation as it diffuses – as opposed to a hopping diffusion mechanism, where the orientation of the molecule is maintained. The suggested diffusion mechanism is attributed to the near-spherical geometry of the C₆₀ molecule and the readily available lateral- π bonds formed as C₆₀ moves across the Pd surface.[101,102] At elevated temperatures, locally-induced C₆₀ reconstructions are observed on the Pd surface. The reconstructions form microscopic pits in the Pd(110) surface where C₆₀-Pd coordination is increased resulting in increased bonding. The reconstructions lead to different C₆₀ heights observed on the Pd(110) surface.

In a theoretical study of C₆₀ at the Al(111) surface, Stengel *et al.* show that the strong covalent bond formed at the surface between C₆₀ and Al induces reconstruction on the Aluminum surface, via an adatom-vacancy mechanism, in which the C₆₀ creates a vacancy on the substrate surface near the C₆₀ adsorption site.[103] The adatom-vacancy mechanism has been observed on other metal surfaces as well, Pt(111) and Ag(100).[104,105] From the STM results presented in Chapter 3, it is clear the C₆₀-Ni bond is equally strong on the Ni(100) surface. However, no induced surface reconstructions are observed on Ni surface. Short-range C₆₀ ordering is observed at room temperature.

The C₆₀ fullerene interaction on noble metal surfaces, Au(111) and Ag(111), was studied by Altman and co-workers. The Au(111) surface, which naturally reconstructs forming a herringbone-type $23 \times \sqrt{3}$ lattice, has a marked influence on the nucleation and growth

of C_{60} at the surface. On the reconstructed Au(111) surface, dislocation ridges separate fcc- and hcp-terminated regions; the fcc sites on the Au surface are observed act as nucleation sites for C_{60} . [106] Two phases of C_{60} were observed on the Au surface: an in-phase close-packed 38×38 lattice and a $2\sqrt{3} \times 2\sqrt{3} R30^\circ$ phase. C_{60} is also observed to disrupt reconstruction on the Au(111) surface. The disruptions observed in the Au surface wishbone reconstruction pattern indicate the strength of C_{60} -Au interaction at the surface. [107,108]

Although the Ag(111) surface is similar to the Au(111) surface in many ways (i.e., lattice constant, electronic structure), it does not reconstruct. On the Ag(111) surface, C_{60} molecules are observed nucleating first at the steps of narrow terraces and at step intersections. [109] On Ag, only the $2\sqrt{3} \times 2\sqrt{3} R30^\circ$ phase is found. On both the Au and Ag surfaces, C_{60} molecules show a high degree of mobility across terraces and along step edges.

In a similar STM study of C_{60} on the Au(111) surface, Guo *et al.* observe an hexagonally-close packed arrangement of C_{60} , similar to Altman as discussed above. [110] However, they also show evidence that C_{60} cluster (2-5 molecules) diffusion is the dominant means by which C_{60} diffuses across the Au(111) surface. In this study, C_{60} was deposited / applied onto the surface in a dilute solution of dichloromethane or benzene. This particular application method may have led to some level of contamination in the study and C_{60} - C_{60} intermolecular interactions and diffusion at the surface. Guo *et al.* also

determine that C_{60} - C_{60} intermolecular interactions are also anisotropic, which can destabilize or stabilize molecules at the edge of C_{60} clusters. The C_{60} - C_{60} interaction energy differences while small depends on the relative orientation of the interacting molecules.[111,112]

Dislocation ridges on the Au(111) surface were also found to impede C_{60} mobility.[113] Surface inhomogeneities, defects and other disruptions on the substrate surface (i.e., steps and step bunching), often alter the normal diffusion behavior of adsorbates at the

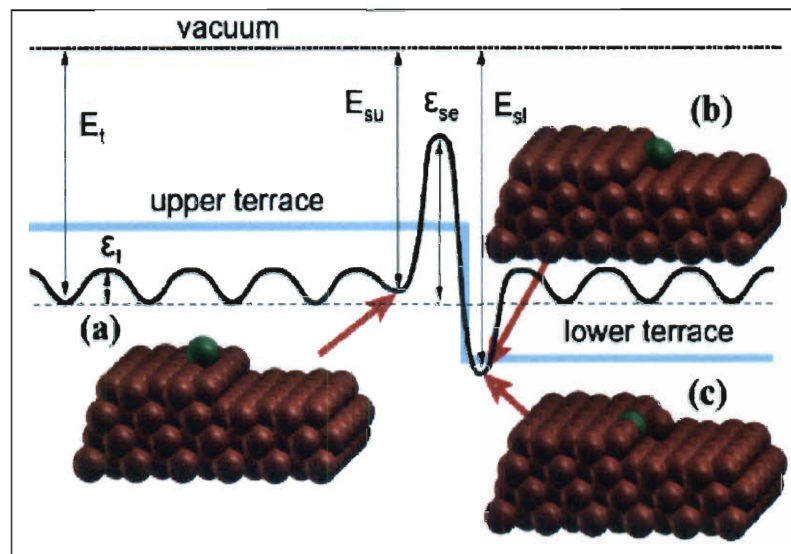


Figure 2.5. Energy diagram and atomic structures showing the motion of an adsorbate (green sphere) diffusing across a step. (a) illustrates the initial adsorbate configuration on the upper terrace step; (b) and (c) show the final configuration after adsorbate descent across the step, via hopping or exchange, respectively. Relevant binding energies, as defined by Mo et al. defined in text. Image modified from [116].

surface. In a study of W-adatom diffusion near a screw dislocation, Antczak *et al.* show that due to strain fields in the near region of the dislocation anisotropic, the W-adatom diffuses anisotropically in the [111]-direction near the screw dislocation.[114] Using a

field ion microscope (FIM), they are also able to calculate large differences in diffusivity in different regions near the screw dislocation. Adsorbates approaching the top terrace of a step edge encounter an energy barrier to further diffusion (descent) across the step – the Ehrlich-Schwoebel (ES) barrier. [115,116,117] If the adsorbate is able to overcome the barrier, it will descend across the step to the lower terrace, via a hopping mechanism or exchange, as shown in figure 2.5.[118] E_t , E_{su} , and E_{sl} are the binding energies on the terrace, upper step, and lower step, respectively. The ϵ_t and ϵ_{se} are the barriers to adsorbate diffusion across the terrace and step edge, respectively. On the lower-side of the step, a potential well exists and can be attributed to the higher substrate-adsorbate coordination at the terrace of the step. This potential well at the lower-side of a step is what leads to the preferential C_{60} adsorption at the step edges. A narrow succession of terraces (step bunches) can deepen the potential well on individual terraces and lock adsorbates at the step as discussed above for C_{60} at the surface of Ag. The impact of these surface inhomogeneities on C_{60} nucleation, ordering and growth will be addressed in Chapter 3.

2.3.3 Resonant Tunneling Mechanism for Molecular Adsorbates: In another study of C_{60} -monolayers deposited on the noble metal surfaces, Au(111) and Ag(111), Altman and coworker observed bright and dim contrasts in the C_{60} molecules deposited at the Au and Ag surfaces.[119] Unique internal (intra-molecular) structures were observed for many of the molecules adsorbed on the surface and the internal structures were bias-dependant. They attributed these experimental observations to (i) electronic

differences in the DOS above the molecule, (ii) differences in the molecular orientation of the molecule at the surface; and (iii) differences in adsorption-site symmetry were

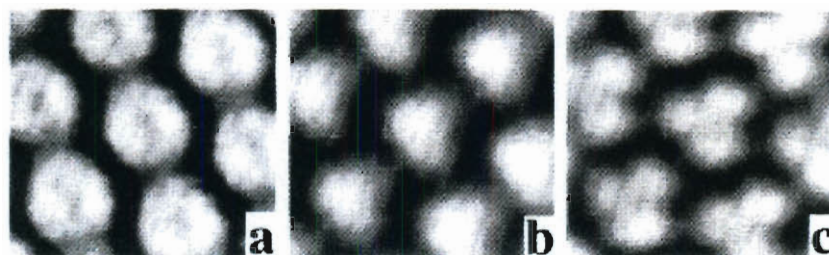


Figure 2.6. STM image of C_{60} molecules at the surface of Cu(111). V_b in (a) -2.0 V, (b) -0.1 V, and (c) 2.0 V. Image modified from [122].

also considered. Similar observations of the C_{60} intramolecular structure have been made on other transition and noble metal surface and on semiconductor surfaces (Cu, Si), as well.[120,121]

The internal structure of C_{60} is also observed for monolayer films adsorbed on the Cu(111) surface.[122] In this STM study, Hashizume *et al.* show that the observed intramolecular structure of C_{60} has a bias (V_b) dependence (shown in figure 2.6). In figure 2.6, the same region on the Cu(111) surface is imaged at different bias voltages. At $V_b = -2$ V, the internal structure of C_{60} looks like a doughnut with a hole in the center of the molecule. At $V_b = -0.1$ V, the hole disappears. When the $V_b = 2$ V, a 3-fold symmetry is observed in the C_{60} molecules internal structure, which they attribute to the symmetry of C_{60} molecule's internal structure at the surface. Theoretical calculations showed that the bias-dependence of the molecular contrast originated from electron tunneling from the HOMO-/LUMO-derived states of C_{60} .

Away from the adsorbate, tunneling is mediated via direct interactions between the substrate and the STM tip. However when the tip approaches an adsorbate chemisorbed onto a surface, the surface energy-levels are shifted (perturbed) by the presence of the adsorbate and simultaneously an additional tip-adsorbate interaction occurs. The result is a constructive/destructive interference effect of the thru adsorbate / surface tunneling current amplitude. So, electron transport in the near-region of the adsorbate (C_{60} -molecule) now proceeds via a “resonant tunneling” mechanism.

Resonance tunneling is an inelastic electron tunneling process in which the electron energy is converted into vibrational motion within the molecule. This tunneling mode is

mediated directly through molecular orbital (MO) interactions with the substrate and tip. Two major factors

determine which MO's contribute to the resonant tunneling current: (i) the energy

difference between the MO and the E_f of the metallic surface, and (ii) the adsorbate – tip / substrate coupling strength.[123,124,125,126,127,128,129] Qualitatively, the relative MO contributions to tunnel current can be represented by the simple equation:

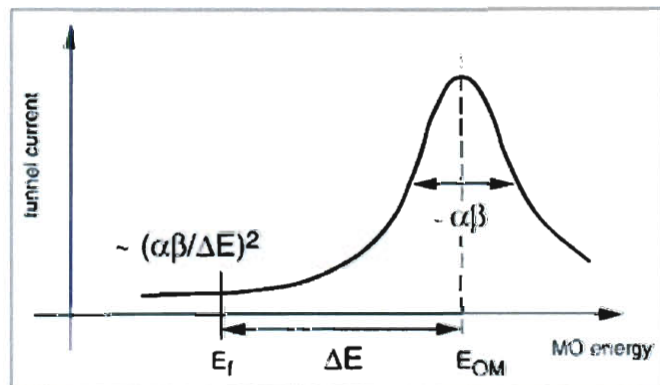


Figure 2.7. Diagram showing MO contribution to tunneling current (curve has Lorentzian line shape distribution). $\alpha\beta$ determines width of resonance. Image modified from [123].

$$I_t \propto (\alpha\beta/\Delta E)^2, \quad (2.11)$$

where α and β represent the adsorbate-tip and adsorbate-surface coupling, respectively, and ΔE is the energy difference between the MO and E_f (also shown in figure 2.7). A quick evaluation of equation (2.11) shows that it is very similar to equation (2.10). Thus, the MO-interaction with electrodes (tip & sample surface) plays an important role in determining both the strength of the adsorbate-surface bond and the through-adsorbate resonant tunneling current.

MO nodal-plane symmetry effects must also be considered, as well – as these are important factors which determine MO interaction with tip/substrate and ultimately the orbital contribution to tunneling. The dominant contribution of LUMO orbitals to resonance tunneling is a direct consequence of MO symmetry at the molecule-substrate interface.

When there is weak coupling in at least one of the electrodes (surface/tip) as is generally the case for STM, the MO are “highly localized” at the molecule, where they contribute significantly to tunneling. As described by Kaun and co-workers, this weak coupling typically results in ample opportunity for the electronic energy to

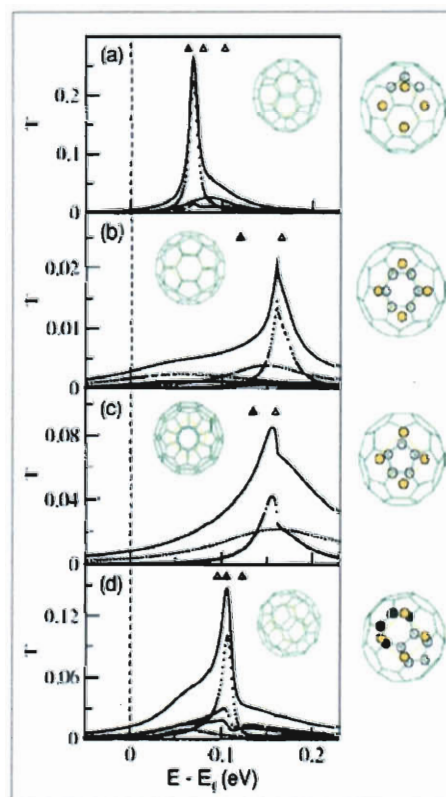


Figure 2.8. Tunneling (transmission) resonances of Au-C₆₀-Au molecular transistor junction with different orientations facing Au-electrode: (a) a 5-6 bond; (b) a hexagon; (c) a pentagon; and (d) a mixed configuration. Image modified from [132].

convert or channel into the vibrational modes of the molecule, due to long lifetimes associated with the initial electronic state.[130] Frontier (HOMO / LUMO) orbitals are not the only MO contributions to resonant tunneling. All molecular orbitals must be considered; in the case of C_{60} , up to 36 MO's make significant contributions to the tunneling process.[131]

The adsorbate molecule's orientation at the surface can also change the through-adsorbate tunneling resonances due to mismatched rotational symmetry of the molecule with the surface. In the theoretical study of the current-driven dynamics of a Au- C_{60} -Au molecular junction, Kaun and co-workers shows (figure 2.8) that the tunneling (transmission) resonance changes in amplitude, lineshape, and position as the orientation of C_{60} molecule changes between the Au electrodes.[132] In (a), the 5-6 bond of C_{60} is facing the Au-electrode surface; (b) a hexagon; (c) a pentagon; and (d) is a mixed configuration. The triangles at the top indicate tunneling resonance contributions from different the MO's of C_{60} . The right column represents the different

node (symmetry) patterns from s , p_z wavefunctions on the C_{60} molecule. These symmetry difference influence the C_{60} -Au-electrode coupling at

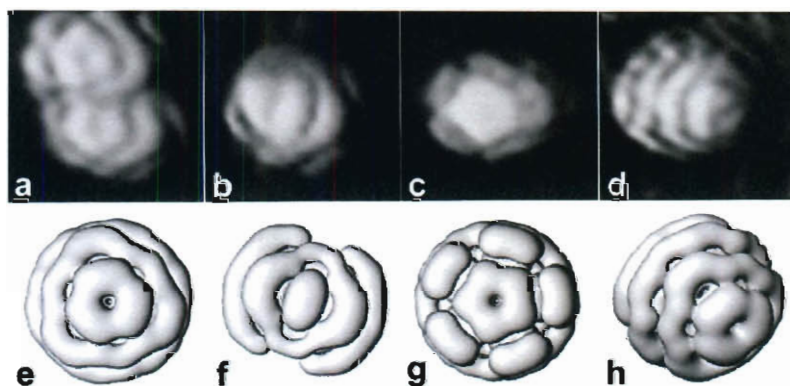


Figure 2.9. STM images of C_{60} on Si(111)(7×7) surface with (a) 3-fold, (b) 2-fold, (c) 5-fold, and (d) 3-fold molecular orientation. (e-h) are calculated images along respective symmetry axes. Image modified from [134].

the interface; the result is a change in tunneling resonance. The variations in MO coupling in this system directly apply to the internal structures of molecules observed with STM, as well.

For C_{60} adsorbed at the Cu(100) surface, Abel *et al.* use STM and x-ray photoelectron diffraction (XPD) to determine the monolayer growth patterns of C_{60} at the surface.[133] They observe along with C_{60} -induced surface reconstructions bright and dim C_{60} molecules across the surface. The dim C_{60} molecules exhibited a 3-fold LUMO orbital symmetry. Using XPD analysis, they determine that 2-inequivalent orientations of C_{60} sit at the surface – two 1-fold axes tilted toward 5- and 6-membered rings, respectively.

In a STM study of C_{60} adsorbed on the Si(111)(7×7), Pascual and co-workers experimentally show and verify the 2-, 3-, and 5-fold molecular orientations of C_{60} at the surface, as shown figure 2.9.[134] The experimental STM images are shown in figure 2.9(a-d) and the calculated structures are presented in figure 2.9(e-h). In a similar STM study, Grobis and co-workers look at the metallo-fullerene, $Gd@C_{82}$, on the Ag(100) surface.[135] They observe two metallo-fullerenes in close proximity on the Ag surface with two different orientations, as shown in figure 2.10. The molecular orientation is rotated 30 degrees with respect to the surface normal. As can be seen in figure 2.10, the differences in the internal structure between the two $Gd@C_{82}$ molecules are clear. Again, the differences cited in this study were again attributed to inelastic tunneling

processes in which the electronic states at the surface were coupled to the phonon vibrational modes of the molecule.

To-date, few STM studies have examined the effect of atomic and molecular adsorbates on spin-polarized (ferromagnetic) surfaces. In Chapter 4 of this dissertation, spin-

averaged STM measurements indicate a 3-fold orientation of C_{60} present at multiple locations on the Co(0001)

surface; and spin-polarized STM/STS detail the effect of C_{60} on exchange-split surface states at the Co surface.

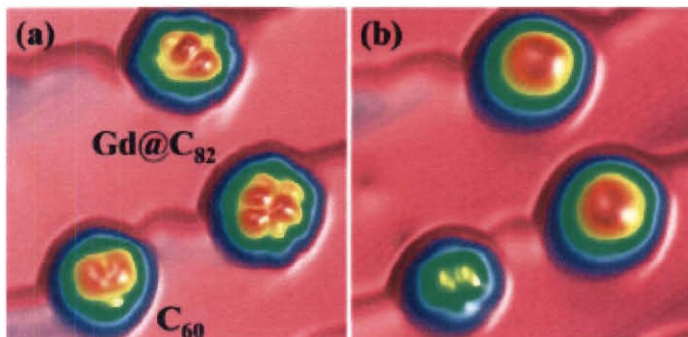


Figure 2.10. In STM topograph, two $Gd@C_{82}$ molecules with different orientations display different internal structure sit near a C_{60} molecule on a $Ag(100)$ substrate surface: (a) 0.1 V, (b) 2.0 V. Image modified from [135].

CHAPTER 3

INFLUENCE OF MOLECULAR C₆₀ ON Ni(100) AND Co(0001) FILM GROWTH

3.1 Introduction

C₆₀ fullerene-metallic nanosystems have been the subject of many recent scientific studies, as the unique physical and chemical properties of these composite systems (superconductivity, ionocovalent bonding) offer great potential in a wide array of device applications. Some of these applications include the use of C₆₀ fullerenes in molecular transistor junctions and giant magnetoresistance devices.[136] In each application, the C₆₀-metal interface plays a fundamental role in the functionality of the device.

However, the exact properties of C₆₀ critically depend on its structural environment. For example in the case of molecular transistor junctions, Kaun *et al.* show theoretical evidence that changes in the bond orientation of the C₆₀ molecule at the C₆₀-Au interface activate different tunneling resonance channels within the metal-fullerene device. Evidence of this has also been found experimentally for magnetic (C₆₀-Ni) transistor junctions. Furthermore, for magnetic Co-C₆₀/Fe-C₆₀ composite films, Zheng *et al.* show that the bulk magnetic properties of these thin films can be manipulated merely by the grain boundary concentration of molecular C₆₀.

Although each of the applications above promises great potential, the fabrication of functional devices has proven difficult and unreliable. Successful implementation of these fullerene-metal nanosystems as full-scale, functional devices hinges on both the structural stability of the system and the nature of the bond interactions at the interface. The growth of fullerene-metal superlattices is based entirely on the assumption of a strong bonding interaction between C₆₀-fullerene and the metal species involved. Strong bonding at the interface encourages epitaxy, required for the growth of atomically flat superlattices.

To maximize the true potential and properties of fullerene-metallic nanosystems, the physical phenomena that drive both the growth and interactions at fullerene-metal interfaces need to be understood. In this paper, the influence of C₆₀ on the initial growth of strained homoepitaxial Ni(100) and Co(0001) films is investigated by means of in-situ scanning tunneling microscopy (STM) combined with Auger electron spectroscopy (AES). The analysis will show that both the Ni and Co continue their crystalline growth unperturbed by the presence of C₆₀ adsorbed onto the strained film surfaces. Eventually, the molecular C₆₀ is encapsulated beneath the film surface, incorporating the C₆₀ molecule within the film network.

3.2 Experimental Procedures

Both the C₆₀/Ni/Cu(100) and the C₆₀/Co/Ru(0001) systems were grown in an ultra-high vacuum (UHV) chamber (base pressure $\sim 5 \times 10^{-11}$ mbar) equipped with low-energy electron diffraction (LEED), Auger electron spectroscopy (AES), and in-situ STM. A clean

Cu(100) substrate surface was prepared by repeated Ar⁺ sputter cycles performed at room temperature and 900 K, followed by a 5-minute flash anneal at 950 K in UHV.[137] The Ru(0001) substrate surface was prepared using 3 flash anneals in an O₂-ambient of 5×10⁻⁹ mbar, followed by 2 flash anneals in UHV. LEED and AES were used to verify the cleanliness of the substrate surfaces. STM topographs along with their corresponding LEED pattern and AES spectra are shown in figure 3.1. The topographs show atomically-flat terraces with widths of ~4000 Å and ≥5000 Å on the Cu (100) and Ru (0001) substrate surfaces, respectively. AES spectra [figures 3.1(b) and 3.1(d)] confirm the absence of any S (at 152 eV), O (at 503 eV), or C (at 272 eV) peak contamination on both the Cu(100) [920 eV] and Ru(0001) [273 eV] surfaces; and LEED patterns [inset of figures 3.1(a) and (c)] show bright delineated spots with a low background on both substrates. STM, AES and LEED all indicate high quality, atomically-flat Cu(100) and Ru(0001) substrate surfaces were prepared.

Ni and Co films were grown from metallic rods using an e-beam evaporation sources. The Ni films were grown to a total thickness of 7.6 ± 0.6 MLs at a deposition rate of 0.95 ML/min. Afterwards, the Ni films were then annealed at ~455 K for 30 mins. Co films were grown to a total thickness of 1.8 ± 0.2 MLs at a deposition rate of 0.23 ML/min. After deposition was complete, the Co films were annealed at 550 K for 8 minutes. After the films were grown, sub-ML amounts of C₆₀ fullerenes (MER-corporation, purity 99.9%) were sublimed from a quartz crucible held at 740 K onto a room temperature Ni(100) and Co(0001) film surface, respectively. The C₆₀ coverage was approximately

0.03 ML for Ni, and the C_{60} coverage was approximately 0.04 ML for Co, as determined from STM. The local effect of C_{60} on Ni and Co film growth was determined on each film (Ni, Co) surface, respectively, by depositing additional monolayers of Ni and Co at room temperature, post C_{60} growth. STM imaging of both the Co and Ni films was performed at room temperature. During STM imaging, the tip was grounded and sample bias was varied. Typically, the tip current setpoint was set at 20 pA to reduce tip-molecule interaction.

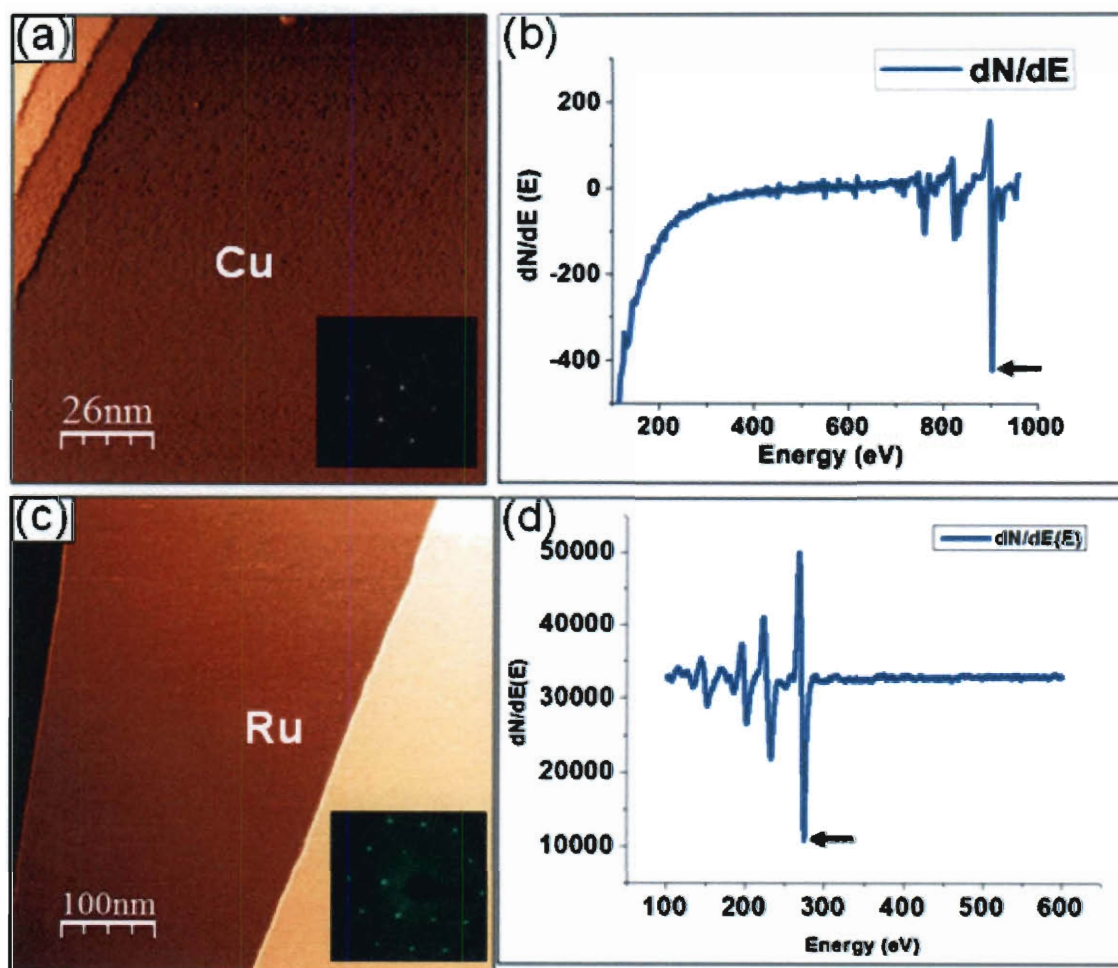


Figure 3.1. Topograph of (a,c) of Cu(100) and Ru(0001) substrate surfaces, respectively, post Ar+ sputter and anneal. (inset) shows LEED pattern for each substrate surface. (b,d) Auger spectra for each substrate. Black arrow indicates location of main peak for each substrate (Cu, 920 eV; Ru, 273 eV).

3.3 Results & Discussion

3.3.1 Sub-ML C_{60} coverage on annealed Ni(100) Films: Figure 3.2(a) shows a constant current STM image of a Ni film (thickness: 7.6 ± 0.6 ML) grown at room temperature.

The surface is relatively rough with multiple islands and 4-5 atomic layers exposed at the film surface, resulting from a multilayer growth mode. Figure 3.2(b) shows the same film after annealing at 455 K. The Ni film morphology has become much smoother with only two distinct levels present; the local coverage is now between 7 ML or 8 ML separated by a monatomic step. The upper Ni film terrace forms a network of coalesced

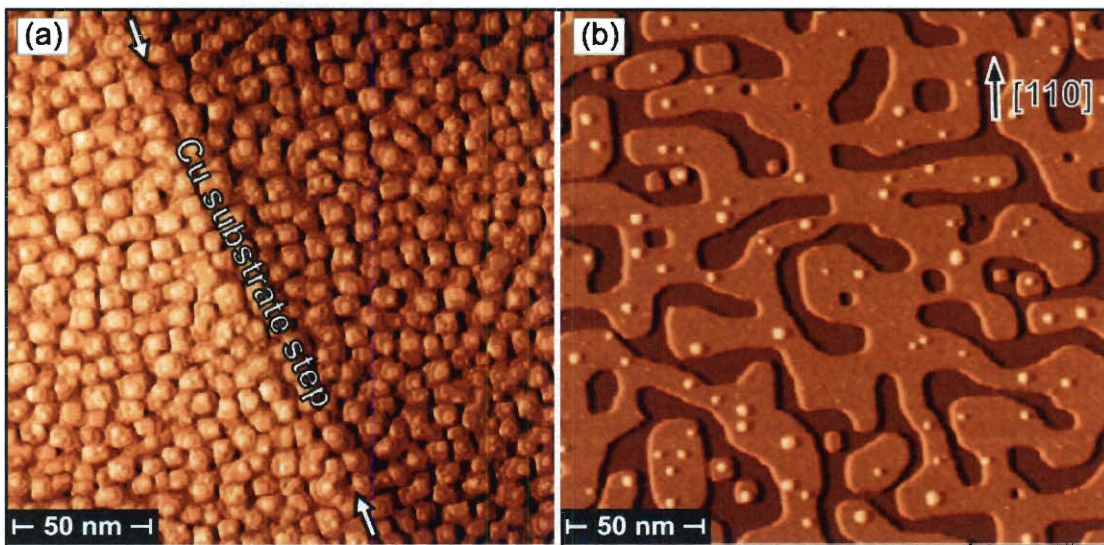


Figure 3.2. (a) Topograph of pre-annealed 7.6 ML Ni film grown on Cu (100) substrate at room temperature. (b) Ni film after a 20-minute anneal at 455 K; annealed Ni film surface has an atomically-flat upper and lower terrace, small Ni islands remain atop the upper terrace.

ridges which are roughly oriented along [110]-equivalent directions and up to 400 Å wide. Additionally, small Ni islands with a diameter of about 50 Å or less are observed on the upper Ni terrace.

As will be shown below, these small Ni islands will act as nucleation sites for adsorbed C_{60} . Auger spectra confirmed the absence of any S, O, or C-peak contamination on the Ni surface and LEED patterns of the post-annealed Ni-film showed bright well-defined spots with a low background indicating the high quality of the Ni(100) film.

After the Ni films were annealed, C_{60} was deposited onto the surface. Throughout this study, full monolayer (ML) coverage of C_{60} is defined as presence of 1.23 C_{60} molecules per square nanometer. Approximately 0.03 ML C_{60} were deposited onto a 7.6 ML Ni film, shown in figure 3.3. The C_{60} molecules preferentially

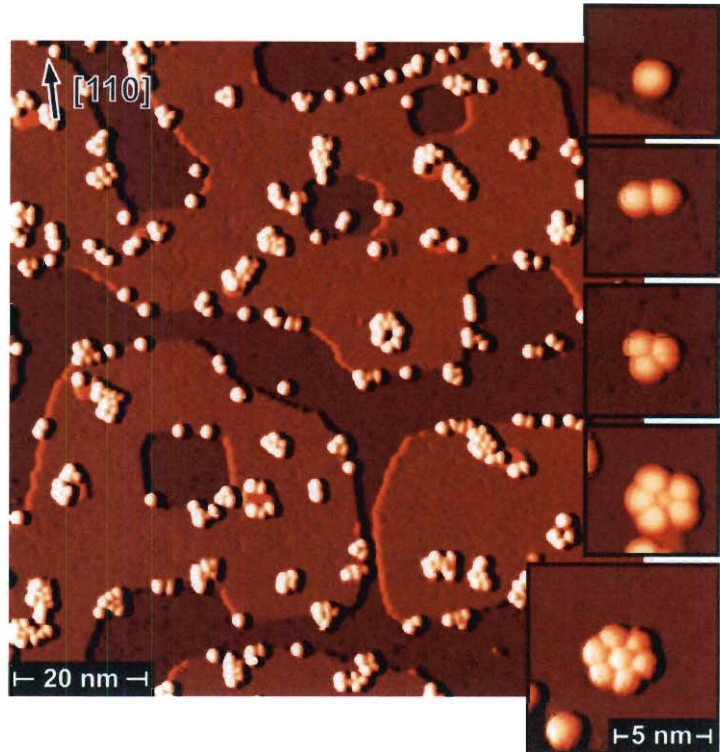


Figure 3.3. Topograph of 0.03 ML C_{60} adsorbed onto an annealed Ni(100) film surface. The insets on the right show a C_{60} monomer, dimer, trimer, pentamer, and a heptamer cluster (from top to bottom).

nucleate and cluster at Ni step edges, on the Ni terraces, and around small Ni islands. Many different molecular cluster sizes were found on the Ni surface. For example, an ordered heptamer that is a cluster of seven C_{60} molecules can be seen in figure 3.3(inset). Due to the smaller area occupied by the lower Ni terrace (local coverage 7 ML) and the absence of Ni clusters, C_{60} coverage and clustering is reduced except along

the Ni step edges. Across the top Ni film terrace (local coverage 8 ML), C_{60} coverage (nucleation) is fairly uniform with a high degree of molecular clustering. The uniform coverage and molecular clustering across the upper terrace are expected due to a relatively strong covalent bond interaction between the C_{60} molecule and the Ni surface, limiting the mobility of C_{60} at the surface. [138]

The average height of C_{60} molecules measured above the Ni film terrace is $7.2 \pm 0.2 \text{ \AA}$. Although the height measured by STM is smaller than the actual cage diameter of C_{60} (10.18 \AA), it is in agreement with similar measurements taken on other metallic surfaces. [139,140,141,142] The reduced apparent height of C_{60} is a consequence of the relatively low local-DOS at a given energy above the molecule linked to the coupling of C_{60} molecular orbitals to substrate states near the E_F surface. [143,144,145,146]

Beyond the heptamer, larger clusters of C_{60} , both ordered and disordered, can be observed on the Ni(100) film surface. Some ordered clusters are shown in the insets of figure 3.3. The observation of short-range quasi-hexagonal molecular ordering in the heptamer (bottom inset) is surprising at such a relatively low-temperature (300 K), given the high binding energy between C_{60} and Ni at the surface.[147] In this sense, the Ni(100) film surface differs from that of the bulk Ni(110) surface where C_{60} ordering only occurs at elevated temperatures ($\geq 540 \text{ K}$).[148,149] This may be attributed to the lower corrugation of fcc(100) surfaces as compared to fcc(110) surfaces which has higher corrugation. This makes C_{60} diffusion more difficult (and anisotropic) on the Ni(110)

surface due to the increased binding energy at this surface between the C_{60} and Ni. The intermolecular interactions of C_{60} lead to close-packed ordering at metal surfaces. [150]

At room temperature the C_{60} molecules and clusters showed limited to no mobility on the Ni(100) film surface. This was confirmed by imaging the same area on the Ni film surface over multiple cycles. While molecular dimer and trimer clusters of C_{60} were observed to be unstable (rotate about axis normal to surface plane) during imaging, no long-range mass molecular transport was observed during imaging for any molecular cluster on the Ni surface over a period of 45 minutes.

3.3.2 Ni Island Growth with 0.03 (Low) C_{60} Coverage: To understand how the presence of molecular C_{60} impacts film growth on the Ni(100) surface, we investigated the growth of Ni on annealed Ni(100) films pre-covered with molecular C_{60} . After each subsequent Ni deposition, successive STM images were taken at the same location. The thickness of Ni monolayer deposits at the surface was varied from 0.5 ML up to 7.5 ML.

In figure 3.4, the progression of Ni growth at the surface is followed after each subsequent deposition. In figure 3.4(a) and (b), topographic STM images show the same location before and after 0.5 ML Ni is deposited onto the Ni(100) surface, respectively. Upon the deposition of an additional 0.5 ML Ni, the average Ni island size is observed to be ≈ 4.2 nm (≈ 18 nm²) and the Ni islands are beginning to coalesce (figure 3.4b). The Ni islands tend to nucleate on both the upper and lower Ni(100) terraces. The presence of

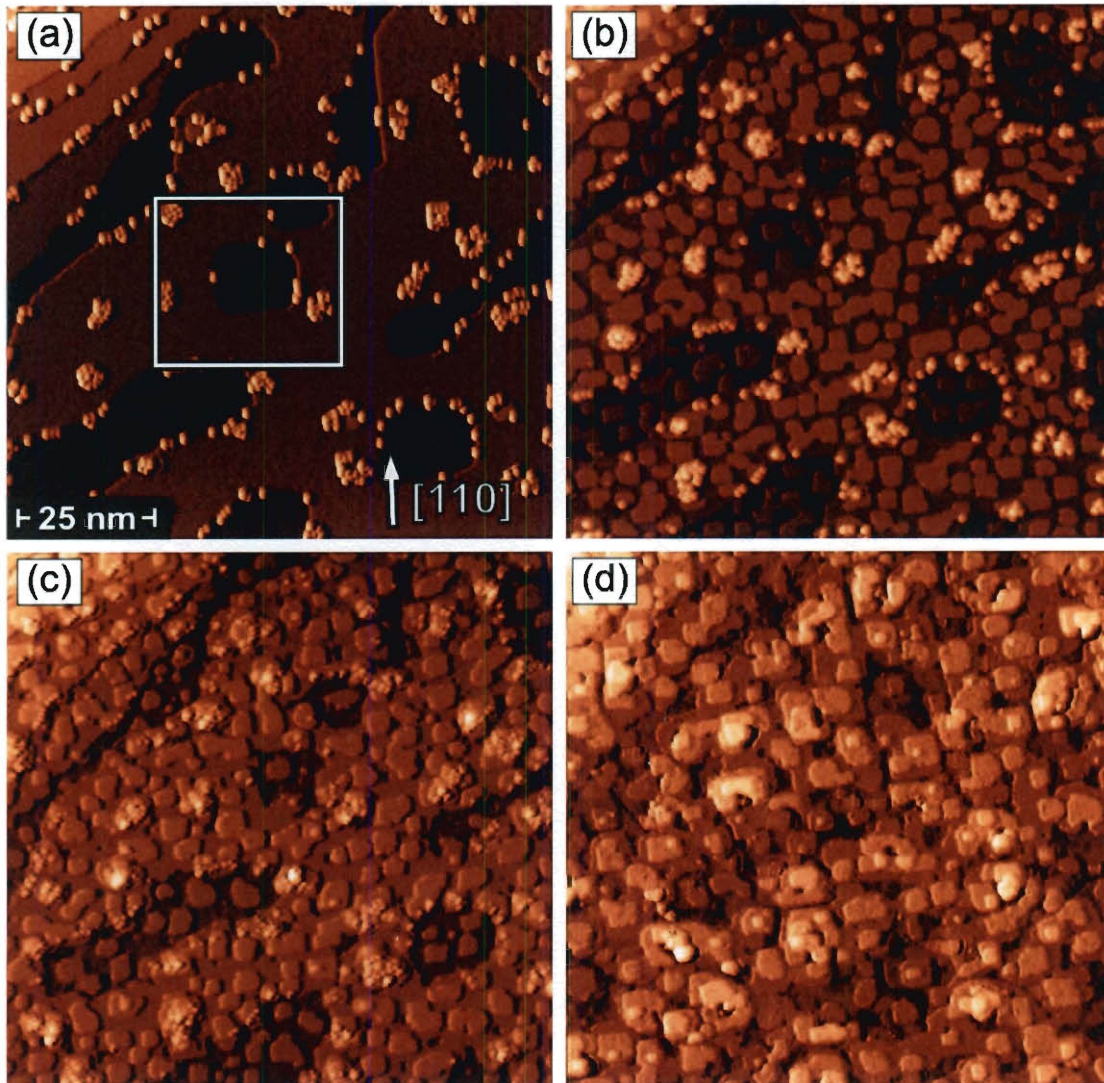


Figure 3.4. Topograph of (a) 0.03 ML C_{60} on Ni(100) film surface and after depositing (b) 0.5 ML, (c) 1.5 ML, and (d) 4.5 ML Ni onto the film surface. Ni nucleates on upper/lower terraces, at step edge. C_{60} molecules also serve as nucleation sites. Box in (a) encloses a section on the surface where Ni growth is followed (shown in figure 4 below.)

step edges or C_{60} has no obvious effect on the multilayered growth of Ni. The

nucleation of Ni islands away from regions on the surface where C_{60} is present indicates

that the Ni diffusion has a high energy barrier and suggests that the diffusion rate is too

low to adequately sample enough sites at the surface for Ni- C_{60} collisions to occur.

In regions on the Ni(100) terrace where no C_{60} is present, the Ni islands nucleate forming a square shape, consistent with previous growth studies of Ni/Cu(100) systems and also consistent with studies of homoepitaxial systems of Ni and Fe(100).[151, 152, 153] The square-shaped Ni islands are an indication of the ability of the impinging adatoms to preferentially diffuse along the [011] step edge direction (closed-packed).[154, 155] In regions on the Ni(100) film surface where C_{60} is present, Ni

adatoms treat the C_{60} molecules as alternative nucleation sites on the Ni film surface, forming islands around the edges of the molecular clusters. Ni islands that nucleate and grow around (encapsulate) the C_{60} clusters tend to take-on the general shape of the molecular

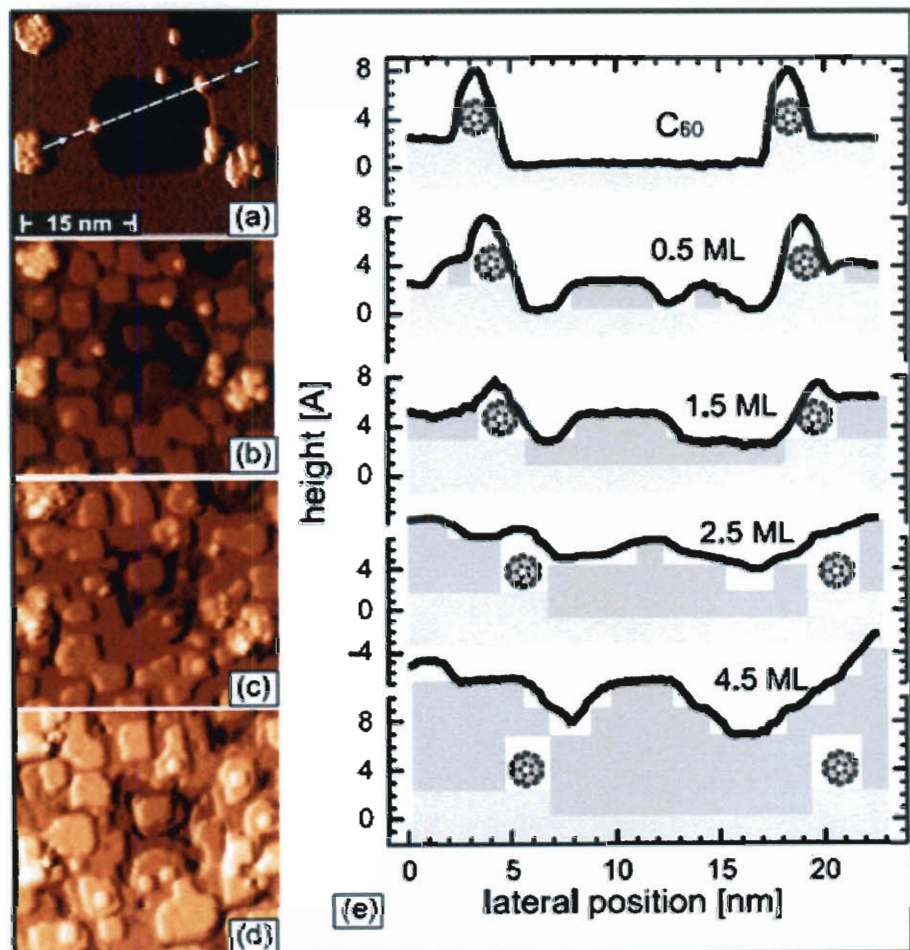


Figure 3.5. Topograph of (a) C_{60} on Ni(100) film surface and after depositing (b) 0.5 ML, (c) 1.5 ML, and (d) 4.5 ML of Ni deposited onto the film surface. (e) Sequential line section of the same location following Ni film growth with C_{60} at the surface.

cluster present at the surface, suggesting that at least locally the molecular C_{60} does influence Ni island growth at the surface. At 1.5 ML Ni, an additional monolayer Ni has grown on the Ni film surface with another partial monolayer exposed at the surface, as evidenced by the small islands on the larger terraces [figure 3.4(c)]. At approximately 2.5 ML Ni, only about 10% ($\sim 0.8\text{\AA}$) of the C_{60} molecule remains visible above the Ni film surface; and after the deposition 4.5 ML Ni, no C_{60} remains exposed on the surface [figure 3.4(d)]. Still as more Ni is deposited at the surface, remarkably, the growing Ni film maintains crystalline (epitaxial) growth, essentially uninterrupted by the presence of C_{60} .

The box drawn in the STM topograph of figure 3.4(a) indicates a region on the film surface tracked (shown in figure 3.5) along with its corresponding line section. Figure 3.5(a) shows a topographic STM image of a region on the Ni film surface where C_{60} molecules have adsorbed at the bottom edge of a Ni step; the dashed line represents the path of the corresponding line section taken, shown in figure 3.5(e). As more Ni is deposited onto the film surface (0.5 to 4.5 ML), the Ni islands nucleate and grow on both the upper and lower Ni(100) film terrace. However as shown in topographic images in figures 3.4(b)-(d) and the

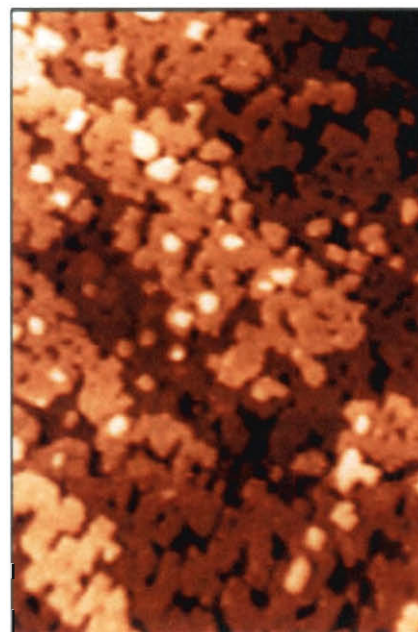


Figure 3.6. Topograph ($200\text{\AA} \times 400\text{\AA}$) of 3.8 ML Ni grown annealed Ni(100) film pre-covered with after 0.2 ML C_{60} . Epitaxial growth of Ni film continues at higher C_{60} coverages.

corresponding line sections in figure 3.5(e), the Ni islands also grow around the C₆₀ molecules, trapping the molecules along the lower edge of the Ni step. After 4.5 ML Ni have been deposited, the C₆₀ molecules are completely encapsulated beneath the surface of Ni.

At even higher C₆₀ coverages (up to 0.2 ML), the Ni film continues to grow with a remarkably high degree of crystallinity. At 0.2 ML C₆₀ coverage, the films were grown slightly above room temperature (~350 K). Figure 3.6 shows the Ni film morphology after 3.8 ML Ni were deposited onto the annealed Ni film surface. At 3.8 ML Ni, there is no evidence of C₆₀ at the surface; similar to what is observed at lower C₆₀ coverages (above). The atomically-flat Ni film terraces also appear wider and more coalesced (figure 3.6), as compared with the lower C₆₀ coverages due to the slightly elevated substrate growth temperature.

3.3.3 Auger Spectral Analysis of Ni Growth: In order to investigate if the C₆₀ molecules are being buried or diffuse on top of the film surface, we have performed a coverage-dependant Auger electron spectroscopy (AES) study. The AES study was performed with double-pass CMA. Additional Ni was grown onto annealed Ni(100) films pre-covered with 0.2 ML C₆₀, under very similar conditions as in the experimental procedures section, (base pressure 7×10^{-10} mbar). C₆₀ film coverage was determined by STM. Auger electron spectra were taken after adding successively 1 ML Ni onto the Ni film surface with 0.2 ML C₆₀ coverage. The peak heights were determined after background

subtraction. The C-peak height and the C-peak position are reported with their associated Ni-to-Cu peak ratios in Table 3.1.

Table 3.1.

C₆₀ C-peak position and height (normalized) after 0.2 ML C₆₀ deposited onto annealed Ni(100) film surface and after each subsequent Ni deposition, respectively. Ni-to-Cu peak ratio increases with each Ni deposition indicating the presence of more Ni, as expected.

Layer	Peak Position	Height	Ni/Cu ratio
C ₆₀ -Ni	259.8	5.77	0.885
1 ML Ni	263.5	4.85	1.337
2 ML Ni	265.0	4.49	1.447
3 ML Ni	266.7	3.57	1.598

The AES plot (figure 3.7) shows a clear shift in the C₆₀ C-peak position – termed in current literature an AES chemical shift. These chemical shifts are attributed to changes

in the chemical environment or the interactions of nearest neighbor atoms. As Ni is deposited onto the film surface, a reduction in the C-peak height and changes in the lineshape are also

observed. This attenuation of the C-peak is consistent

with the C₆₀ molecules slowly being buried below the Ni surface during deposition; due to the relatively short mean-free path of Auger electrons, even the first few atomic layers of Ni lead to a significant reduction of the C signal.[156] An explanation of the

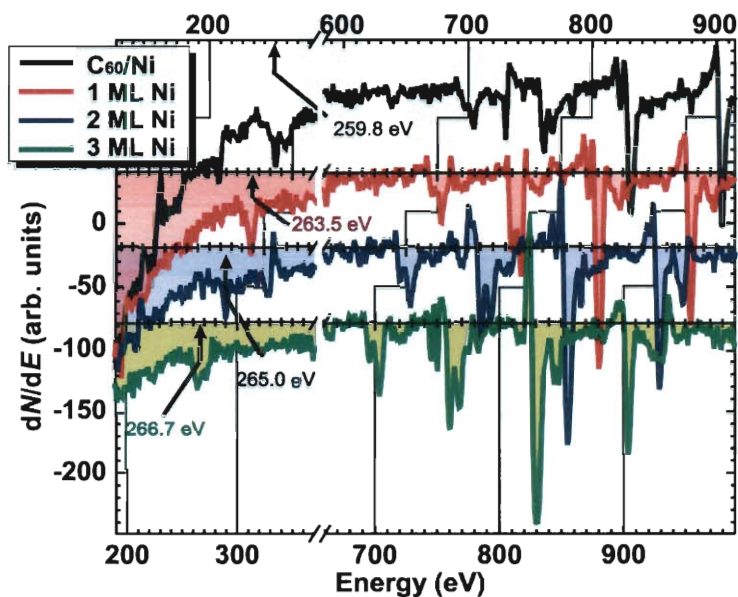


Figure 3.7. AES plots showing shifts in C₆₀ C-peak as 1 to 3 ML Ni are deposited onto the annealed Ni(100) film surface pre-covered with C₆₀. The Ni- and Cu-peaks are offset by 25eV in the plot for clarity.

changes observed in the C_{60} C-peak lineshape is less clear without more detailed theoretical / experimental studies.

For molecules, it is well-understood that changes in the AES (and XAS) lineshape can generally be attributed to changes in the molecular bond orientations at the substrate surface and many-body processes (unresolved vibrational excitations accompanying AES transitions within the molecule), which are the result of long-lived final states.

[157,158,159,160] The AES results presented here indicate the C_{60} molecules maintain their chemical integrity during the Ni growth, in good agreement with literature which reports the decomposition of C_{60} on Ni(110) surface occurs only at elevated substrate temperatures (≥ 750 K), well-above the temperatures used in this study.[161]

3.3.4 Co Film Growth & Morphology on Ru (0001) Substrate: Figure 3.8(a) and (b) show Co films grown on Ru(0001) substrate surface at room temperature before and after

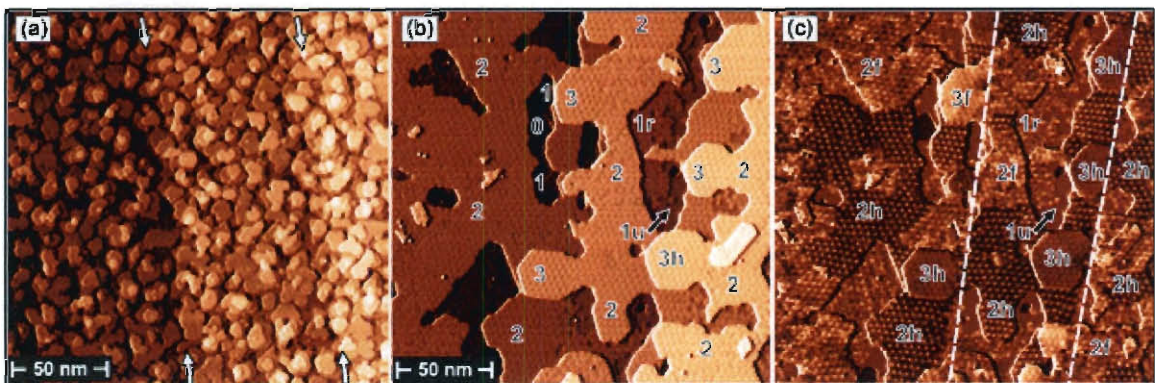


Figure 3.8. (a) Topograph of the pre-annealed Co(0001) film surface (arrows denote terraces of underlying Ru substrate). (b) Topograph taken from a different location on a post-annealed Co(0001) film surface. (c) Differential conductance dI/dV map of post-annealed Co film (dashed lines denote terraces of underlying Ru substrate). Unreconstructed and reconstructed regions on the 1st Co ML are denoted (u) and (r), respectively. The hcp- and fcc-stacked regions on the 2nd and 3rd Co ML are labeled (h) and (f), respectively.

annealing, respectively. The film thickness amounts 1.84 MLs. Pre- and post-annealed STM images are taken from different locations on the film surface. The Co films grown at room temperature on the Ru(0001) substrate display a very rough multilayer surface morphology, as shown in figure 3.8(a), similar to that of the pre-annealed Ni films (discussed above). However after the Co films are annealed, the morphology changes significantly (figure 3.8b). The resultant Co film surface is relatively complex and has atomically-flat terraces as wide as 500 Å.

In the post-annealed Co film, local coverages between 1 ML and 3 MLs can be found on the film surface, accompanied by regions on the surface where the Ru(0001) substrate is exposed. In the first Co monolayer, we find co-existing smooth and quasi-periodically corrugated regions with a lateral periodicity of about 35 ± 1 Å. These regions have different apparent heights of 1.82 Å and 2.34 Å above the Ru(0001) substrate terrace, respectively, and are labeled unreconstructed (u) and reconstructed (r), in figure 3.8(b).

We speculate that the reconstructed region is equivalent to the strain-driven formation of a dislocation network reported in a LEED study by Gabaly *et al.* performed under slightly different conditions, i.e. on films grown at an elevated substrate temperature of 523 K [162]. In this study evidence was found that film strain is relieved in the first Co monolayer only after the appearance of a temporary phase, which consists of a network of misfit dislocations. Gabaly *et al.* also observe that the phase change occurs only after approximately 0.9 ML Co have been deposited onto the Ru(0001) substrate surface at

523 K. It is described to be a “metastable” phase (dislocation network), which disappears within a minute. In contrast, the quasi-periodic corrugation pattern appearing in our STM images obtained at room temperature was stable for hours after the annealing process.

The existence of a stable quasi-periodically reconstructed (r) region in the first Co monolayer differs from the findings of Lundgren *et al.* for Co films grown on Pt(111).[163] In their study, dislocations in the first Co monolayer are lifted by the growth of the second Co layer. However as evidenced in figures 3.8(b), the areas of reconstruction observed in the first Co monolayer are stable and concomitant with regions showing no reconstruction. The reconstructed regions display a moiré pattern; and the presence of concomitant (r) and (u) regions within the first (and second) Co film monolayer suggests (i) that the partial-layer reconstruction (dislocation network) is not fully lifted by the second (or third) Co monolayer, respectively, and (ii) that the partially-reconstructed regions also play a role in relieving film strain energy within these monolayers. The differences we site in comparison are likely related to the nature in which our Co films are prepared.

With the exception of some tiny unreconstructed patches in the second monolayer, all higher coverages were found to be fully reconstructed and display a moiré pattern with a periodicity of $35 \pm 1 \text{ \AA}$. Although the local coverage across the Co film surface looks largely homogeneous in the topographic (constant-current) images, significant contrasts

could be identified in the differential conductance (dI/dV) maps measured at $U = -0.4$ V [Figure 3.8(c)]. Close inspection of the dI/dV map reveals that for both local coverages of 2- and 3-monolayer, two discrete signatures can be observed. The contrasts are caused by changes in the Co film's electronic structure. We believe that this variation in the local electronic structure originates from differently stacked regions.

It is well-known that variations of the stacking sequence in quasi-hexagonal surfaces (hcp vs. fcc) lead to energetic shifts of surface states and surface state resonances with $d_{3z^2-r^2}$ symmetry near the $\bar{\Gamma}$ point.[164,165,166] Closer analysis reveals that out of the five 3rd monolayer islands in figure 3.8(b), four were found to exhibit a low differential conductivity (labeled 3h) and only one exhibits a high differential conductivity (labeled 3f). A similar observation is made for the 2nd monolayer in figure 3.8(c), where histogram analysis of the Co film surface reveals that the hcp stacking is 78% and the fcc stacking is 22% in the second Co monolayer.

Since both the Ru substrate as well as the Co film are hexagonal in nature, we interpret (h) and (f) regions in the second and third monolayer as predominantly hcp- and fcc-stacked Co domains, respectively, where hexagonal stacking is more likely. Such stacking faults are quite common in hetero-epitaxial systems where both constituents exhibit a bulk hcp crystalline structure. The resultant moire patterns are the product of atomic surface distortions induced by the large lattice-mismatch (7%) between the Co film and the Ru (0001) substrate. The atomic distortions relieve the stress built-up

within the Co film and are mediated by the formation of a network of dislocation on the film surface.[167]

The stacking faults in moiré reconstruction patterns consist of Shockley partial misfit dislocations. These partial dislocations separate atomically-distorted hcp regions from fcc regions with atomic distortion, via on-top sites. Figure 3.9(a) shows the surface topography of a 3rd-ML Co terrace with moiré reconstruction. The bright lines in the surface topography are partial dislocations; these bright lines (dislocations) separate the fcc regions from hcp regions. As mentioned earlier, the moiré reconstructed terraces can contain predominantly fcc- or hcp-stacking, and this predominance is determined

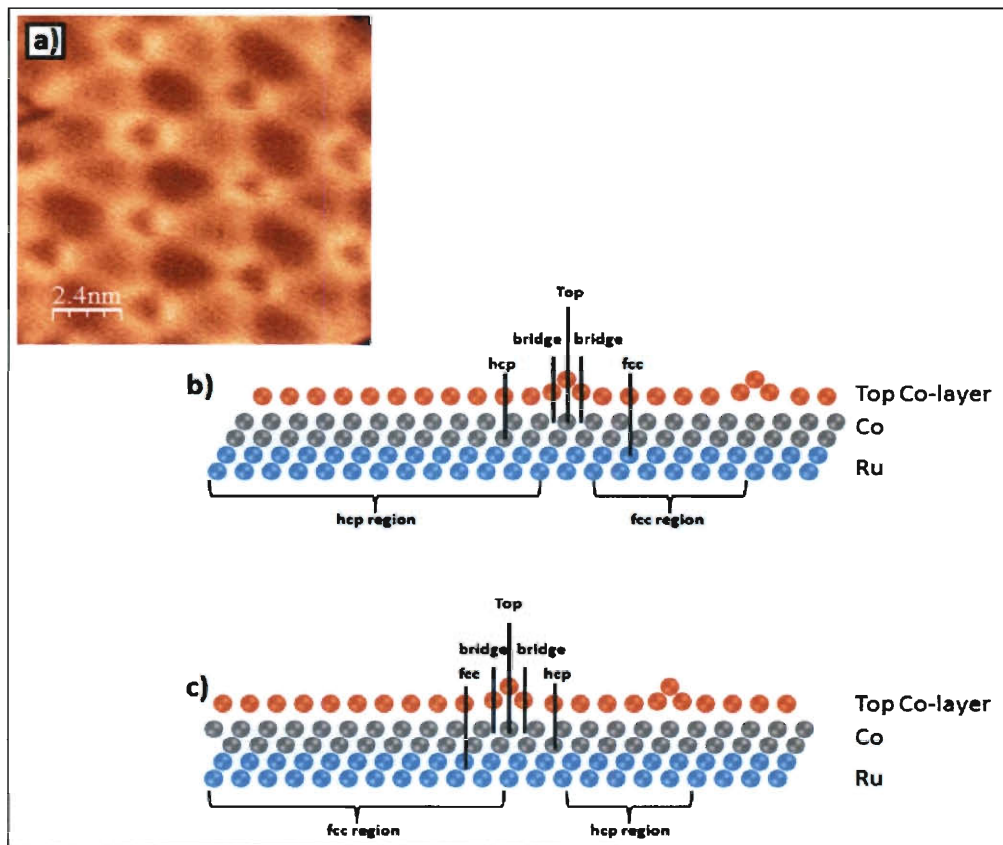


Figure 3.9. (a) Topography of 3rd-ML Co terrace with moiré reconstruction. (b) Model cross-section of moiré patterned Co terrace with predominantly hcp stacking. (c) Model cross-section of moiré patterned Co terrace with predominantly fcc stacking.

the overlayer stacking at the Co-Ru interface. As the Co overlayer grows, adatoms impinging on the Ru(0001) substrate surface can choose to stack at available fcc or hcp 3-fold atomic sites depending on which site is energetically most favorable. As discussed above for the Co-Ru thin film-substrate system, terraces with hexagonal stacking are observed to be the preferred form of growth in good agreement with previous studies. Model cross-sections of hcp- and fcc-favored moiré terraces are given in figures 3.9(b) and (c), respectively.

The changes observed in the moiré pattern across the Co film surface have a direct impact on the C_{60} interactions

with the film and will be discussed in more detail below.

Figure 3.10 shows a STM topograph of a Co film annealed at 660 K for 15 minutes. At this anneal temperature, the Co film shows a substantially different morphology. The 1st Co

monolayer is visible on the surface and shows a layered form of growth; the remaining Co on the

surface has agglomerated into large islands extending across multiple Ru substrate steps

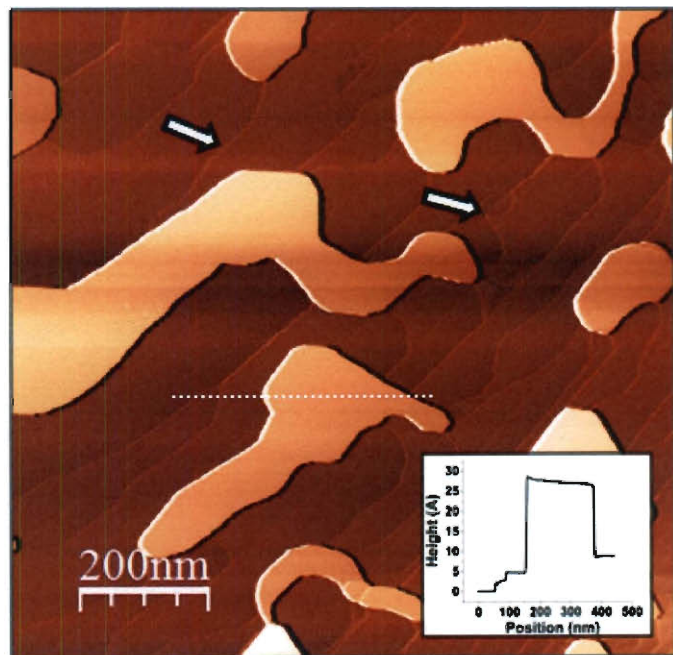


Figure 3.10. Topograph of 1.84 ML Co film annealed at 660 K showing a Stranski-Krotonov form of growth. Arrows indicate regions on surface with 1 to 2 ML Co; dashed line indicates location where line section was taken (inset).

(inset figure 3.10). The morphology on the surface is indicative of a Stranski-Krastonov (S-K) form of growth. A similar form of growth has been observed for Co(0001) films annealed at 500 K on W(110), as in highly stressed film systems S-K growth is thermodynamically more stable at elevated anneal temperatures – as at higher temperatures, kinetic constraints are removed and the thin film-substrate system is better able to approach equilibrium.[168] Only Co films annealed at 550 K were used in the remainder of this study, as they produced an ideal atomically-flat surface for this study. For more information on S-K growth, please refer to reference [169].

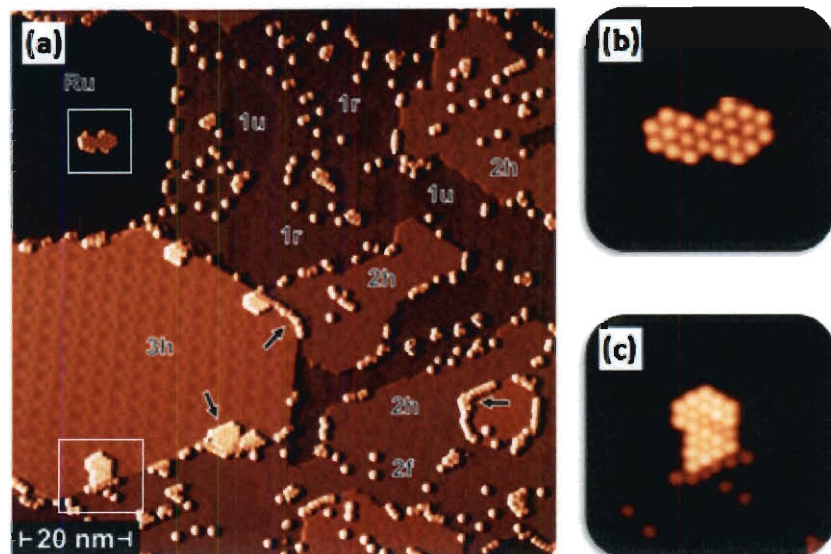
3.3.5 Sub-ML C_{60} coverage on annealed Co(0001) Films: After the Co(0001) films were annealed, sub-monolayers of C_{60} were deposited onto the film surface. Figure 3.11(a) shows a Co film covered by 0.04 ML C_{60} ; from this figure, it is evident that the C_{60} distribution across the surface is non-uniform. When C_{60} is deposited onto the Co film surface, the molecules should impinge onto the entire Co surface with equal probability and the resultant C_{60} -coverage uniform. However as will be discussed in detail below, the observed non-uniformity is a direct consequence of variations in the local film properties of Co. [170]

In the upper left corner of figure 3.11(a), a large quasi-hexagonal cluster of C_{60} sits atop a region on the surface where the Ru(0001) substrate is exposed (indicated by a white arrow) – a high resolution image is also shown in figure 3.11(b); small molecular chains of C_{60} have also adsorbed along the bottom step edge of the 1st Co monolayer. The C_{60}

molecules, adsorbed on both the Ru substrate surface and the Co film surface, exhibit a height of $6.8 \pm 0.1 \text{ \AA}$. No distinguishable height difference is observed for C_{60} adsorbed on Ru as compared with Co.

A relatively high number of monomer C_{60} sit adsorbed on top of the 1st Co monolayer. Many relatively small C_{60} clusters (3-5 molecules) are also present on the 1st Co monolayer. In contrast, no C_{60} is observed in the unreconstructed regions of the 1st Co monolayer. In figure

3.11, individual C_{60} monomers and small C_{60} clusters are also observed on the reconstructed regions of the 2nd Co monolayer.



However unlike the 1st Co monolayer, the reconstructed regions of the second Co monolayer may

Figure 3.11. (a) Topograph of 0.04 ML C_{60} deposited onto an annealed Co(0001) film surface shows C_{60} distribution is non-uniform across film surface. Unreconstructed and reconstructed regions on the 1st Co ML are denoted (u) and (r), respectively. The hcp- and fcc-stacked regions on the 2nd and 3rd Co ML are labeled (h) and (f), respectively. Boxed region in upper left corner (b) shows C_{60} cluster atop exposed Ru(0001) substrate surface. Boxed region in lower left corner (c) shows C_{60} molecules (bright) atop 3rd ML moire Co terrace; C_{60} molecules along step edge (darker) of 3rd ML Co terrace.

exhibit a different stacking, i.e. hcp and fcc. Very few C_{60} molecules seem to adsorb on the hexagonally stacked (2h) surface, likely due to high mobility of C_{60} in these regions.

In comparison, more C_{60} monomers and clusters can be found on fcc-stacked (2f) regions, where the dislocations impede the mobility of C_{60} molecules.

C_{60} molecules at a lower (0.02 ML) coverage on the annealed-Co surface are shown in figure 3.12. At 0.02 ML coverage, very few C_{60} clusters are observed on any Co monolayer; C_{60} monomers dominate the surface. The hcp (h) and fcc (f) regions on each

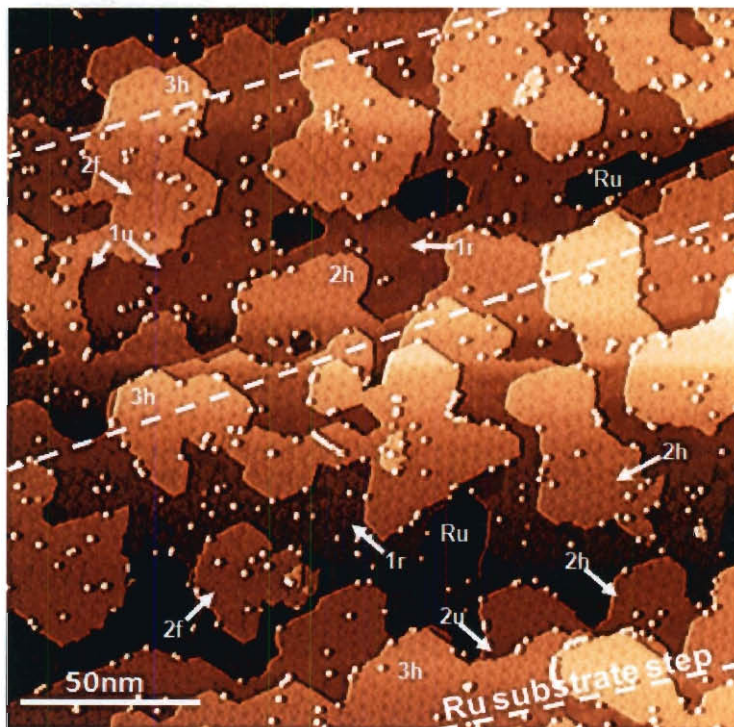


Figure 3.12. Topograph of C_{60} at a slightly lower coverage (0.02 ML) deposited onto an annealed Co(0001) film surface shows C_{60} distribution is non-uniform across film surface. Monomer- C_{60} dominates on the film surface.

Co monolayer are identified in the figure, as well. As discussed in the previous paragraph, very few C_{60} molecules adsorb in the hcp regions on the Co surface. In figure 3.12, this is true for both the 2nd and 3rd Co monolayer at the slightly lower 0.02 ML C_{60} coverage. Counting the number of molecules on the 2-ML terraces of Co and comparing

the number of molecules present within each (h) and (f) region (in figure 3.12), it is determined that for every 100 molecules on the 2-ML terraces 66% or more of those molecules occupy the fcc region on the surface. The high C_{60} mobility in the hcp regions does increase C_{60} non-uniformity on top of the 2nd monolayer Co. The high C_{60} mobility observed on the 2nd Co monolayer are directly applicable to the 3rd Co monolayer also, as explained below.

On top of the 3rd Co monolayer shown in figures 3.11(a) and (c), large quasi-hexagonal clusters of C_{60} (10 molecules or more) are observed only along the top terrace edge of the 3rd monolayer Co step (labeled 3h). The average lattice spacing measured between these molecules is 10.19 Å. The bulk lattice spacing of C_{60} is 10.18 Å. Van der Waal forces dominate molecule-molecule interactions in the bulk; the close agreement in lattice spacing suggests van der Waal forces dominate molecule-molecule interactions on the 3rd monolayer Co surface. Values for C_{60} lattice spacing at other locations on the surface can be found in Appendix [B].

In contrast to earlier observations on the 1st and 2nd monolayer surfaces, no C_{60} molecules are observed at the center of these 3rd monolayer Co terraces. A high number of C_{60} molecules are also adsorbed along the bottom step edge of these terraces, indicating the high C_{60} mobility in these regions. Again, higher C_{60} mobility in these (3h) regions correlates with the increased step decoration observed along the 3rd Co monolayer step.

The effect of Co (stacking/reconstruction) on C₆₀ mobility is also revealed by quantifying the percent monolayer coverage of C₆₀ on each Co layer at the surface. In the STM topograph of figure 3.11, Co occupies approximately 90% of the surface area, and the area covered by each of the three Co monolayers is relatively equivalent (1:1:1). The remaining portion (10%) of the surface is the exposed Ru substrate. As determined by STM, the C₆₀ coverage on the Ru substrate surface is 0.047 MLs. While our analysis shows that the C₆₀ coverage on Co monolayers 1 and 2 is 0.054 MLs, for the 3rd monolayer the C₆₀ coverage is determined to be 0.027 ML, nearly half the amount found on the Ru substrate surface and lower Co monolayers. The disparity observed in the local coverage of C₆₀ can only be explained by diffusion of the C₆₀ molecule across the 3rd monolayer step of Co from the upper terrace to the lower terrace. As the mobility of C₆₀ is limited on Co monolayers 1 and 2, step diffusion across these monolayers is negligible compared with Co monolayer 3. For C₆₀-coverage refer to Appendix [B].

3.3.6 Co Island Growth with Low C₆₀ Coverage: To determine how Co growth will proceed with C₆₀ present on the film surface, additional Co (0.2 ML - 1.6 ML) was deposited at room temperature onto the annealed Co film with 0.04 ML C₆₀ present at the surface. After each subsequent Co deposition, successive STM images were taken at the same location. The STM image in figure 3.13(a) shows C₆₀ molecules adsorbed onto a room temperature grown and annealed 1.84 ML Co film. As described in the previous section, the high mobility of C₆₀ on the 2nd and 3rd Co monolayer leads to step edge decoration. Indeed, the 3rd monolayer island in the top-right corner of figure

3.13(a) is surrounded by five C_{60} molecules. A line section crossing two C_{60} molecules and the third monolayer island is shown in the lower panel of figure 3.13(a). The apparent height of the C_{60} molecules in the profile indicates that it is adsorbed on the lower terrace that is the second layer.

On top of this surface, an additional 0.23 ML Co was deposited at room temperature. After the deposition, the same location was imaged by STM again [figure 3.13(b)].

Comparison of the STM images (upper panels) and corresponding line section (lower

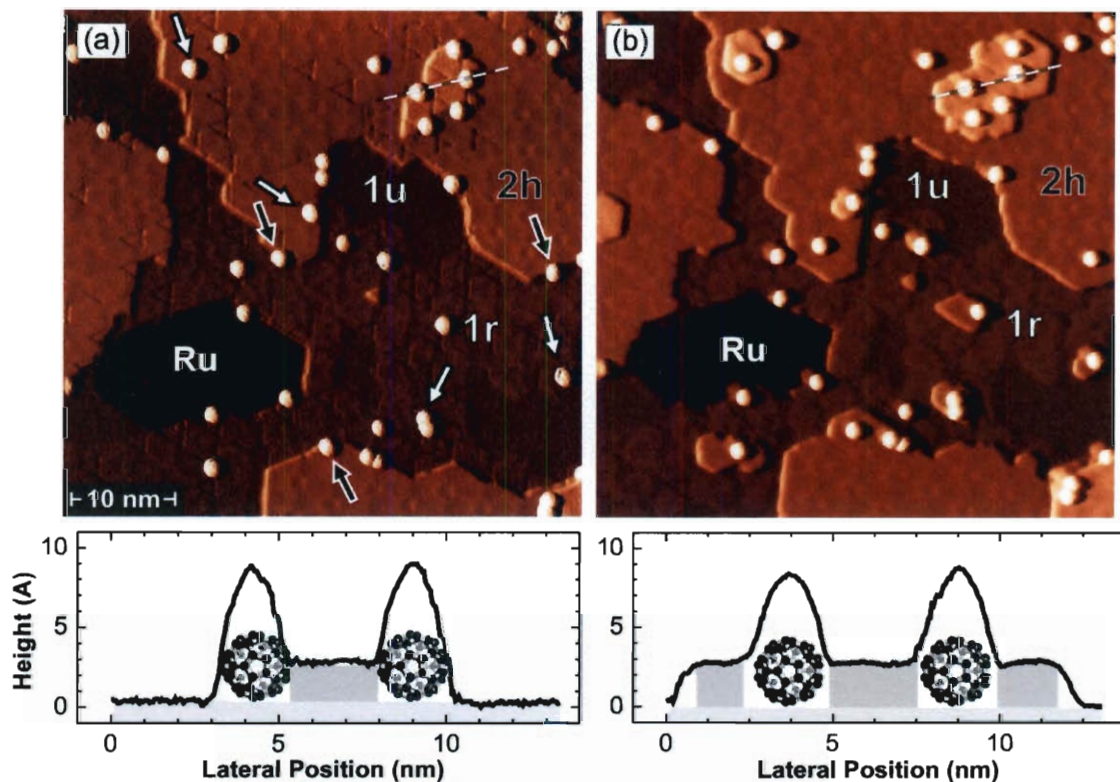


Figure 3.13. Topograph of Co film growth tracked in the same location before and after 0.23 ML Co is deposited onto the film surface (a,c). The dashed lines in STM topographs (above) indicate the position of corresponding line sections from the topographs (b,d).

panels) before and after growth indicates two processes: (i) the step edges of existing

islands are decorated with Co. The data indicate that the C_{60} molecules that were previously adsorbed at the step edges, remain at their original position. As a consequence, the C_{60} molecules appear to move inward (some examples highlighted by black arrows). (ii) Some C_{60} molecules act as nucleation sites for the formation of new Co islands in the second and third monolayer (white arrows).

However unlike Ni, Co atoms impinging on the film surface never nucleate on the bare Co terrace. Co island nucleation is only observed to precede from the step edges, via step flow, or around C_{60} molecules adsorbed on top of the film terrace. These C_{60} molecules behave like artificial nucleation sites for the Co

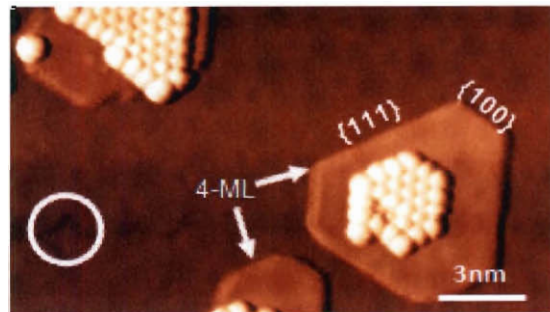


Figure 3.14. Topograph of large Co islands with $\{111\}$, $\{100\}$ step edge microfacets nucleated around C_{60} clusters on a Co film after 0.5 ML Co deposited. Arrows point to 4th ML on Co surface. Circled region on topograph points to a triangular dislocation network identified on the 3rd ML of Co film surface.

diffusing across the film surface; and as the islands grow and extend away from the C_{60} molecule, $\{100\}$, $\{111\}$ microfacets along the edges of the growing island begin to develop. The absence of Co-island formations away from molecular C_{60} or step edges indicates that the strength of the Co- C_{60} bond interaction (binding energy) is stronger and more stable than the Co-Co bond atop the film terrace.

In figure 3.14, 0.5 ML Co have been deposited onto the film surface. A fourth monolayer of Co has nucleated and continues to grow around clusters of C_{60} . The Co

islands extend approximately 3.4nm beyond the edge of the C_{60} cluster forming smooth atomically-flat islands with $\{100\}$, $\{111\}$ -type microfacets at the island edges. The higher adatom edge diffusion rate (lower diffusion barrier) along the $\{111\}$ -type step edge

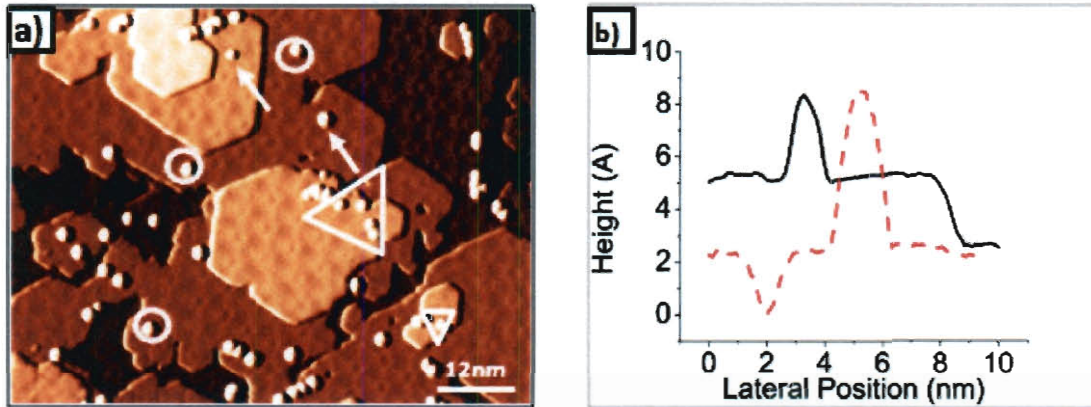


Figure 3.15. (a) Topograph of Co film surface after 1.6 ML Co deposited. Circled regions on topograph point to C_{60} molecules with 1 ML Co nucleated. Triangles point to molecules with 2 ML Co nucleated. Arrows point to molecules on the surface where (b) line sections were taken (line sections taken in the direction of white arrows). 2 ML Co nucleated around C_{60} (black solid line); 1 ML Co nucleated around C_{60} (red dotted line).

microfacets, as reported by Jacobsen *et al*, leads to the anisotropic hexagonal island shape observed.[171,172,173] In contrast with earlier observations (discussed above), C_{60} molecules have nucleated forming ordered clusters at the center of a third monolayer (moiré) terrace. In this figure, dislocation networks are observed on the 3rd monolayer Co terrace. These dislocation networks (sinks) are atypical on the third monolayer Co surface and may play a role in the formation of the C_{60} clusters observed. More studies are needed to understand the role of these dislocation networks play in the formation of these large C_{60} clusters at the surface.

After the deposition of 1.6 ML Co, the Co islands begin to coalesce and form terraces 160 Å in width [shown in figure 3.15(a)]. These films were grown at room temperature, similar to the pre-annealed Co films discussed earlier (figure 3.8). However unlike the pre-annealed Co films, the Co films grown, here, continue to grow with the same morphology of the underlying annealed Co film surface. The film growth is crystalline, similar to the Ni growth (described above). The terraces remain atomically-flat with a majority of the coalesced terraces displaying a moiré-reconstructed surface. The C₆₀ molecules present on the surface continue to act as pseudo-nucleation sites for the diffusing Co atoms at the surface, and the molecules combine rather coherently within crystalline network of the Co film. Line sections (figure 3.15b) show that the height of C₆₀ molecules above the film surface has decreased after 1.6 ML Co has been deposited. Many of the C₆₀ molecules are still surrounded by 1 ML Co. However, a few molecules at the surface have a second monolayer of Co nucleated around them. A third monolayer of Co nucleated around the C₆₀ was not observed for the 1.6 ML Co coverage.

3.4 Summary

The effect of C₆₀ on film growth and morphology was studied using STM for both the Ni/Cu(100) and the Co/Ru(0001) systems. C₆₀ molecules deposited onto the Ni(100) film surface were observed to be fairly immobile and were uniformly distributed across the Ni film surface. On Co(0001) film surfaces, we observe regions on the surface where C₆₀ is highly mobile and regions where mobility is severely limited, resulting in a non-

uniform distribution of C_{60} molecules across the Co film surface. Despite the presence of C_{60} molecules on the Ni surface, the C_{60} shows no obvious effect on the crystalline (pseudomorphic) Ni film growth, as a high Ni diffusion barrier is shown to limit the occurrence Ni- C_{60} collisions at the Ni surface. AES results suggest the C_{60} molecules maintain their chemical integrity during Ni growth. For Co films, Co islands only nucleate and grow from the step edges and locally around C_{60} molecules which serve as pseudo-nucleation sites. The strength of the Co- C_{60} bond interaction appears stronger than the Co-Co bond on Co film terrace. The Co films continue to grow as crystalline films with well-defined reconstructed (moiré) terraces. These findings demonstrate that the nature of the C_{60} -metallic bond at the surface does influence the film growth and structure of these pseudomorphic thin film systems.

CHAPTER 4:

SPIN-AVERAGE & SPIN-POLARIZED SCANNING TUNNELING MICROSCOPY / SPECTROSCOPY OF BARE Co FILMS & C₆₀-ADSORBED Co FILMS GROWN ON Ru(0001)

4.1 Introduction

The interactions of C₆₀ molecules with transition and noble metal surfaces have been the subject of intense study for many years, due to the unique chemical and physical properties that these systems display and their potential for use in microelectronic technologies. However in recent literature, C₆₀ molecules adsorbed at the surface of ferromagnetic metals has received little attention. Some studies have explored the structure and binding energy of C₆₀ at the Ni(110) and Ni(111) surfaces.[174,175] However in these studies, little information is gained regarding the local spin-polarization effect of C₆₀ at the surface. The nature of these C₆₀ interactions may have important implications in molecular transistor junctions. To establish the nature of the spin-polarized interactions of C₆₀ molecules at the Co(0001) surface, the local magnetic properties (i.e. magnetic anisotropy and domain structure) of clean post-annealed Co and Co in the presence of C₆₀ were determined using spin-polarized scanning tunneling microscopy and spectroscopy techniques (SP-STM/STS). The experimental results are presented here in Chapter 4.

4.2 Experimental

The Ru(0001) substrate was prepared using the same procedure, as described above in the experimental section of Chapter 3. The Ru substrate was flash annealed 3-times in an O₂-ambient of 5.0×10^{-9} mbar, and followed with 2 flash anneals in UHV at 1.2×10^{-10} mbar, both at 1800°C. The Co films were deposited in an ultra-high vacuum environment (base pressure of 1×10^{-11} mbar). The Co was evaporated from a rod heated via electron bombardment and deposited at a rate of 0.23 ML/min onto a Ru substrate held at 77 K. The deposited Co films then underwent a 250°C anneal for 8 minutes. The total thickness of the Co films grown in this study was 1.84 ML, as determined by STM. These samples were then placed onto the He-cooled STM sample stage and cooled to 77 K prior to SP-STM/STS analysis. Conductance (dI/dV)-curves were collected using a lock-in amplifier technique.

Clean Fe-coated W-tips which are predominately magnetized in-plane were used in this study. The W tips were first flashed in ultra-high vacuum, using e-beam heating, prior to Fe deposition onto the tip. Approximately 140 Å Fe was evaporated from a rod heated via electron bombardment onto the tip. The tip was then annealed at 493 K for 10 minutes. Prior to any SP-STM/STS analysis imaging, the tip was allowed to cool to room temperature.

4.3 Results and Discussion

4.3.1 Co(0001) Film Growth & Morphology: As stated in the experimental section (above), Co films used in the spin-polarization study were grown at a low-temperature (LT), 77 K, and annealed. Figures 4.1(a) and (b) show STM topographs of post-annealed Co films grown at room temperature (RT) and LT, respectively. While some minor differences, regarding the exact island size and coalescence, and overall film morphology (roughness), might exist between the two Co films, the morphology of the RT- and LT-grown Co films is qualitatively very similar. Local coverage for Co grown at LT varies between 1 ML to 3 ML, along with small regions where the underlying Ru substrate is exposed, similar to the Co films grown at RT.

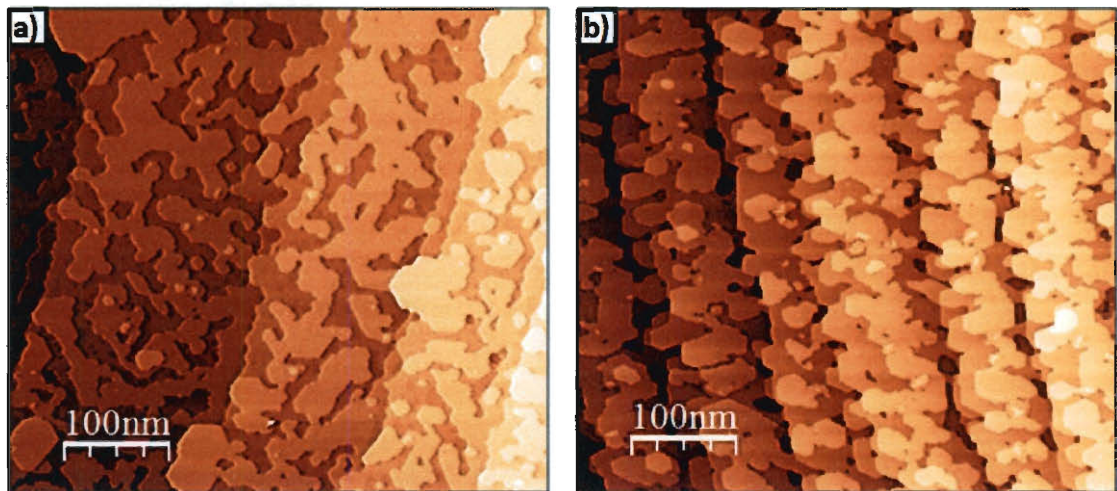


Figure 4.1. STM topographs of post-annealed Co films grown at (a) RT and (b) 77 K. Large atomically-flat terraces present on both film surfaces.

Both films show the presence of reconstructed (r) and unreconstructed (u) regions within the 1st Co monolayer. Small unreconstructed regions on the 2nd Co monolayer are present in LT films, and the 2nd and 3rd Co monolayers each contain hcp (h) and fcc-stacked (f) regions. Given that most of the differences observed in the morphology are

due to step density, it is evident that during the annealing process the RT- and LT-grown Co films lose their memory, i.e. the initial structure and morphology of these films becomes unimportant. In this study, the LT-grown films were considered suitable for the spin-polarized STM analysis. For a more detailed discussion on the Co film growth and morphology, please refer back to Chapter 3.

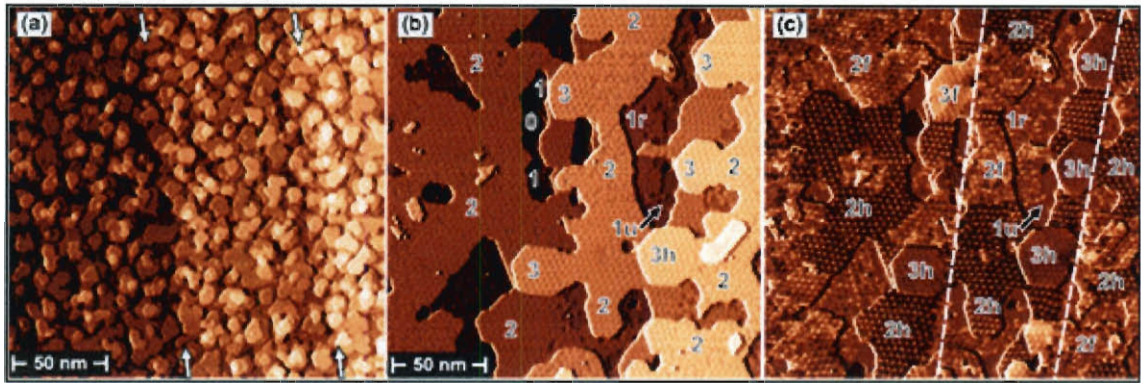


Figure 4.2. (a) Topograph of the pre-annealed Co(0001) film surface (arrows denote terraces of underlying Ru substrate). (b) Topograph of post-annealed Co(0001) film at different location. (c) Differential conductance dI/dV map ($V_b = -0.4$ V) taken from (b) - dashed lines denote terraces of underlying Ru substrate. Unreconstructed and reconstructed regions on 1st Co ML are denoted (u) and (r), respectively. The hcp- and fcc-stacked regions on the 2nd and 3rd Co ML are labeled (h) and (f), respectively.

4.3.2 Spin-Average Electronic Structure of Co Films on Ru(0001): In the following experiment, the spin-averaged electronic structures of the annealed Co films were studied using scanning tunneling spectroscopy. A STM topograph and a corresponding spectroscopic-map [spin-average conductance (dI/dV)] of the same region are shown in figure 4.3(a) and (b), respectively. The STM topograph has a 100 nm^2 scan area; the spectroscopic map [figure 4.3(b)] has a scan area of $96 \times 56 \text{ nm}$ with dI/dV -curves taken at each pixel in the scan. The dI/dV -data were collected using lock-in detection at room temperature with a 20 mV (rms) input ac-signal added to the sample bias.

In the topograph, the first, second and third Co monolayers are present on the surface. In the second Co monolayer, fcc (f) and hcp (h) regions are identified [figures 4.3(a) and (b)]. The boxes in 4.3(a) indicate areas on the surface where the dI/dV -curves were taken. As described above, the bright contrast regions in figure 4.3(b) correspond to fcc-stacking (f) and the dark contrast regions correspond to hcp-stacking (h) of the Co film. The spin-averaged dI/dV spatial maps were collected over a 11-hour time window explaining the presence of drift in image.

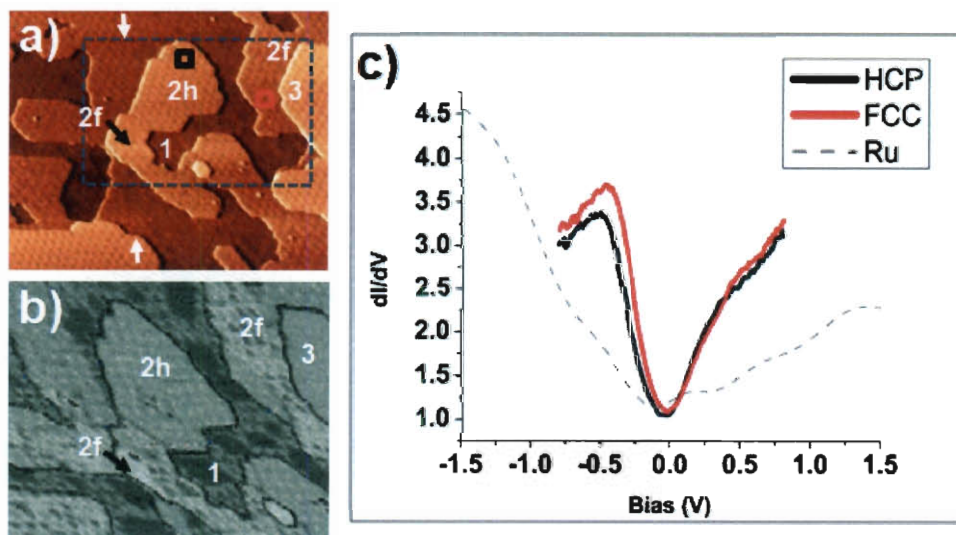


Figure 4.3. (a) Topograph of 1.84 ML Co(0001) film. hcp (h) and fcc (f) regions present on Co surface. White arrows indicate location of underlying Ru substrate step. Red (black) box indicate regions on surface where spatially-averaged dI/dV -curves were taken (b) Corresponding spatially-resolved dI/dV -map from same region ($V = -0.4$ V). Bright contrast regions identified as fcc; dark contrast regions identified as hcp. (c) Spatially-averaged dI/dV -curves taken from fcc (red curve) & hcp (black curve) regions.

In figure 4.3(c), the dI/dV -curves of the (h) and (f) regions on the Co film are plotted along with the dI/dV of the bare Ru(0001) substrate. The dI/dV -curves taken from these two

regions both have high background intensity, typically due to tip-induced effects. The Ru substrate is observed to be featureless and does not contribute to the spectroscopic features of the Co film. The dI/dV -curve taken from the fcc-stacked region (red curve) shows a peak -0.473 eV below the Fermi surface. The dI/dV curve taken from the hcp-stacked region (black curve) has a peak located at -0.499 eV below the Fermi surface. A reliable measurement of peak shift was not determined as due to the high tip-induced background and peak broadening effects related to temperature / size (rms) of ac-input signal. The peak height in the fcc region is also observed to be higher than in the hcp-stacked region indicating that the DOS ($dI/dV \propto$ LDOS) in the fcc-stacked is indeed higher than in the hcp-stacked regions. The maximum contrast observed between the fcc-stacked region and the hcp-stacked regions is defined as:

$$C_{f,h} = \frac{(dI/dV)_f - (dI/dV)_h}{[(dI/dV)_f + (dI/dV)_h]/2} \quad (4.1)$$

The maximum contrast, here, is calculated to be $C = 12.1\%$. The dI/dV -curves correlate well with the contrast shown in figure 4.3(b) [also shown in figure 3.8(c)].

As discussed briefly in Chapter 3, the contrast identified in the spin-average conductance (dI/dV) maps at $U = -0.4$ V, shown in figure 4.2 [also shown in Figure 3.8(c)], originates from changes to the Co film's surface state electronic structure. These observed shifts in the surface state electronic structure are caused by (i) an increase in the atomic-layer thickness of the film; as the Co film thickness increases, its bulk electronic structure is not fully complete until the 4th or 5th monolayer.

[176,177,178] The electronic shifts observed are also induced by local variations from (ii) unreconstructed and reconstructed regions found in the 1st Co monolayer and (iii) local variation in the Co film stacking sequence of the film (hcp vs. fcc). The experimentally observed electronic shifts due to stacking have been associated with weaker surface state and surface state resonance coupling (minority character, $d_{3z^2-r^2}$ symmetry near the $\bar{\Gamma}$ point) to the bulk d -band in other systems.[179] Each of these contributions may affect the contrast, however theoretical calculations are needed to determine the significance of each contribution in the Co/Ru(0001) system.

In current STS literature although some debate exists regarding the exact origins of the Co(0001) peak, there is general agreement that the peak derives from d_{z^2} - like surface state and has minority character. In a STS study, Okuno *et al.* identify a peak on the Co(0001) surface at -0.43 eV and assign this peak to a Γ -centered (please reference Appendix [A] for definition of Γ -point location within reciprocal space brillouin zone), d_{z^2} - like surface state with minority character.[180] In two other studies by Diekhoner *et al.* and Pietzsch *et al.*, a localized peak with similar (minority) character for the Co/Cu(001) system is identified, however the peak is located at 0.31 eV below E_F . [181,182] Pietzsch *et al.* also reveal a stacking-induced surface state peak shift of -70 meV for islands with fcc stacking compared hcp-stacking.

For Co grown on the W(110) surface, Wiebe *et al.* report a peak located at -0.3 eV below E_F and using first-principles calculations attribute the peak to a $d_{z^2-r^2}$ - like surface state resonance located near (off) the Γ -point. From their calculations, they also identify a pure surface state peak -0.5 eV below E_F (minority-spin character). This surface state is centered at the Γ -point, but makes a negligible contribution to the peak resonance found at -0.3 eV.[183] Wiebe *et al.* also identify a peak shift of -55 meV for fcc-stacked Co versus Co with hcp-stacking. In this study, spin-average surface state peak positions, for the fcc-regions (-0.473 eV) and the hcp-regions (-0.498 eV), were measured at room temperature and are close to the pure surface state peak (-0.5 eV below E_F) identified by Wiebe and co-workers.

The discrepancies cited in this and other studies can be partially explained by (i) film stress; and (ii) the influence of substrate interface effects, i.e. hybridization and intermixing, on the electronic structure of ultra-thin Co(0001) films. Substrate intermixing effects can be neglected in this study as intermixing effects are only valid at high temperature.[184] However, a recent study by Bork *et al.* shows clear evidence of a correlation between the d-band surface state peak position and degree of hybridization between the adlayer and the substrate bulk sp-bands.[185] Each of the factors discussed above, (stacking, substrate hybridization, stress) can have a tremendous influence on the position of the surface state peak observed.

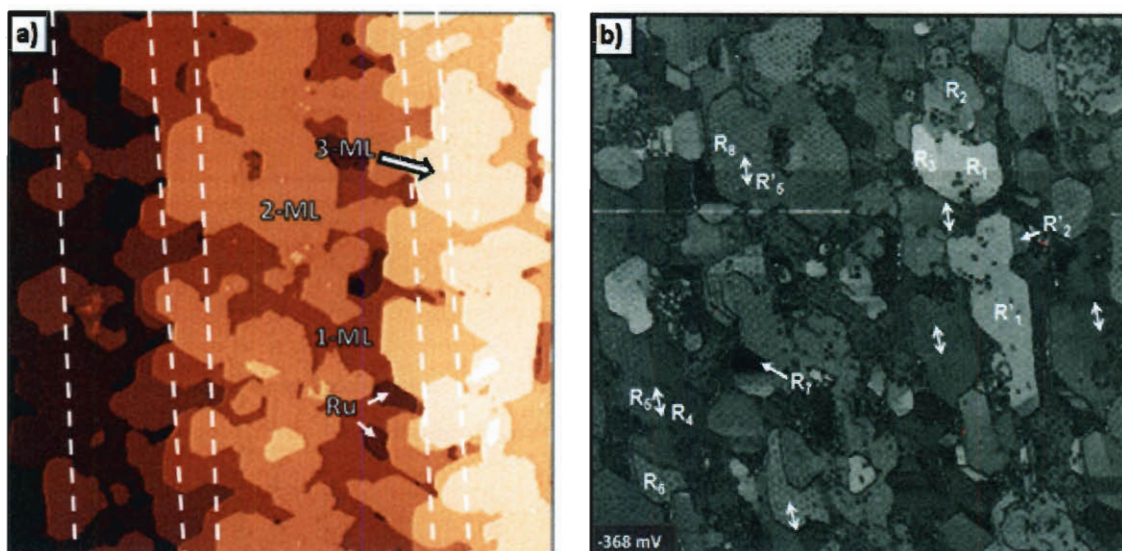


Figure 4.4. (a) 250nm×250nm STM topograph of post-annealed Co grown at 77K. dashed lines indicate location of underlying substrate step. (b) Corresponding spectral map from same area (double arrows indicate locations/direction of underlying substrate step). Refer to table 4.1 for specification of unique individual contrast regions.

4.3.2.1 Spin-Polarized Electronic Structure of Co Films on Ru(0001) Results: For the

spin-polarized electronic study of Co, the Co films were grown at 77 K and were annealed at a temperature of 550 K. In figure 4.4(a), a STM topograph of a post-annealed film shows that three Co monolayers are present on the surface, along with regions on the surface where the Ru substrate is exposed. The local Co coverage is identified in the figure. The dashed lines indicate the locations of underlying substrate steps. As discussed above in section 4.3.1, the Co film surface shown in figure 4.4(a) is very similar to the Co films grown at RT. All STM scans and spin-polarized spectroscopic maps and dl/dV -curves were collected using lock-in detection at 77 K (stabilization parameters: $I = 2$ nA, $V = 1.4$ V) with a 20 mV (rms) input ac-signal added to the sample bias. A Fe-coated W-tip was used to collect spin-polarized data in this study.

A spin-polarized spectral (SP- dI/dV) map of the same region is shown in figure 4.4(b). The STM topograph has a 250 nm^2 scan area; the spectroscopic map [figure 4.3(b)] has a pixilation of 304×304 with a dI/dV -curve taken at each pixel. Eight different contrast regions (R_i) are identified in the spectral map [figure 4.4(b)] and will be discussed in greater detail below; at the end of the results section, Table 4.1 (on page 86) contains a summary defining the source of contrast from each region (R_i). As observed in addition to the contrast present on the Co surface caused by layer (fcc/hcp) stacking, there is an additional magnetic contrast induced by the spin-moment alignment of the Co surface with the spin-moment of Fe-coated tip.

For these two magnetic materials – the Co surface and the Fe tip, the magnetic signal [i.e. magnetoresistance or spin-polarized tunneling current (I_p)] is not only determined by spin alignment between the tip/surface ($I_p \propto M_T \cdot M_S$, where M_T and M_S are the magnetization of the tip/sample, respectively). The I_p also has additional contributions which may derive from the electronic band structure of the tip/sample bulk and surface and the symmetry of individual electronic states and may derive from the small differences in magnetic potential experienced by electrons of different spin (\uparrow/\downarrow) as they scatter normal across a magnetic (tip/sample) interface.[186]

Since the Co surface is negatively spin-polarized and Fe has a positive surface spin polarization, a sharp increase in the tunneling conductance occurs when the Co film's spin-moment is anti-parallel to the spin-moment of tip. [187,188] When the Co film's

spin-moment is aligned parallel with the tip, the tunneling is reduced greatly as electrons tunneling from the Co film are spin-down in character and the empty states of Fe are spin-up; as during the tunneling process, spin must be conserved. By this reasoning, regions on the Co film surface [shown in figure 4.4(b)] with bright contrast are identified as magnetic domains with spin-moment alignment anti-parallel to the tip.

Regions on the Co film surface with dark contrast are identified as magnetic domains with parallel spin-moment alignment to the tip. The additional contrast observed in the figure 4.4(b) is not observed in the spin-averaged electronic Co studies, discussed above in section 4.3.2. As shown in the spectroscopic map of figure 4.4(b), the spin-polarized electronic structure of the Co is fairly complex, complicated by the influence of sequential layer stacking (fcc/hcp), strain-induced reconstruction (moiré), and the evolving electronic structure of individual Co monolayers. In the following paragraphs, the contributions to each of these individual contrast components labeled in figure 4.4(b) will be discussed.

Spatially-averaged dI/dV -curves taken from regions highlighted by the colored boxes are shown in figure(s) 4.5 – 4.10. In each, the spectrum of a clean Ru substrate surface is plotted (the Ru substrate spectrum is featureless and does not contribute to the contrast features identified in the dI/dV -curves). In figure 4.5(a), a bright (bottom) region on the Co surface is juxtaposed next to a dark region (top). The vertical arrows in figure 4.5 indicate the location of an underlying substrate step. To the

left of the step the Co is 3 ML thick; to the right of the step the Co is 2 ML thick. Both the top and bottom regions in the spectral map have hcp-stacking. To the right of the step, as indicated in figure 4.5(a) by the vertical arrows, the Co remains 2 ML thick.

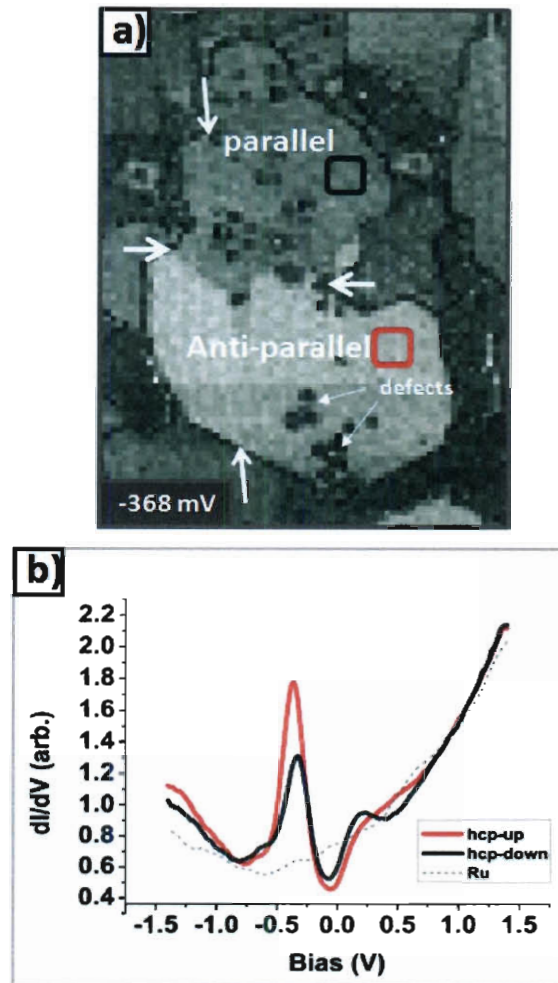


Figure 4.5. (a) Spin-Polarized dI/dV -map of hcp region on Co surface. Vertical (horizontal) arrows indicate location of underlying substrate step (location of magnetic domain boundary). Bright (dark) contrast region is anti-parallel (parallel) to tip moment. Red (black) box indicate the $hcp_{\uparrow\downarrow}$ ($hcp_{\uparrow\uparrow}$) region where (b) spatially-average dI/dV -curves were taken. Peak intensity from $hcp_{\uparrow\downarrow}$ region (red curve) is higher compared with peak from $hcp_{\uparrow\uparrow}$ region (black curve).

Therefore, no contrast between these two regions (top/bottom) is expected for a spin-averaged dI/dV -map. However, dark/bright contrast is observed between the top/bottom regions. By reasoning, the source of the contrast observed in this figure is magnetic and identifies magnetic domains on the Co surface with spin-moments aligned parallel (dark) and anti-parallel (bright) to the tip. The horizontal arrows in the figure indicate where the two domains meet. Here, no contrast difference can be seen across the step.

The dI/dV -curves from each region are shown in figure 4.5(b). The tip-induced background, as seen in figure 4.3, is absent from dI/dV -curves presented in figure 4.5(b). In the bright contrast region (red), a peak appears at -0.368 eV below E_F , and the dI/dV -curve from the dark contrast region (black) has a peak at -0.324 eV below E_F . The peak shift as we move from the region with an anti-parallel spin-moment (bottom) to a region with a parallel spin-moment is 44 meV shift up. The peak height from each region is also different, resulting in a calculated magnetic contrast difference for the different regions (hcp $\uparrow\downarrow$ / hcp $\uparrow\uparrow$) of $C = 29\%$. An additional surface state peak also appears 0.1 eV above E_F [figure 4.5(b)] and shows majority character.[189]

Taking another look at this island, figure 4.6(a) shows a topographic map of the exact same region on the Co surface. Moving from the 2 ML region (right) across the step to the 3 ML region (left), a change in the moiré pattern is observed. The observed change in the moiré pattern is not associated with a different stacking (hcp/fcc) sequence

across the step but can in principle be linked to the depth at which the dislocations sit (i.e., at the Ru/Co interface or at higher levels).[190,191,192]

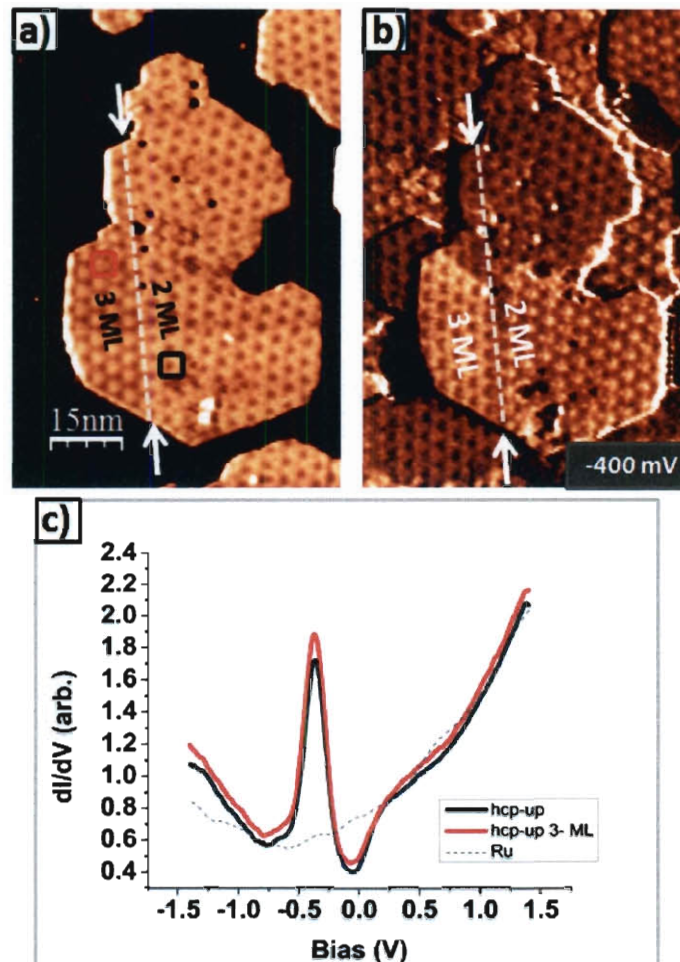


Figure 4.6. (a) STM topograph showing atomically-flat 2 ML Co film terrace across substrate step (indicated by dashed line). Red (black) box indicates regions where spatially averaged dI/dV -curves were taken. (b) Spin-Polarized dI/dV -map ($V_b = -0.4$ V) of hcp region on Co surface. Bright (dark) contrast region is anti-parallel (parallel) to tip moment. (c) Peak intensity from 3 ML hcp $\uparrow\downarrow$ region (red curve) is slightly higher compared with peak from 2 ML hcp $\uparrow\downarrow$ region (black curve). Peak height has minimal offset for clarity.

In figure 4.6(c), spatially-averaged dI/dV -curves taken from a 2 ML hcp $\uparrow\downarrow$ -region and 3 ML hcp $\uparrow\downarrow$ -region on the Co surface are shown. The location/direction of underlying

substrate step is indicated by arrows. The 3 ML hcp $\uparrow\downarrow$ -region occupies the exact same peak location, -0.368 eV, as the 2 ML hcp $\uparrow\downarrow$ Co region (reported above). Therefore, it is apparent that the layer stacking across the underlying step is consistent (hcp). Only a slight contrast difference is observed in the peak height across the substrate step. The resulting contrast is $C = 6.2\%$, in close agreement with spin-averaged spectroscopic studies performed Wiebe *et al.*, who observe contrast differences across Co(0001) monolayers grown on W(110) ranging from less than 10% up to 20%.[193] Figure 4.6(b) shows a dI/dV spatial map taken in constant current mode. Here, the contrast difference can be seen across the step.

Comparing figures 4.5(a) and 4.6(b), the contrast across the step in each image is different. No contrast is observed across the step in figure 4.5(a); contrast is observed across the step in figure 4.6(b). The dI/dV -map in figure 4.5(a) was collected in constant-height mode; the dI/dV -map in figure 4.6 was collected in constant-current mode. Comparing the two image collection modes, the lack of contrast in figure 4.5(a) and presence of contrast in figure 4.6(b) is due in-part to the voltage difference during data collection, but is also related to differences that exist in the LDOS across the surface which may result in height-induced tunneling current modulations of the STM signal caused by changes in the width of the tunneling barrier, as described by Crommie and co-workers.[194,195]

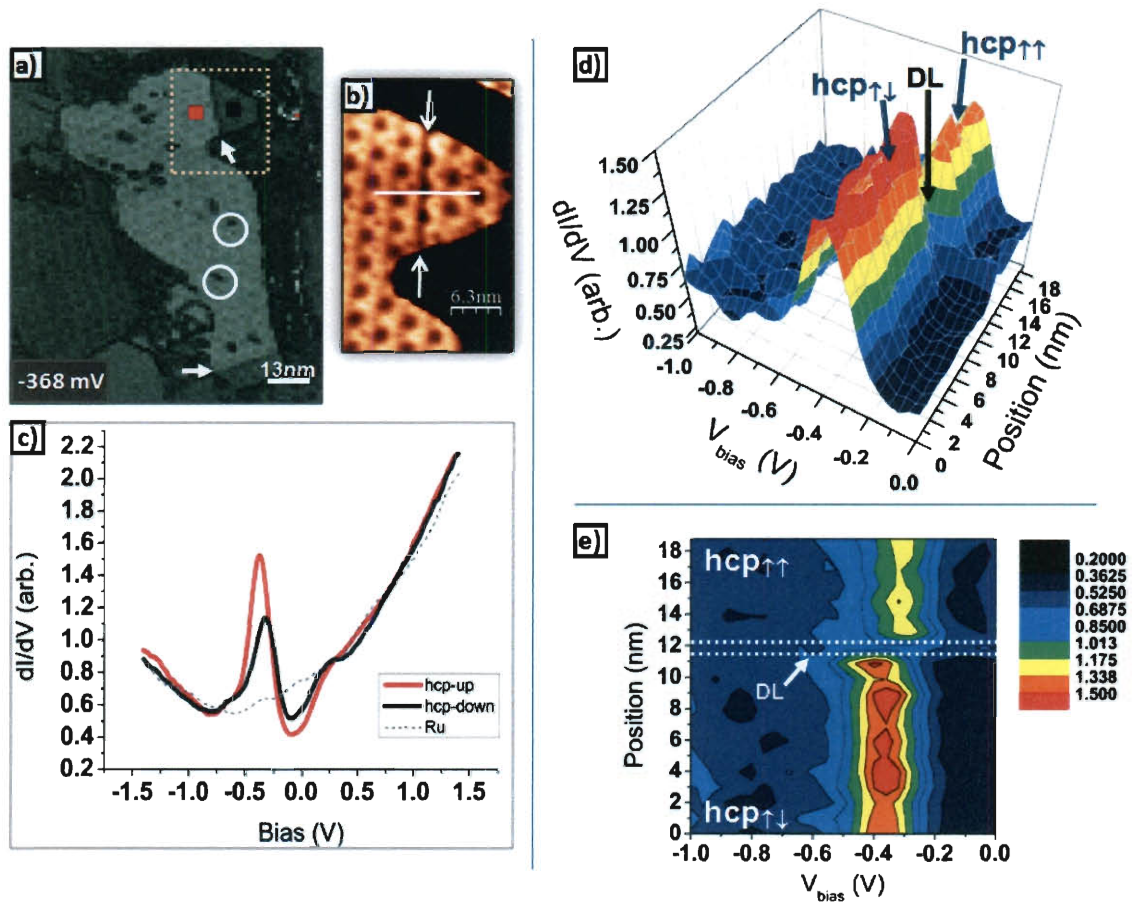


Figure 4.7. (a) Spin-polarized dI/dV -map of hcp region on Co surface. Bright (dark) contrast region is anti-parallel (parallel) to tip moment. Circles indicate defects in Co film surface. Arrows indicate location of dislocations (DL). Dashed box indicates region where (b) STM topograph is taken showing location of DL on 2 ML Co film terrace. Red (black) box indicates regions where (c) spatially averaged dI/dV -curves were taken. A line section [horizontal line in (b)] taken from the spectral-map in (a) shows absence of surface state peak over DL in surface and contour plot (d, e).

Figure 4.7(b) shows a STM topograph of a surface dislocation (DL) on the Co film surface. In the topograph, the region to the left of the DL has been identified as an hcp-stacked region (above), and the stacking remains hcp on right side of the DL. The film thickness is 2 ML on both sides of the DL. A corresponding spin-polarized spectral map is shown in figure 4.7(a), and spin-polarized dI/dV -curves spatially-averaged over regions to the left (red box) and to the right (black box) of the DL the dislocation, respectively, are shown in figure 4.7(c).

Upon first observation, it is observed that the dI/dV -curves in figure 4.7(c) are very similar to the curves discussed in figure 4.5. The peak from the bright (red) region is located -0.368 eV below E_F , and the peak from the dark (black) region is located at -0.324 eV below E_F . The peak heights from both regions (bright/dark) are approximately 14% lower than those observed in figure 4.5 (likely due to a tip change). However, the contrast difference across the DL is $C = 28.7\%$. Since, the peak positions and contrast observed in figure 4.7(c) mimic the dI/dV -curves described in figure 4.5, the source of contrast from this region is also identified as magnetic with the bright and dark regions corresponding to hcp $\uparrow\downarrow$ and hcp $\uparrow\uparrow$, respectively. However interestingly, the magnetic domain wall separating the two magnetic domains (hcp $\uparrow\downarrow$ / hcp $\uparrow\uparrow$) at the surface has been pinned by a dislocation line present at the Co surface. This pinning of magnetic domain walls by dislocation lines is observed in multiple locations on the Co film surface.

As further evidence of dislocation-pinned magnetic domain walls, a line-section taken from the spectral map of figure 4.7(b) demonstrates how the spin-polarized surface state peak changes as the Fe-coated tip is stepped across the DL region [figure 4.7(d)] on the Co surface; a corresponding 2-D contour map is also shown in figure 4.7(e). As can be seen in figures 4.7(d) and (e), as the STM tip (Fe-coated) is stepped from the bright (hcp $\uparrow\downarrow$) region over the DL and into the dark (hcp $\uparrow\uparrow$) region, the surface resonance peak at hcp $\uparrow\downarrow$ (-0.368 eV) disappears while positioned directly over the DL; and the Co surface state resonance peak reappears at -0.324 eV as the tip is stepped into the dark (hcp $\uparrow\uparrow$) region. The absence of the surface state peak is evident in both figures 4.7(d) and (e). Note also that in figures 4.7(d) and (e) the peak intensity (dI/dV) is greater in the hcp $\uparrow\downarrow$ region compared with the hcp $\uparrow\uparrow$ region [as shown in figure 4.7(b)]. Although the origin of the contrast (peak loss) over the DL is currently unknown, spin-orbit coupling effects at the DL and strain may have a strong influence on the spin-moment alignment along the DL and local Co band structure, respectively.

In figure 4.8(a), a spectroscopic map of an fcc region on the Co surface is identified. The dashed line in the image indicates the location of an underlying Ru substrate step running vertically through the image. The bright region to the left of the substrate step is 2 ML Co and the dark region to the right of the step is 1 ML Co. In the bottom left region, a DL identified by arrows in the image runs horizontally across the 2 ML Co terrace and continues across the step [shown in the inset of figure 4.5(c)]. The DL separates two contrast regions (upper/lower) in the 2nd Co monolayer. Contrast in the

lower (upper) region is brighter (darker). The closed (open) boxes indicate regions on the 2nd ML (1st ML) where spatially-averaged dI/dV -curves were taken. Spatially-averaged dI/dV -curves from the closed box (red/black, 2nd ML) regions are plotted in figure 4.8(b), and dI/dV -curves from the closed box (black, 2nd ML) and open box (red, 1st ML) regions are plotted in figure 4.8(c), respectively.

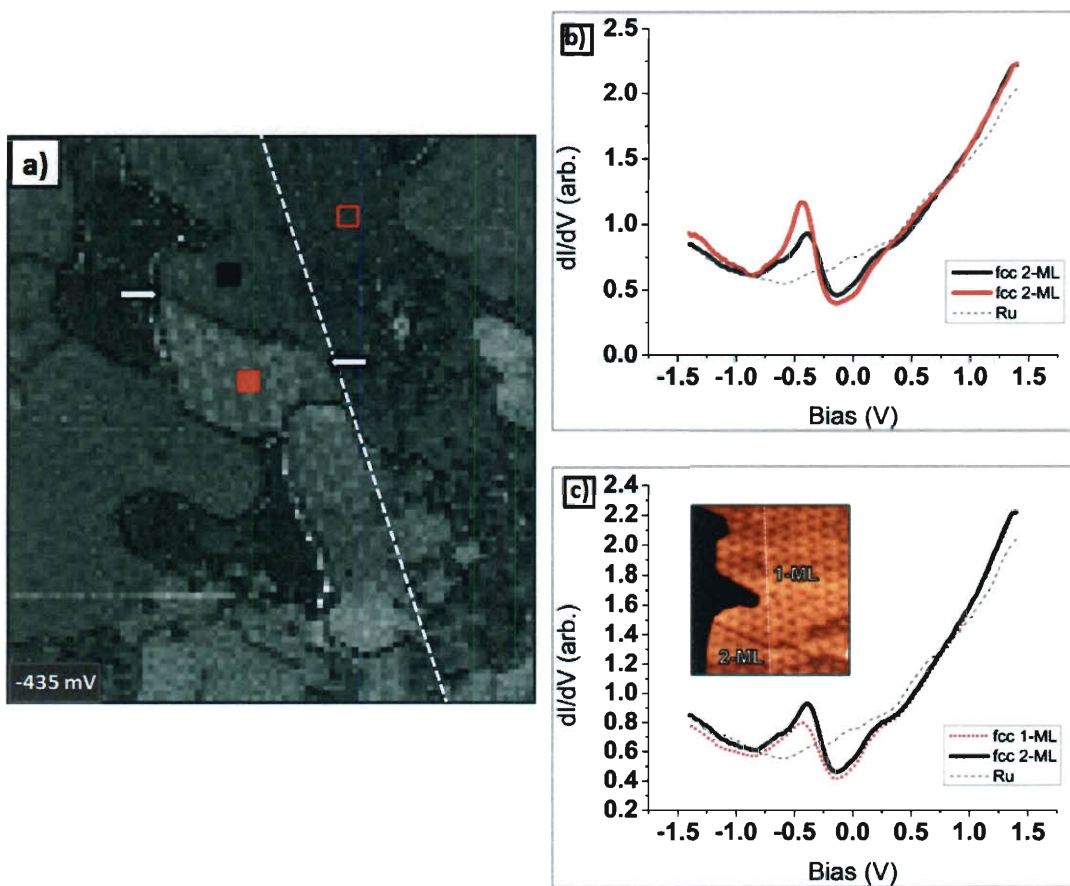


Figure 4.8. (a) Spin-Polarized dI/dV -map of fcc region on Co surface. Dashed lines indicate location of underlying substrate step. Horizontal arrows indicate location of a DL separating two magnetic domain boundaries. Solid red (black) box indicates the 2 ML $fcc_{\uparrow\downarrow}$ ($fcc_{\uparrow\uparrow}$) regions where (b) spatially-averaged dI/dV -curves were taken. Peak intensity from $fcc_{\uparrow\downarrow}$ region (red curve) is higher compared with peak from $fcc_{\uparrow\uparrow}$ region (black curve). Open red box in (a) indicates 1 ML $fcc_{\uparrow\uparrow}$ region where (c) the dI/dV -curve was taken. (inset is STM topograph of region). Peak intensity of 2 ML Co (red curve) is higher compared 1 ML Co (black curve).

Comparing the upper (dark) and lower (bright) contrast regions, it is observed that the peaks from the upper (black curve) and lower (red curve) regions are located at positions -0.389 eV and -0.434 eV below E_F , respectively. The peaks from the upper and lower regions are separated by -44 meV with respect to each other; both the lower (bright) and upper (dark) peaks are shifted -66 meV with respect to the hcp $\uparrow\downarrow$ (bright) and hcp $\uparrow\uparrow$ (dark) dI/dV -peaks shown in figure 4.5. The -66 meV peak shift indicates that these peaks are from regions with fcc stacking and is in good agreement with hcp-to-fcc peak shifts observed by Pietzsch *et al.* (-70 meV) and Wiebe *et al.* (-55 meV). [196,197]

The contrast between the upper and lower fcc-stacked regions is $C = 22\%$, slightly lower, but similar to the contrast observed between the hcp $\uparrow\downarrow$ and hcp $\uparrow\uparrow$ regions. With a peak shift of -43 meV between the upper (dark) and lower (bright) fcc-stacked regions, the source of the contrast across the DL is considered to be magnetic. The characteristic electronic features (upper/lower) described in figure 4.8 indicate that the upper (dark) and lower (bright) regions are fcc $\uparrow\uparrow$ and fcc $\uparrow\downarrow$ regions, respectively.[198,199,200]

The dI/dV -curve (red, dotted) in figure 4.8(c) is taken from the 1 ML Co region to the right of the step. The peak from this 1 ML Co region is located at -0.423 eV below E_F and shifted -32 meV with respect to the 2nd ML Co (fcc $\uparrow\uparrow$) region. The contrast between the 1st and 2nd monolayer Co peaks is $C = 12.5\%$. The electronic properties of the peak from the 1st monolayer Co region also indicate that this is an fcc $\uparrow\uparrow$ region. The contrast difference and peak shift observed across the underlying step are purely related to film thickness in good agreement with Wiebe *et al.*[201]

At the inset of figure 4.9, a dI/dV -spatial map ($V = -0.4$ eV) identifies 2nd and 3rd ML regions on the Co film surface with fcc-stacking. The underlying Ru step runs vertically through the center of the image (dashed-line indicates location). On the left side of the

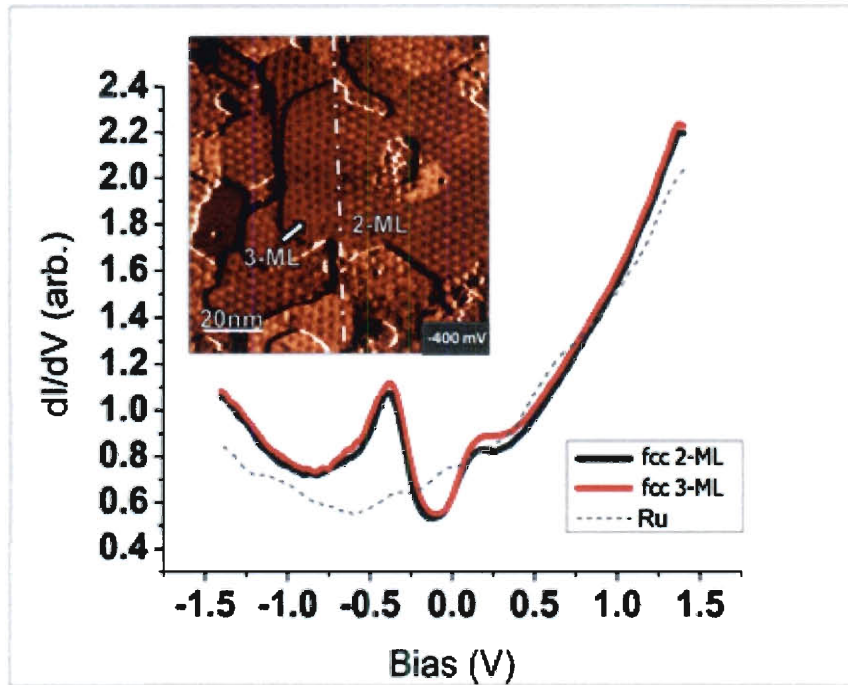


Figure 4.9. Spatially-averaged spin-polarized dI/dV -curves taken from 2,3-ML fcc $\uparrow\uparrow$ regions on Co surface. [inset: dI/dV -map of fcc regions ($V = 0.4$ V); dashed-dot line indicates location of substrate step]. Peak intensity from 3 ML fcc $\uparrow\uparrow$ region (red curve) is higher compared with 2 ML fcc $\uparrow\uparrow$ region (black curve).

step, the Co film is 3 ML; on the right side, the Co film is 2 ML. The dI/dV -curves from each region are also plotted in figure 4.9. Both peaks are located -0.379 eV below E_F ; and the contrast difference across the step (between the 2nd and 3rd monolayer hcp Co peaks) is $C = 1.24\%$, small compared to the contrast observed between the 1st and 2nd fcc Co monolayers. The small contrast observed across the step is purely due to Co film thickness and this region is identified as fcc $\uparrow\uparrow$.

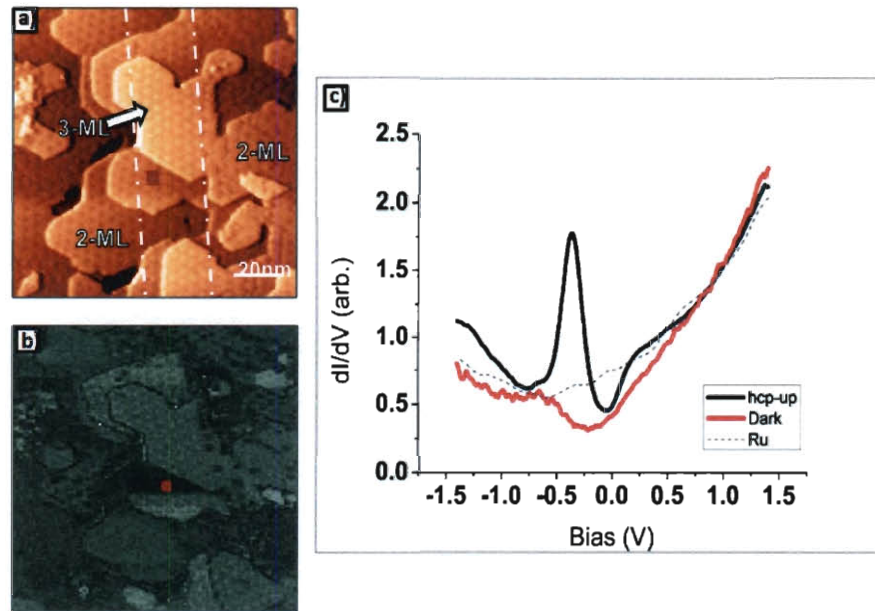


Figure 4.10. (a) STM topograph and (b) corresponding spin-polarized dI/dV -map of a dark contrast, hcp region on the Co surface. Dashed-dot line indicates location of underlying substrate step. Red box in (a) & (b) indicates region where spatially averaged dI/dV -curves were taken. (c) Peak intensity from dark contrast region (red curve) much lower compared with peak from hcp $\uparrow\downarrow$ region (black curve).

Two regions with very dark contrast were identified in the spectral map; one of those regions is shown in figure 4.10. Figure 4.10(a) is a STM topograph taken from this region. The dashed lines in the figure indicate underlying substrate steps. The dark contrast region is shown in the spectral map [figure 4.10(b)] and spans across a step moving from a 2nd to a 3rd ML Co region. The red dot in the figure indicates where a spatially-averaged dI/dV -curve was taken. The curve is plotted in figure 4.10 along with the dI/dV -curve taken from an hcp $\uparrow\downarrow$ (R_1 , shown in figure 4.11) region. Compared with the hcp $\uparrow\downarrow$ (R_1) peak, the peak from the dark (R_1) region is relatively weak and located - 0.653 eV below E_F , shifted -285 meV below the hcp $\uparrow\downarrow$ (bright) peak. The contrast difference between the two regions is $C = 99\%$, indicating minimal electron tunneling

from this region. Although the STM tip is magnetically-coated, the source of the contrast from this region is not magnetic. While the source of the dark contrast is not well-understood in these regions, the dark contrast regions are rare on the film surface and may be caused by local impurities at the surface or surface state quenching caused by adsorbate contamination. Below in figure 4.11 and table 4.1, each of the contrast regions identified using SP-STs are labeled and summarized; all peak heights reported in Table 4.1 have been normalized with respect to the brightest contrast region (peak), R_3 .

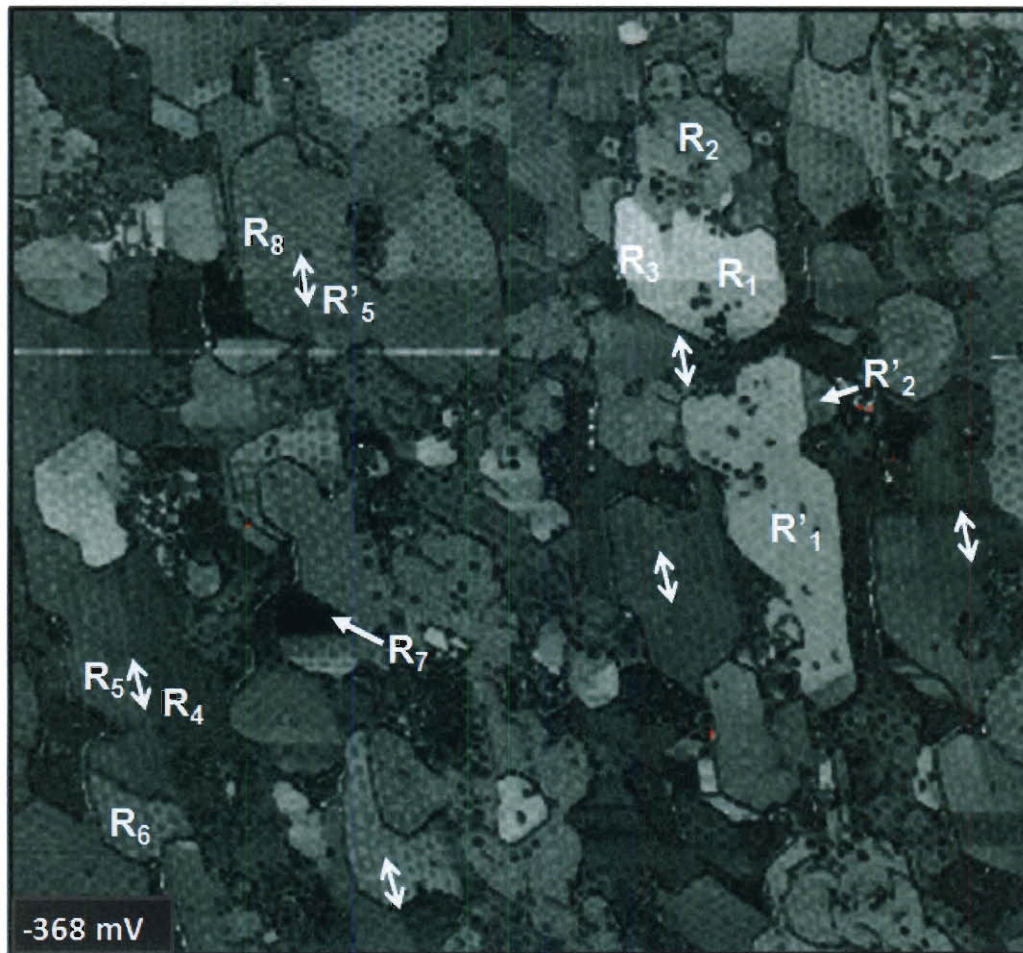


Figure 4.11. 250nm×250nm spin-polarized dI/dV-map of 1.84 ML post-annealed Co(0001) film. Each individual contrast regions (R_i) is identified in table 4.1. Double arrows indicate locations/direction of underlying Ru substrate step.

Table 4.1. Summary of SP- dI/dV Results (Fe-coated tip).^aContrast reported as an absolute value^mCorresponds to magnetic contrast^{*}Corresponds to contrast due to film thickness

Region	Monolayer	Stacking	Spin Moment	Peak Height (arb.)	Peak Pos'n (eV)	Contrast ^a	
R ₁	2-ML	hcp	↑↓	0.940	-0.368	30.0%	R ₁ -R ₂ ^m
R ₂	2-ML	hcp	↑↑	0.695	-0.324	6.2%	R ₃ -R ₁ ^m
R ₃	3-ML	hcp	↑↓	1.000	-0.368		
R' ₁	2-ML	hcp	↑↓	0.805	-0.368	28.7%	R' ₂ -R' ₁ ^m
R' ₂	2-ML	hcp	↑↑	0.603	-0.324		
R ₄	1-ML	fcc	↑↑	0.435	-0.423	12.5%	R ₅ -R ₄ [*]
R ₅	2-ML	fcc	↑↑	0.493	-0.390	22.4%	R ₆ -R ₅ ^m
R ₆	2-ML	fcc	↑↓	0.618	-0.434	99.1%	R ₇ -R ₁ ^m
R ₇	2-ML	--	--	0.317	-0.653		
R' ₅	2-ML	fcc	↑↑	0.569	-0.379	1.2%	R ₈ -R' ₅ [*]
R ₈	3-ML	fcc	↑↑	0.576	-0.379		

4.3.2.2 Spin-Polarized Electronic Structure of Co Films on Ru(0001) Discussion:

It has been shown by El Gabaly and co-workers that ultrathin Co films undergo two different spin re-orientation transitions as the film thickness is increased.[202] Co films >1 ML switch from an in-plane orientation in the 1st ML to a perpendicular orientation in the 2nd ML, back to in-plane in the 3rd ML and at higher coverages, respectively.[203] The spin re-orientation transitions in Co ultrathin films are driven by competition between many physical phenomena: (i) bulk/surface/interfacial anisotropic energies (magnetocrystalline, shape), and also (ii) induced effects caused by the substrate such as hybridization and strain.[204] In this study, only two magnetic domains, one with a parallel spin-moment and one with an anti-parallel spin-moment with respect to the tip, are identified in both the fcc and hcp regions of the Co film surface (refer to table 4.1 and figure 4.11).

However given the fact that the Co (0001) films have a hexagonally closed packed (hcp) crystal structure, six in-plane orientations of Co spin-moment are expected. These moments, \mathbf{M} , should be directed along the six equivalent ($\mathbf{a}_1, \mathbf{a}_2, \mathbf{a}_3, -\mathbf{a}_1, -\mathbf{a}_2, -\mathbf{a}_3$) axes of the Co. As a result, a Fe-coated tip with an in-plane magnetic sensitivity should detect six different magnetic contrast levels in both the fcc and hcp regions of the spin-polarized dI/dV-maps. However as discussed above, only two orientations of the spin-moment are observed at the surface of the surface of the 1.84 ML Co/Ru(0001) films grown here. The presence of only two magnetic contrast levels on the Co(0001) film surface suggests (i) that the spin-moment is not in-plane, but perpendicular at the

surface, and (ii) that the spin-moment of the Fe-coated tip is canted and sensitive to out-of-plane moment alignment at the Co surface. Canted moments of the tip magnetization axis are a common phenomenon in the spin-polarized STM measurements. In general, no spin re-orientations are observed as the local film thickness varies from 1 ML to 3 ML across the film surface, in contrast to the spin-polarized low-energy electron microscopy (SPLEEM) studies of El Gabaly and co-workers who report multiple spin-re-orientations, as described above. Only an out-of-plane magnetic orientation is observed for all three Co monolayers. The differences cited in this study may be directly attributable to the differences in film growth and processing.

For pseudomorphic Co films grown on Ru(0001), an in-plane lattice constant near that of the bulk Co lattice (2.51 Å) is observed by the 2 ML.[205] In this study, the 1.84 ML post-annealed Co films display moiré patterns in both the 2nd and 3rd monolayers with a periodicity of $35 \pm 1 \text{ \AA}$ (calculated from a Fourier transform taken from a moiré pattern on 3rd monolayer Co terrace, shown in figure 4.12). Using the moiré expression for spacing without rotation taken from Parkinson *et al.*, $D = a_1 \cdot a_2 / |a_1 - a_2|$,

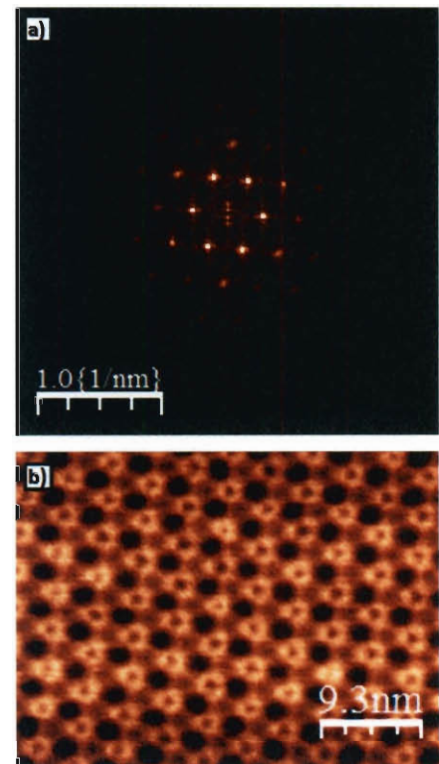


Figure 4.12. (a) Fourier Transform taken from (b) moiré pattern of relaxed 3 ML Co(0001) surface (37nm×28nm). Periodicity of moiré pattern determined to be $35 \pm 1 \text{ \AA}$.

CHAPTER 5

SPIN-AVERAGED & SPIN-POLARIZED STM STUDIES OF MOLECULAR C₆₀ ON Co/Ru(0001)

5.1 Spin-Averaged Intra-Molecular Structure of C₆₀ on Co

An STM topograph of a post-annealed Co film is shown in figure 5.1(a) after 0.02 ML C₆₀ were deposited. The topograph was taken with a W-tip at a bias, $V = 0.950$ V. The C₆₀ was deposited at room temperature. In this region on the Co surface, individual C₆₀ monomers are observed adsorbed predominantly along the bottom step edges of the 1

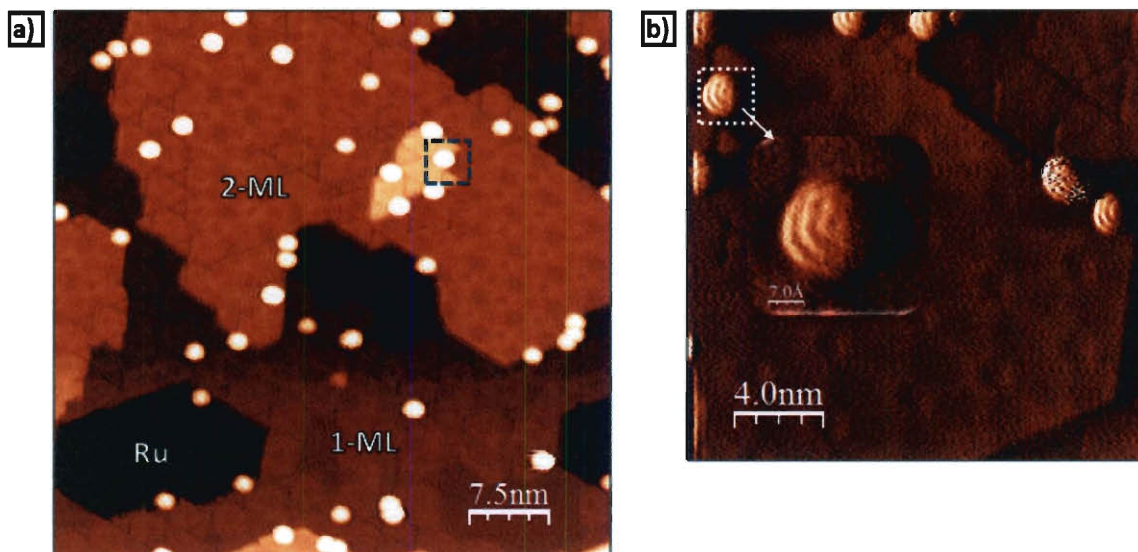


Figure 5.1. (a) STM topograph of 0.02 ML C₆₀ deposited post-annealed Co. Blue box in centered around C₆₀ molecule in (a) indicates same molecule in white box in (b), a high resolution image of C₆₀ (inset). Intramolecular (internal) structure of C₆₀ visible in 4 molecules shown in (b).

and 2nd Co monolayers. Five molecules are also observed adsorbed along the bottom step of a small 3rd monolayer Co island. Individual C₆₀ monomers can be found atop the

where D is the periodic spacing of the moiré pattern, and a_1 and a_2 are the lattice constants of the epitaxial layer and substrate, respectively; the periodicity of the moiré pattern indicates complete relaxation of the Co film (7%).[206] Such a reduction in the strain of post-annealed Co films may influence the relative contribution of shape anisotropy effect at the surface.

4.4 Summary

The spin-polarized electronic structure of bare 1.84 ML Co/Ru(0001) films and 1.84 ML Co/Ru(0001) films with C_{60} adsorbed at the surface was studied using spin-polarized scanning tunneling microscopy and spectroscopy (SP-STM/STS) techniques. On bare Co(0001) films, the spin-polarized STS measurements showed that the dI/dV -peaks taken from fcc-regions were shifted -66 meV lower compared with dI/dV -peaks taken from hcp-regions. The SP-STS measurements also showed the presence of only a perpendicular magnetic spin-orientation on all three Co monolayers at the surface. No evidence of an in-plane magnetic spin-orientation or spin re-orientation transitions were observed at the Co surface. The magnetic domains at the Co surface were affected by presence of defects and dislocation lines, as domain walls showed evidence of pinning at dislocation lines. In addition to the surface state peaks (minority character) observed below Fermi, a surface state peak with majority character was observed above Fermi.

1st and 2nd monolayer terraces of Co; and with the exception of a few regions with moiré patterning, the C₆₀ distribution is fairly uniform across the Co surface. In figure 5.1(b), a higher resolution STM topograph close to the same region is shown. The topograph was obtained with a bias, $V = -0.475$ V. The boxes in figures 5.1(a) and (b) correspond to the same molecule in both topographs. Each C₆₀ molecule in this figure is adsorbed along the bottom step of a 2nd monolayer Co terrace or 3rd monolayer Co island. Four of the seven C₆₀ molecules in figure 5.1(b) display a distinct internal (intra-molecular) structure. The inset in figure 5.1(b) also shows a high resolution image of the C₆₀ molecules internal structure. The spatially-resolved internal structure observed on the C₆₀ molecules is directly related to the spatial charge distribution across the molecule and the molecule's DOS at a given energy within the molecule. The internal structure observed corresponds to 3-fold molecular-orientation of C₆₀; the 3-fold orientation indicates the hexagonal C-ring faces down on the Co(0001) film surface.[207,208,209,210]

5.2 Molecular C₆₀ Spin-Polarized Interactions with Co(0001)

C₆₀ fullerenes in the spin-polarized experimental study were sublimed from a quartz crucible held at 740 K onto a post-annealed Co (0001) film surface held below room temperature in order to limit C₆₀ mobility and cluster size on 2nd and 3rd ML moiré patterned Co terraces. In figure 5.2, an STM topograph shows C₆₀ molecules atop a 2nd ML Co terrace with moiré patterning. At room temperature, the C₆₀ molecules are expected to form large clusters along the edges of this terrace (discussed in Chapter 3).

However in figure 5.2, the C_{60} cluster size on this terrace is limited ranging individual C_{60} monomers up to heptamer-sized clusters. The small cluster size is observed in multiple STM images on both 2nd and 3rd ML moiré patterned Co terraces; and the clusters are randomly distributed and centered atop these terraces away from the step

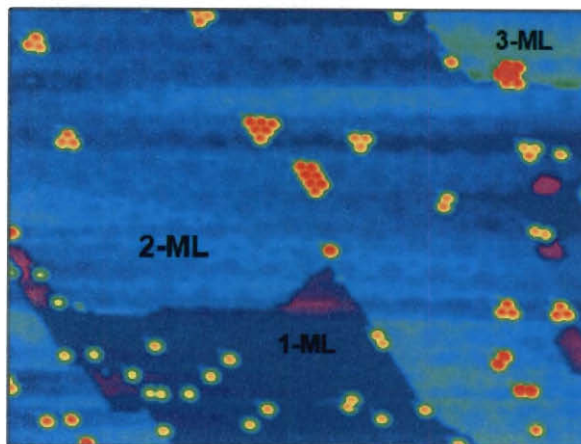


Figure 5.2. (a) STM topograph showing C_{60} clusters centered on 2nd ML Co terrace with moiré pattern. C_{60} deposited onto Co surface below room temperature. Cluster size ranges from individual C_{60} monomers to heptamers.

indicating that the C_{60} cluster size and mobility are limited by the low temperature growth. On the 1st Co ML, only individual monomers and dimers of C_{60} are observed, as the mobility of C_{60} is further impeded in this region by the low temperature of the substrate during deposition and the presence of dislocations at the surface (as described in section 3.3.5 of Chapter 3).

Figure 5.3(a) shows another STM topograph of C_{60} deposited onto a post-annealed Co surface below room temperature. Here, the C_{60} molecules sit atop a 3rd ML moiré patterned Co terrace. The clusters vary in size from individual monomers, adsorbed at the step edge and on the terrace, up to pentamer-sized clusters. In figure 5.3(b), a spin-polarized dI/dV spatial map ($V = -0.4$ eV) is shown of the same area. Both bright (left) and dark (right) regions are present on the 3 ML Co terrace. The red/black squares

indicate regions on the surface where spatially-averaged dI/dV -curves were taken. The dI/dV -curves are plotted in figure 5.3(c). The dI/dV -curve (red) from the bright region has a peak at -0.423 eV below Fermi; the dI/dV -curve (black) from the dark region has a peak at -0.389 eV below Fermi. The peaks from the bright region is shifted -33 meV compared with the peak from the dark region. The contrast difference between the bright/dark region is $C = 25.1\%$. The peaks in figure 5.3(c) are very similar to those discussed above in figure 4.8. By reasoning, the source of the contrast from these two

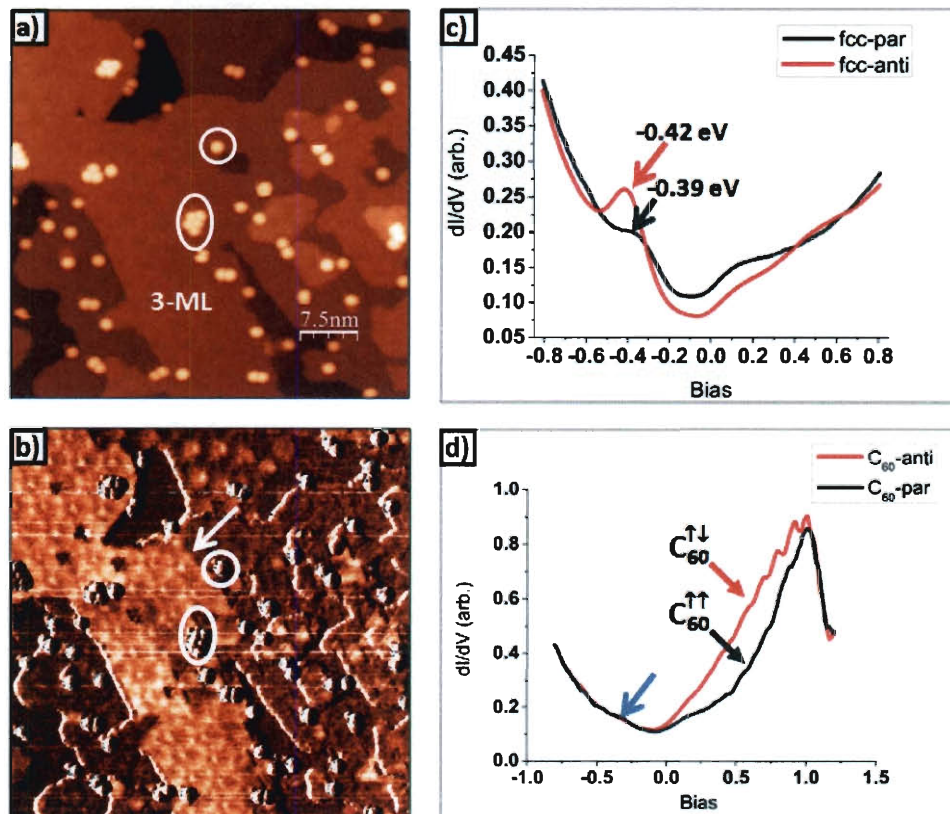


Figure 5.3. (a) STM topograph showing C_{60} atop an 3 ML fcc region on the Co(0001) film surface. (b) Corresponding spin-polarized dI/dV -map of same region on Co surface. Bright (dark) contrast region is anti-parallel (parallel) to tip moment (arrow indicates domain boundary). (c) Spatially averaged dI/dV -curves associate contrast from this region at $fcc_{\uparrow\downarrow}$ (red curve) and $fcc_{\uparrow\uparrow}$ (black curve). Circles in (b) indicate location where (d) spatially averaged dI/dV -curves were taken from C_{60} molecules in the $fcc_{\uparrow\downarrow}$ ($fcc_{\uparrow\uparrow}$), respectively. Blue arrow indicates location of quenched SS peaks.

regions is identified as magnetic and the peaks from the bright (dark) regions are determined to be $\text{fcc}\uparrow\downarrow$ ($\text{fcc}\uparrow\uparrow$). The arrow in figure 5.3(b) indicates the location of the domain wall separating the two regions at the surface.

As shown above in figure 5.3(a) and (b), C_{60} molecules sit atop both the $\text{fcc}\uparrow\downarrow$ and $\text{fcc}\uparrow\uparrow$ regions of the 3rd ML Co region. Spatially-averaged dI/dV -curves were taken from a region directly above a C_{60} monomer sitting atop a $\text{fcc}\uparrow\uparrow$ (dark) domain and from a region directly above a C_{60} cluster sitting atop a $\text{fcc}\uparrow\downarrow$ (bright) domain for comparison. The dI/dV -curves plotted in figure 5.3(d) appear to be tunneling resonance peaks of C_{60} and are located at 0.993 eV above Fermi. The resonance peaks appear in the dI/dV -curves of C_{60} molecules in both $\text{fcc}\uparrow\downarrow$ and $\text{fcc}\uparrow\uparrow$ regions. The resonance peaks observed above C_{60} result from the interaction of the LUMO states with the bulk d-band and surface states near E_F of Co.[211,212]

In figure 5.3(d), a notable absence is observed in the spin-polarized dI/dV -curves taken atop the C_{60} molecules from both ($\text{fcc}\uparrow\downarrow/\text{fcc}\uparrow\uparrow$) regions; the Co surface state peaks are missing. To verify whether the absence of the Co peak is consistent across the surface, line sections were taken from a spectral map from three different C_{60} clusters sitting atop an $\text{fcc}\uparrow\downarrow$ regions. An example line section is shown in figure 5.4. When the tip is over the Co surface the Co surface state peak is present on both sides of the C_{60} cluster.

However when the tip is positioned over the C_{60} cluster, Co surface state peak is absent. Line sections taken from a total ten different C_{60} clusters, sitting atop $fcc\uparrow\downarrow$ and $fcc\uparrow\uparrow$ regions, repeatedly show the absence of the Co surface state peak above C_{60} , shown in Appendix [C].

Locally, the Co surface state peak appears to be quite sensitive to the presence of C_{60} at the surface. However, the absence of this Co peak is relegated only locally to regions on the Co surface where the C_{60} has adsorbed. In a study oxygen adsorption on the Co/W(0001) film surface, Wiebe *et al* report that the Co surface state peak vanishes in regions where oxygen has adsorbed.[213] The quenching of these surface states is observed to be limited to regions where the oxygen was adsorbed. Similar surface state quenching effects have also been observed for CO-adsorption on Cu(111).[214,215]

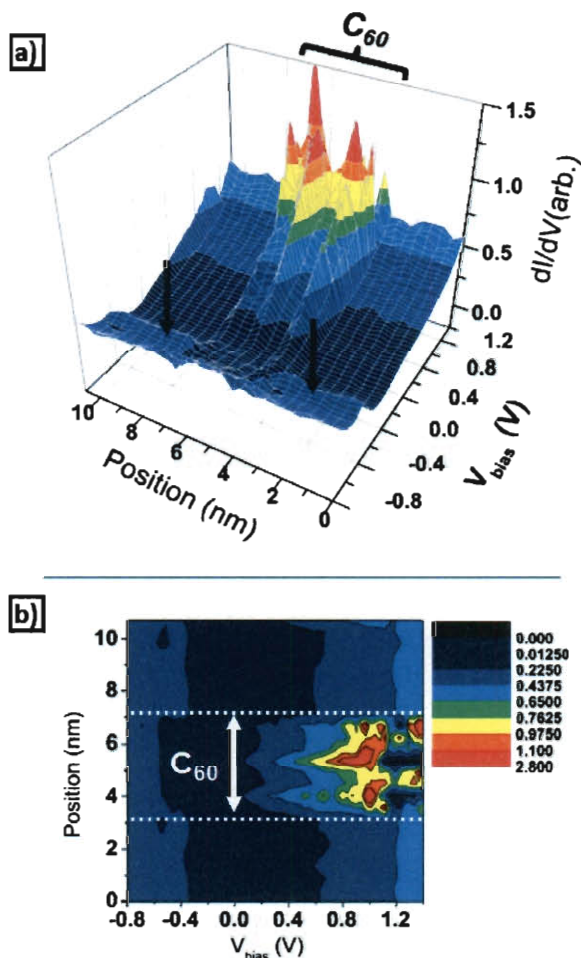


Figure 5.4. (a) Surface plot of dI/dV -curves obtained from a line section taken across C_{60} cluster atop a $fcc\uparrow\downarrow$ region on Co film surface. Arrows indicate location of surface state peaks (-0.42 eV below Fermi) on both sides of C_{60} cluster. (b) Corresponding contour map from (a). Surface state peaks are absent; resonant tunneling peaks observed above C_{60} cluster.

Surface state quenching at the Co surface, however does not automatically imply a reduced or dead Co surface magnetic moment. Numerous studies have investigated the effect of adatom/molecular adsorption at the surface of Co, Fe, and Ni ultra-thin films. Oxygen adsorbed at the surface of Ni(111) has been shown to kill the magnetic moment equivalent of one monolayer at the Ni surface, while oxygen adsorbed at the surface of Fe has been reported to enhance the Fe magnetization.[216,217,218] Amemiya *et al.* report an 18% reduction in the effective spin magnetic moment of Co upon adsorption of oxygen; for CO adsorption, they report the antiferromagnetic alignment of both the CO and the Co atom interacting directly underneath the CO-molecule with the Co film.[219]

The resultant impact of C₆₀ on the Co magnetic moment at the surface cannot be deciphered from these measurements. X-ray magnetic circular dichroism (XMCD) and photoemission studies are needed to determine the effect of C₆₀ on the Co moment. However upon adsorption of the C₆₀, the most important contributions to the resultant moment are (i) the degree to which the C₆₀ molecular orbitals hybridize with the 3d bands of neighboring Co atoms at the surface and (ii) the local charge depletion (quenching) of the partially occupied Co surface states, as charge depletion has been shown to reduce exchange-splitting of surface states.[220] Preliminary results from XAS measurements indicate some charge is transferred to the C₆₀ adsorbed on the Co(0001) film surface {Appendix [C]}.[221]

To demonstrate how the magnetic (spin-polarized) contrast across the Co(0001) film surface depends on voltage, spatially-resolved spin-polarized conductance maps taken at different voltages (shown in figure 5.5) are presented below. Figure 5.6 shows a 100nm×100nm STM topograph of the same fcc $\uparrow\downarrow$ ($\uparrow\uparrow$) region shown in figure 5.3 along with corresponding spatially-resolved spectral maps at different voltages above and below Fermi. For a $V_{\text{bias}} = 1.093$ V above Fermi near the C_{60} resonant tunneling peak [figure 5.6(b)], the C_{60}

molecules in dI/dV -map show a bright contrast. As the bias is decreased to $V_{\text{bias}} = 379$ mV, the brightness of the C_{60} molecules in the dI/dV -map decreases; and very little or no spin-polarized contrast is observed on the Co film surface, itself, at this voltage

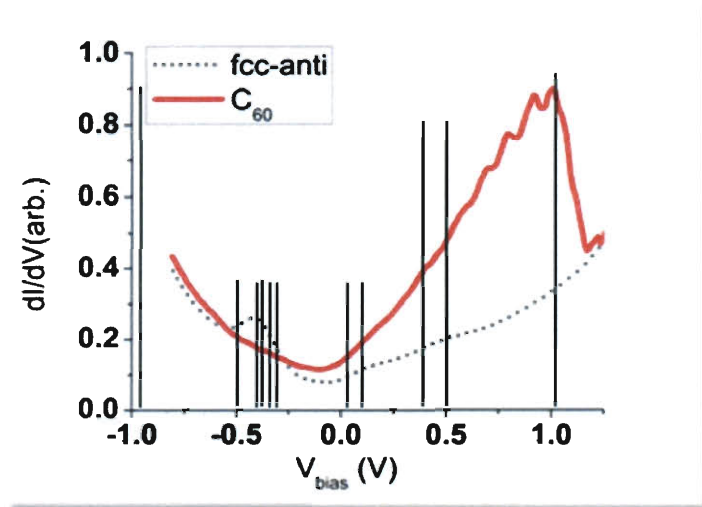


Figure 5.5 Spin-polarized conductance (dI/dV) curves taken from fcc $\uparrow\downarrow$ region (black-dotted) and above C_{60} cluster (red), respectively. The eleven black bars in the plot represent voltage of each SP-STIS image, shown in figure 5.6 (below). Refer to text for more information.

bias. At $V_{\text{bias}} = 148$ mV above Fermi [figure 5.6(e)], the contrast between the fcc $\uparrow\downarrow$ and fcc $\uparrow\uparrow$ regions increases. However, the contrast in the fcc $\uparrow\downarrow$ (dark) and fcc $\uparrow\uparrow$ (bright) regions is observed to be the opposite of the contrast expected in these two regions (please reference Table 4.1). The change in the contrast observed is related to the majority character of the Co surface state approximately 0.1 eV above Fermi. As the

bias voltage is decreased below Fermi, contrast in the dI/dV -map between the $fcc_{\uparrow\downarrow}$ and

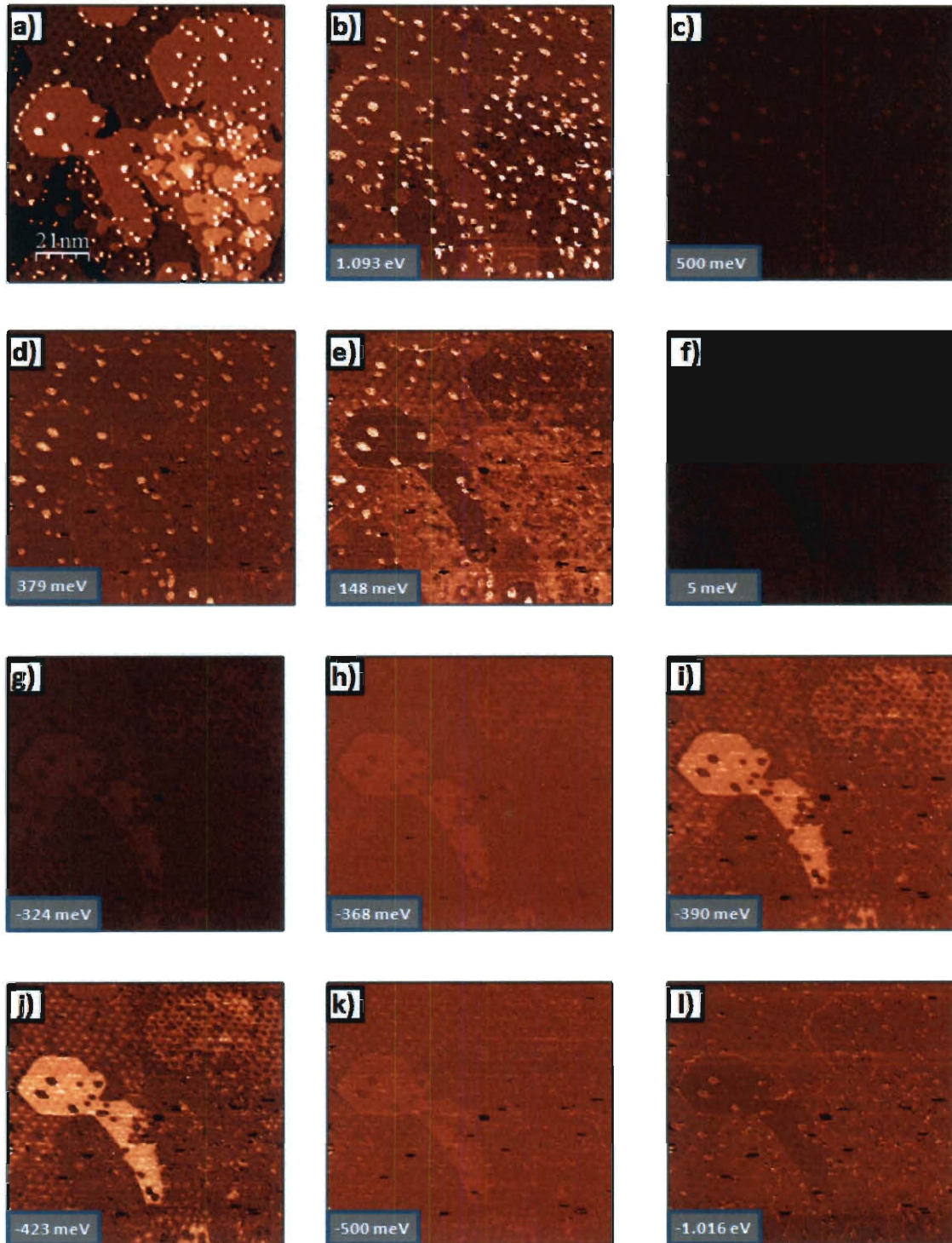


Figure 5.6. (a) STM topograph of C_{60} atop $fcc_{\uparrow\downarrow}$ and $fcc_{\uparrow\uparrow}$ regions on the $Co(0001)$ film surface along with (b-l) corresponding spin-polarized spectral-map of same region at different voltages above and below Fermi.

$f_{cc\uparrow}$ regions is lost again and begins to increase at a voltage bias, $V_{\text{bias}} = -368$ mV below Fermi [figure 5.6(h)]. Contrast between the regions reaches a maximum at a $V_{\text{bias}} = -423$ mV, near the peak of the $f_{cc\uparrow\downarrow}$ region [figure 5.6(j)]. At lower bias voltages little contrast is observed in the dI/dV -maps.

5.3 Summary

C_{60} molecules deposited onto the substrate surface below room temperature showed a tendency to form smaller clusters on the Co film surface compared with sub-ML C_{60} deposited at room temperature. At the Co surface, an internal structure of C_{60} is observed corresponding to a 3-fold (symmetry) molecular-orientation. SP-STM/STS measurements did not reveal any affect of C_{60} on local magnetic properties at the Co surface. However in the near-region where C_{60} clusters were adsorbed, the absence of the Co surface state peak indicated that the state was quenched or depopulated by presence of C_{60} . The Co electronic structure is locally perturbed by presence C_{60} , a large molecular impurity, at the surface.

CHAPTER 6: CONCLUSIONS

The bulk magnetic properties of composite C_{60} -ferromagnetic metal thin film systems and the functionality of C_{60} -based molecular transistor junction devices are fundamentally dependant on the atomic structure and electronic interactions at the C_{60} fullerene-metal interface. In this dissertation, the atomic-molecular and electronic interactions of C_{60} at the surface of Ni(100) and Co(0001) films were determined using in-situ spin-averaged and spin-polarized STM measurement techniques.

C_{60} molecules deposited onto the Ni(100) film surface were observed to be fairly immobile. However, a uniform distribution of C_{60} molecules was observed across the Ni(100) film surface. On atomically-flat Ni(100) films pre-covered with C_{60} , homoepitaxial Ni film growth studies revealed no obvious of effects by the presence of C_{60} at the surface. Crystalline growth continued uninterrupted, as a high Ni diffusion barrier along with low C_{60} mobility worked to limit the occurrence of Ni- C_{60} collisions at the surface. Auger electron spectroscopy (AES) results helped to confirm that C_{60} molecules maintained their chemical integrity (or do not decompose) during Ni growth.

The mobility of C_{60} molecules deposited on the Co(0001) film surface was observed to vary from region to region: in some regions on the Co surface, the C_{60} molecules showed high mobility, however in other regions; C_{60} mobility was severely limited. The result was a non-uniform distribution of C_{60} molecules across the Co film surface. The

variations observed in C_{60} mobility were driven by local changes in the Co film's atomic surface structure – (i) moiré reconstructions and (ii) surface dislocations.

On atomically-flat Co(0001) films pre-covered with C_{60} , homoepitaxial growth studies showed that Co islands only nucleated and grew from the step edges and locally around C_{60} molecules. The C_{60} molecules served as pseudo-nucleation sites for Co-island growth and indicated that the strength of the Co- C_{60} bond interaction is stronger than the Co-Co bond on the film's terrace. Crystalline growth of the Co films continued uninterrupted, similar to the Ni(100) films. Well-defined moiré reconstructed terraces were easily observed.

The findings above demonstrate that the nature of the C_{60} -metallic bond at the surface can influence film growth and morphology. As a result, C_{60} -metal thin film systems (i.e., Ni- C_{60} , Co- C_{60}) will likely exhibit different initial growth modes and morphologies dependent upon (i) the substrate surface, (ii) the initial growth conditions, and (iii) the interactions of the C_{60} molecule with the metal film overlayer and substrate.

Results from spin-polarized scanning tunneling microscopy and spectroscopy (SP-STM/STS) studies show that the spin-polarized electronic structure of the Co(0001) film surface is fairly complex, influenced by a number of factors: (i) sequential layer stacking (fcc/hcp), (ii) strain-induced reconstruction (moiré), (iii) Co(0001) atomic layer thickness, and (iv) surface defects. On bare Co(0001) films, STS measurements showed

that the spin-polarized dI/dV -peaks taken from the $\text{fcc}\uparrow\uparrow$ and $\text{fcc}\uparrow\downarrow$ domain regions were shifted -66 meV lower and had lower peak intensities (contrast) as compared with the spin-polarized dI/dV -peaks taken from the $\text{hcp}\uparrow\uparrow$ and $\text{hcp}\uparrow\downarrow$ domain regions.

SP-STs measurements only detected a perpendicular magnetic spin-orientation in each of the three Co monolayers at the surface. No evidence of an in-plane magnetic spin orientation was observed at the Co surface; and no evidence of spin re-orientation transitions were observed. Magnetic domains on the Co surface were also affected by presence of defects and dislocation lines, as domain walls showed evidence of pinning at dislocation lines. In addition to the surface state peaks (minority character) observed below Fermi, an additional surface state peak with majority character was observed above Fermi.

C_{60} molecules deposited at substrate temperatures below room temperature formed small clusters at the center of Co film terraces. With C_{60} molecules adsorbed on the Co(0001) surface, an internal structure of C_{60} was observed corresponding to a 3-fold (symmetry) molecular-orientation. SP-STM/STS measurements did not reveal any effect of C_{60} on the Co film's surface magnetic properties. However in the near-region where C_{60} clusters were adsorbed, Co surface state peaks were absent, indicating that the surface states could be quenched by presence of C_{60} . These results suggest the local electronic structure of Co(0001) is perturbed by the presence of C_{60} at the surface.

The complex atomic, electronic, and magnetic environment posed by Co film surfaces make it an interesting system for future C₆₀ (ad-molecular) studies. Theoretical studies have shown that in presence of an external H-field, paramagnetic and diamagnetic ring currents develop on the C₆₀ molecule surface.[222] Inelastic neutron scattering experiments have also shown that the molecular rotations of bulk C₆₀ (fcc) crystals are slowed in the presence of small H-fields.[223] Interesting SP-STM studies might investigate how different ferromagnetic domains and/or H-fields (magnitude and direction) may affect C₆₀ inter-molecular interactions and orientations at the surface.

Determining how C₆₀ molecules respond in external H-fields can increase our understanding C₆₀-based ferromagnetic molecular junction transistors (MTJ) and may provide a pathway for manipulating the molecular orientation of C₆₀ on metallic surfaces. Future spin-averaged and spin-polarized STM/STS studies may also reveal the perturbation effects of C₆₀ at metal surfaces. Fano oscillations and spin-polarized electron scattering effects may persist at the metallic surface in the presence of C₆₀. [224,225,226] X-ray Magnetic Circular Dichroism (XMCD) studies could also be used to determine how C₆₀ adsorption effects magnetism at the surface of ferromagnetic thin film systems, as well. Each of these studies would play an important role in helping clarify how ferromagnetic metal surfaces interact with large molecules.

¹ Yukitaka Matsuoka et al., "Transport properties of C₆₀ thin film FETs with a channel of several-hundred nanometers," *Science and Technology of Advanced Materials* 6, no. 5 (7, 2005): 427-430.

² Kazuhito Tsukagoshi, Bruce W. Alphenaar, and Hiroki Ago, "Coherent transport of electron spin in a ferromagnetically contacted carbon nanotube," *Nature* 401, no. 6753 (October 7, 1999): 572-574.

³ Francois Leonard and J. Tersoff, "Role of Fermi-Level Pinning in Nanotube Schottky Diodes," *Physical Review Letters* 84, no. 20 (May 15, 2000): 4693.

-
- ⁴ Eldon G. Emberly and George Kirczenow, "Molecular spintronics: spin-dependent electron transport in molecular wires," *Chemical Physics* 281, no. 2-3 (August 1, 2002): 311-324.
- ⁵ S. Heinze et al., "Carbon Nanotubes as Schottky Barrier Transistors," *Physical Review Letters* 89, no. 10 (2002): 106801.
- ⁶ "Information for the Public, The Nobel Prize in Physics 2007," *The Royal Swedish Academy of Sciences*, http://nobelprize.org/nobel_prizes/physics/laureates/2007/info.html.
- ⁷ "The Discovery of Giant Magnetoresistance, Scientific Background on the Nobel Prize in Physics 2007," *The Royal Swedish Academy of Sciences*, http://nobelprize.org/nobel_prizes/physics/laureates/2007/phyadv07.pdf.
- ⁸ Evgeny Y Tsymlal et al., "Interface effects in spin-dependent tunneling," *Progress in Materials Science* 52 (February 1, 2007): 401-420.
- ⁹ Christian Heiliger, Peter Zahn, and Ingrid Mertig, "Microscopic origin of magnetoresistance," *Materials Today* 9, no. 11 (November 2006): 46-54.
- ¹⁰ X.-G. Zhang, W. H. Butler, and Amrit Bandyopadhyay, "Effects of the iron-oxide layer in Fe-FeO-MgO-Fe tunneling junctions," *Physical Review B* 68, no. 9 (2003): 092402.
- ¹¹ S Yuasa and D D Djayaprawira, "Giant tunnel magnetoresistance in magnetic tunnel junctions with a crystalline MgO(001) barrier," *Journal of Physics D: Applied Physics* 40, no. 21 (11, 2007): R337-R354.
- ¹² M. Bibes and A. Barthelemy, "Oxide Spintronics," *IEEE Transactions on Electron Devices* 54, no. 5 (May 2007): 1003-1023.
- ¹³ Abhay N. Pasupathy et al., "The Kondo Effect in the Presence of Ferromagnetism," *Science* 306, no. 5693 (October 1, 2004): 86-89.
- ¹⁴ Kenneth E. Johnson, "Magnetic materials and structures for thin-film recording media (invited)," *Journal of Applied Physics* 87, no. 9 (2000): 5365.
- ¹⁵ Bin Lu et al., "Development of Co-Alloys for Perpendicular Magnetic Recording Media," *IEEE Transactions on Magnetics* 39, no. 4 (July 2003): 1908-1913.
- ¹⁶ Olav Hellwig et al., "Role of boron on grain sizes and magnetic correlation lengths in recording media as determined by soft x-ray scattering," *Applied Physics Letters* 80, no. 7 (2002): 1234.
- ¹⁷ Xiaobin Wang and H. Neal Bertram, "Simple transition parameter expression including grain size and intergranular exchange," *Journal of Applied Physics* 93, no. 10 (2003): 7005.
- ¹⁸ X. Z. Cheng and M. B. A. Jalil, "Micromagnetic study of intergranular exchange coupling in tilted perpendicular media," *IEEE Transactions on Magnetics* 41, no. 10 (October 2005): 3115-3117.
- ¹⁹ Hong Zhou, H. N. Bertram, and M. E. Schabes, "Micromagnetic analysis of the effect of intergranular exchange on thermal stability in magnetic recording. III. Perpendicular media," *IEEE Transactions on Magnetics* 32, no. 2 (March 2002): 1422-1428.
- ²⁰ Lingyi A. Zheng, Enrique V. Barrera, and Robert D. Shull, "Magnetic properties of the Co-C60 and Fe-C60 nanocrystalline magnetic thin films," *Journal of Applied Physics* 97, no. 9 (2005): 094309.
- ²¹ Lingyi A. Zheng et al., "Formation of nanomagnetic thin films by dispersed fullerenes," *Applied Physics Letters* 77, no. 20 (2000): 3242.
- ²² Lingyi A. Zheng, Enrique V. Barrera, and Robert D. Shull, "Formation and stabilization of nanosize grains in ferromagnetic thin films by dispersed C60," *Journal of Applied Physics* 92, no. 1 (2002): 523.
- ²³ Kenta Amemiya et al., "O K-edge x-ray magnetic circular dichroism of atomic O adsorbed on an ultrathin Co/Cu(100) film: Comparison with molecular CO on Co/Cu(100)," *Physical Review B* 64, no. 13 (2001): 132405.
- ²⁴ Yoshiki Yonamoto et al., "Magnetic Interaction between Adsorbed NO and fcc Co(001) Thin Films Studied by X-ray Magnetic Circular Dichroism," *Journal of the Physical Society of Japan* 71 (2002): 607-612.
- ²⁵ K. von Bergmann et al., "Spin-Polarized Electron Scattering at Single Oxygen Adsorbates on a Magnetic Surface," *Physical Review Letters* 92, no. 4 (January 27, 2004): 046801.
- ²⁶ G. Srajer et al., "Advances in nanomagnetism via X-ray techniques," *Journal of Magnetism and Magnetic Materials* 307, no. 1 (December 2006): 1-31.
- ²⁷ "<https://share.sandia.gov/8700/capabilities/content.php?cid=213>," *Scanning Tunneling Microscopy*, 2007.

-
- ²⁸ Ben Streetman, *Solid State Electronic Devices*, 3rd ed. (Englewood Cliffs, New Jersey: Prentice Hall, 1990).
- ²⁹ J. Bardeen, "Tunnelling from a Many-Particle Point of View," *Physical Review Letters* 6, no. 2 (January 15, 1961): 57.
- ³⁰ J. Tersoff and D. R. Hamann, "Theory of the scanning tunneling microscope," *Physical Review B* 31, no. 2 (January 15, 1985): 805.
- ³¹ D. Wortmann, H. Ishida, and S. Blugel, "Embedded Green-function formulation of tunneling conductance: Bardeen versus Landauer approaches," *Physical Review B* 72, no. 23 (December 15, 2005): 235113.
- ³² Bardeen, "Tunnelling from a Many-Particle Point of View." *Physical Review Letters* 6, no. 2 (January 15, 1961): 57.
- ³³ B. G. Briner et al., "Charge-density oscillations on Be(1010): Screening in a non-free two-dimensional electron gas," *Physical Review B* 58, no. 20 (November 15, 1998): 13931.
- ³⁴ J. Wang, M. Li, and E. I. Altman, "Scanning tunneling microscopy study of Pd growth on Ge(001)," *Journal of Applied Physics* 100, no. 11 (2006): 113501.
- ³⁵ F. Nouvertne et al., "Atomic exchange processes and bimodal initial growth of Co/Cu(001)," *Physical Review B* 60, no. 20 (November 15, 1999): 14382.
- ³⁶ D. Drakova, M. Nedjalkova, and G. Doyen, "Theory of tip-dependent imaging of adsorbates in the STM: CO on Cu(111)," *International Journal of Quantum Chemistry* 106, no. 6 (2006): 1419-1431.
- ³⁷ D. Wortmann et al., "Resolving Complex Atomic-Scale Spin Structures by Spin-Polarized Scanning Tunneling Microscopy," *Physical Review Letters* 86, no. 18 (April 30, 2001): 4132.
- ³⁸ D. Wortmann, H. Ishida, and S. Blugel, "Embedded Green-function formulation of tunneling conductance: Bardeen versus Landauer approaches," *Physical Review B* 72, no. 23 (December 15, 2005): 235113.
- ³⁹ Ivar Giaever and Karl Megerle, "Study of Superconductors by Electron Tunneling," *Physical Review* 122, no. 4 (May 15, 1961): 1101.
- ⁴⁰ P. M. Tedrow and R. Meservey, "Spin Polarization of Electrons Tunneling from Films of Fe, Co, Ni, and Gd," *Physical Review B* 7, no. 1 (January 1, 1973): 318.
- ⁴¹ R Meservey, "Spin-polarized electron tunneling," *Physics Reports* 238, no. 4 (3, 1994): 173-243.
- ⁴² D. Wortmann et al., "Resolving Complex Atomic-Scale Spin Structures by Spin-Polarized Scanning Tunneling Microscopy," *Physical Review Letters* 86, no. 18 (April 30, 2001): 4132.
- ⁴³ M Bode, "Spin-polarized scanning tunnelling microscopy," *Reports on Progress in Physics* 66, no. 4 (4, 2003): 523-582.
- ⁴⁴ J. A. C. Bland and Bretislav Heinrich, *Ultrathin Magnetic Structures III: Fundamentals of Nanomagnetism* (Springer, 2005).
- ⁴⁵ Q. Y. Jin et al., "Periodic Oscillations of the Surface Magnetization during the Growth of Co Films on Cu(001)," *Physical Review Letters* 80, no. 18 (May 4, 1998): 4056.
- ⁴⁶ Jürgen K. Kübler, *Theory of itinerant electron magnetism* (Oxford University Press, 2000).
- ⁴⁷ J. A. C. Bland and Bretislav Heinrich, *Ultrathin Magnetic Structures III: Fundamentals of Nanomagnetism* (Springer, 2005).
- ⁴⁸ M. Tischer et al., "Enhancement of Orbital Magnetism at Surfaces: Co on Cu(100)," *Physical Review Letters* 75, no. 8 (1995): 1602.
- ⁴⁹ Q. Y. Jin et al., "Periodic Oscillations of the Surface Magnetization during the Growth of Co Films on Cu(001)," *Physical Review Letters* 80, no. 18 (May 4, 1998): 4056.
- ⁵⁰ N Memmel, "Monitoring and modifying properties of metal surfaces by electronic surface states," *Surface Science Reports* 32, no. 3-4 (1998): 91-163.
- ⁵¹ Hartmut Zabel, "Magnetism of chromium at surfaces, at interfaces and in thin films," *Journal of Physics: Condensed Matter* 11, no. 48 (1999): 93039346.
- ⁵² Charles Kittel, "Physical Theory of Ferromagnetic Domains," *Reviews of Modern Physics* 21, no. 4 (October 1, 1949): 541.

-
- ⁵³ S. L. Silva et al., "Fabricating nanometer-scale Co dot and line arrays on Cu(100) surfaces," *Applied Physics Letters* 76, no. 9 (2000): 1128.
- ⁵⁴ J R Cerda et al., "Epitaxial growth of cobalt films on Cu(100): a crystallographic LEED determination," *Journal of Physics: Condensed Matter* 5, no. 14 (1993): 2055.
- ⁵⁵ W. Weber et al., "Magnetic switching in cobalt films by adsorption of copper," *Nature* 374, no. 6525 (April 27, 1995): 788-790.
- ⁵⁶ W. Weber et al., "Structural relaxation and magnetic anisotropy in Co/Cu(001) films," *Physical Review B* 54, no. 6 (1996): 4075.
- ⁵⁷ R. Moroni et al., "Uniaxial Magnetic Anisotropy in Nanostructured Co/Cu(001): From Surface Ripples to Nanowires," *Physical Review Letters* 91, no. 16 (October 17, 2003): 167207.
- ⁵⁸ Fumihiko Matsui et al., "Atomic-Layer Resolved Magnetic and Electronic Structure Analysis of Ni Thin Film on a Cu(001) Surface by Diffraction Spectroscopy," *Physical Review Letters* 100, no. 20 (May 19, 2008): 207201.
- ⁵⁹ A. B. Shick, Yu. N. Gornostyrev, and A. J. Freeman, "Magnetoelastic mechanism of spin-reorientation transitions at step edges," *Physical Review B* 60, no. 5 (1999): 3029.
- ⁶⁰ U. Bauer et al., "Effect of step decoration on the spin reorientation of Ni films grown on vicinal Cu(001)," *Physical Review B* 76, no. 18 (November 14, 2007): 184415.
- ⁶¹ Farid El Gabaly et al., "Imaging Spin-Reorientation Transitions in Consecutive Atomic Co Layers on Ru(0001)," *Physical Review Letters* 96, no. 14 (April 11, 2006): 147202.
- ⁶² Farid El Gabaly et al., "Noble metal capping effects on the spin-reorientation transitions of Co/Ru(0001)," *New Journal of Physics* 10, no. 7 (7, 2008): 073024.
- ⁶³ Farid El Gabaly et al., "Imaging Spin-Reorientation Transitions in Consecutive Atomic Co Layers on Ru(0001)," *Physical Review Letters* 96, no. 14 (April 11, 2006): 147202.
- ⁶⁴ C. Liu and S.D. Bader, "Magnetism and growth of ultrathin Co films grown epitaxially on Ru(0001)," *Journal of Magnetism and Magnetic Materials* 119, no. 1-2 (February 1, 1993): 81-86.
- ⁶⁵ K. Baberschke, M. Donath, and W. Nolting, *Band-Ferromagnetism*, 1st ed. (Springer, 2001).
- ⁶⁶ N Memmel, "Monitoring and modifying properties of metal surfaces by electronic surface states," *Surface Science Reports* 32, no. 3-4 (1998): 91-163.
- ⁶⁷ Andrew Zangwill, *Physics at Surfaces* (Cambridge University Press, 1988).
- ⁶⁸ Charles Kittel, *Introduction to Solid State Physics*, 7th ed. (Wiley, 1995).
- ⁶⁹ Neil W. Ashcroft and N. David Mermin, *Solid State Physics*, 1st ed. (Brooks Cole, 1976).
- ⁷⁰ N Memmel, "Monitoring and modifying properties of metal surfaces by electronic surface states," *Surface Science Reports* 32, no. 3-4 (1998): 91-163.
- ⁷¹ Jürgen K. Kübler, *Theory of itinerant electron magnetism* (Oxford University Press, 2000).
- ⁷² Markus Donath, "Surface Electronic Structure of Band Ferromagnets," in *Band-Ferromagnetism*, 2001, 267-282, http://dx.doi.org/10.1007/3-540-44610-9_17.
- ⁷³ S.H. Ma et al., "Effect of S adsorption on magnetic Co(0001) surface: a DFT study," *The European Physical Journal B* 61, no. 3 (2008): 6.
- ⁷⁴ Jürgen K. Kübler, *Theory of itinerant electron magnetism* (Oxford University Press, 2000).
- ⁷⁵ F. J. Himpsel and D. E. Eastman, "Intrinsic Lambda 1-symmetry surface state on Co(0001)," *Physical Review B* 20, no. 8 (October 15, 1979): 3217.
- ⁷⁶ T. Kishi et al., "Spin-dependent electronic structure and theoretical SP-STM images for Co(0001) film," *IEEE Transactions on Magnetics* 36, no. 5 (September 2000): 2972-2974.
- ⁷⁷ L. Diekhoner et al., "Surface States of Cobalt Nanoislands on Cu(111)," *Physical Review Letters* 90, no. 23 (June 10, 2003): 236801.
- ⁷⁸ O. Pietzsch et al., "Spin-Polarized Scanning Tunneling Spectroscopy of Nanoscale Cobalt Islands on Cu(111)," *Physical Review Letters* 92, no. 5 (February 6, 2004): 057202.
- ⁷⁹ S. N. Okuno, T. Kishi, and K. Tanaka, "Spin-Polarized Tunneling Spectroscopy of Co(0001) Surface States," *Physical Review Letters* 88, no. 6 (January 25, 2002): 066803.
- ⁸⁰ Lam H. Yu and Douglas Natelson, "The Kondo Effect in C60 Single-Molecule Transistors," *Nano Letters* 4, no. 1 (January 1, 2004): 79-83.

-
- ⁸¹ Lingyi A. Zheng, Enrique V. Barrera, and Robert D. Shull, "Formation and stabilization of nanosize grains in ferromagnetic thin films by dispersed C60," *Journal of Applied Physics* 92, no. 1 (2002): 523.
- ⁸² J. Ortiz-Lopez and R. Gomez-Aguilar, "Dielectric permittivity and AC conductivity in polycrystalline and amorphous C60," *Revista mexicana de física* 49, no. 6 (2003): 529-536.
- ⁸³ Jin Yu, Rajiv K. Kalia, and Priya Vashishta, "Phonon dispersion and density of states of solid C60," *Applied Physics Letters* 63, no. 23 (1993): 3152.
- ⁸⁴ Y. Z. Li et al., "Order and Disorder in C60 and KxC60 Multilayers: Direct Imaging with Scanning Tunneling Microscopy," *Science* 253, no. 5018 (July 12, 1991): 429-433.
- ⁸⁵ C. W. Chang et al., "Probing structural phase transitions of crystalline C60 via resistivity measurements of metal film overlayers," *Solid State Communications* 128, no. 9-10 (December 2003): 359-363.
- ⁸⁶ Yukiumi Kita et al., "Study on the intermolecular interaction of C60 and simulations on the orientational properties of C60 in crystals," *The Journal of Chemical Physics* 125, no. 3 (2006): 034506.
- ⁸⁷ M. R. C. Hunt et al., "Charge transfer and structure in C60 adsorption on metal surfaces," *Physical Review B* 51, no. 15 (April 15, 1995): 10039.
- ⁸⁸ Milton Ohring, *Materials Science of Thin Films, Second Edition*, 2nd ed. (Academic Press, 2001).
- ⁸⁹ N Memmel, "Monitoring and modifying properties of metal surfaces by electronic surface states," *Surface Science Reports* 32, no. 3-4 (1998): 91-163.
- ⁹⁰ Roald Hoffmann, "A chemical and theoretical way to look at bonding on surfaces," *Reviews of Modern Physics* 60, no. 3 (July 1, 1988): 601.
- ⁹¹ Susumu Saito, Koichiro Umemoto, and Takashi Miyake, *Structure & Bonding*, vol. 109 (Springer Berlin / Heidelberg, 2004).
- ⁹² Philippe Sautet, "Images of Adsorbates with the Scanning Tunneling Microscope: Theoretical Approaches to the Contrast Mechanism," *Chemical Reviews* 97, no. 4 (June 1, 1997): 1097-1116.
- ⁹³ B. Hammer and J. K. Norskov, "Why gold is the noblest of all the metals," *Nature* 376, no. 6537 (July 20, 1995): 238-240.
- ⁹⁴ Manabu Kiguchi et al., "Atomic and electronic structures of heteroepitaxial C60 film grown on Ni(1 1 1), Cu(1 1 1)," *Applied Surface Science* 212-213 (May 15, 2003): 101-104.
- ⁹⁵ P. W. Murray et al., "Growth of C60 on Cu(110) and Ni(110) surfaces: C60-induced interfacial roughening," *Physical Review B* 55, no. 15 (April 15, 1997): 9360.
- ⁹⁶ A. Ruban et al., "Surface electronic structure and reactivity of transition and noble metals," *Journal of Molecular Catalysis A: Chemical* 115, no. 3 (February 7, 1997): 421-429.
- ⁹⁷ M. R. C. Hunt et al., "Charge transfer and structure in C60 adsorption on metal surfaces," *Physical Review B* 51, no. 15 (April 15, 1995): 10039.
- ⁹⁸ P. W. Murray et al., "Growth of C60 on Cu(110) and Ni(110) surfaces: C60-induced interfacial roughening," *Physical Review B* 55, no. 15 (April 15, 1997): 9360.
- ⁹⁹ J. Weckesser, J. V. Barth, and K. Kern, "Mobility and bonding transition of C60 on Pd(110)," *Physical Review B* 64, no. 16 (2001): 161403.
- ¹⁰⁰ J. Weckesser, J. V. Barth, and K. Kern, "Mobility and bonding transition of C60 on Pd(110)," *Physical Review B* 64, no. 16 (2001): 161403.
- ¹⁰¹ W. Fan, X. G. Gong, and W. M. Lau, "Rolling: A fast diffusion mechanism for small clusters on a solid surface," *Physical Review B* 60, no. 15 (October 15, 1999): 10727.
- ¹⁰² J. Weckesser, J. V. Barth, and K. Kern, "Mobility and bonding transition of C60 on Pd(110)," *Physical Review B* 64, no. 16 (2001): 161403.
- ¹⁰³ M Stengel, A De Vita, and A Baldereschi, "Adatom-vacancy mechanisms for the C60/Al(111)-(6 x 6) reconstruction," *Physical Review Letters* 91, no. 16 (October 17, 2003): 166101.
- ¹⁰⁴ Roberto Felici et al., "X-ray-diffraction characterization of Pt(111) surface nanopatterning induced by C60 adsorption," *Nat Mater* 4, no. 9 (2005): 688-692.
- ¹⁰⁵ N. Néel, J. Kröger, and R. Berndt, "Fullerene nanowires on a vicinal gold surface," *Applied Physics Letters* 88, no. 16 (2006): 163101.
- ¹⁰⁶ Eric I. Altman and Richard J. Colton, "Interaction of C60 with the Au(111) $23 \times [\text{square root of } 3]$ reconstruction," *Journal of Vacuum Science & Technology B* 12, no. 3 (May 0, 1994): 1906-1909.

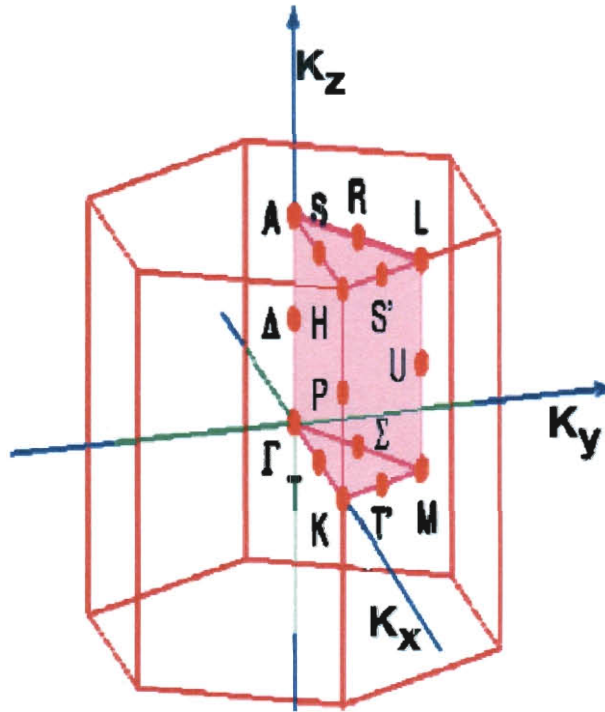
- ¹⁰⁷ Eric I. Altman and Richard J. Colton, "The interaction of C60 with noble metal surfaces," *Surface Science* 295, no. 1-2 (September 20, 1993): 13-33.
- ¹⁰⁸ Roberto Felici et al., "X-ray-diffraction characterization of Pt(111) surface nanopatterning induced by C60 adsorption," *Nat Mater* 4, no. 9 (2005): 688-692.
- ¹⁰⁹ Eric I. Altman and Richard J. Colton, "The interaction of C60 with noble metal surfaces," *Surface Science* 295, no. 1-2 (September 20, 1993): 13-33.
- ¹¹⁰ Song Guo et al., "Thermal Diffusion of C60 Molecules and Clusters on Au(111)," *The Journal of Physical Chemistry B* 108, no. 37 (2004): 14074-14081.
- ¹¹¹ Yukiumi Kita et al., "Study on the intermolecular interaction of C60 and simulations on the orientational properties of C60 in crystals," *The Journal of Chemical Physics* 125, no. 3 (2006): 034506.
- ¹¹² Song Guo et al., "Thermal Diffusion of C60 Molecules and Clusters on Au(111)," *The Journal of Physical Chemistry B* 108, no. 37 (2004): 14074-14081.
- ¹¹³ Eric I. Altman and Richard J. Colton, "Interaction of C60 with the Au(111) $23 \times [\text{square root of}]3$ reconstruction," *Journal of Vacuum Science & Technology B* 12, no. 3 (May 0, 1994): 1906-1909.
- ¹¹⁴ Grazyna Antczak and Przemyslaw Jóźwik, "Atom Movement on a Dislocated Surface," *Langmuir* 24, no. 18 (2008): 9970-9973.
- ¹¹⁵ Shi-Cai Wang and T.T. Tsong, "Measurement of the barrier height of the reflective W {110} plane boundaries in surface diffusion of single atoms," *Surface Science* 121, no. 1 (September 1, 1982): 85-97.
- ¹¹⁶ Gert Ehrlich, "Atomic View of Surface Self-Diffusion: Tungsten on Tungsten," *The Journal of Chemical Physics* 44, no. 3 (1966): 1039.
- ¹¹⁷ Richard L. Schwoebel, "Step Motion on Crystal Surfaces," *Journal of Applied Physics* 37, no. 10 (1966): 3682.
- ¹¹⁸ Yina Mo et al., "Electronic Nature of Step-Edge Barriers against Adatom Descent on Transition-Metal Surfaces," *Physical Review Letters* 101, no. 21 (November 20, 2008): 216101.
- ¹¹⁹ Eric I. Altman and Richard J. Colton, "Determination of the orientation of C60 adsorbed on Au(111) and Ag(111)," *Physical Review B* 48, no. 24 (December 15, 1993): 18244.
- ¹²⁰ Kumi Motai et al., "C60 Grown on the Cu(111)1x1 Surface," *Japanese Journal of Applied Physics* 32, no. Part 2, No. 3B (3, 1993): L450-L453.
- ¹²¹ J. I. Pascual et al., "Seeing molecular orbitals," *Chemical Physics Letters* 321, no. 1-2 (April 21, 2000): 78-82.
- ¹²² Tomihiro Hashizume et al., "Intramolecular structures of C60 molecules adsorbed on the Cu(111)-(1 x 1) surface," *Physical Review Letters* 71, no. 18 (November 1, 1993): 2959.
- ¹²³ Philippe Sautet, "Images of Adsorbates with the Scanning Tunneling Microscope: Theoretical Approaches to the Contrast Mechanism," *Chemical Reviews* 97, no. 4 (June 1, 1997): 1097-1116.
- ¹²⁴ Saman Alavi et al., "Current-triggered vibrational excitation in single-molecule transistors," *Chemical Physics* 281, no. 2-3 (August 1, 2002): 293-303.
- ¹²⁵ C. Zhang et al., "Spin-dependent transport through a magnetic carbon nanotube-molecule junction," *The Journal of Chemical Physics* 124, no. 20 (2006): 201107.
- ¹²⁶ Nobuhiko Kobayashi et al., "First-Principles Calculations of Quantum Transport in Single Molecule," *Japanese Journal of Applied Physics* 45 (2006): 2151-2153.
- ¹²⁷ Lucia Grüter et al., "Resonant tunnelling through a C60 molecular junction in a liquid environment," *Nanotechnology* 16, no. 10 (10, 2005): 2143-2148.
- ¹²⁸ Jeremy Taylor, Hong Guo, and Jian Wang, "Ab initio modeling of open systems: Charge transfer, electron conduction, and molecular switching of a C60 device," *Physical Review B* 63, no. 12 (March 13, 2001): 121104.
- ¹²⁹ Hongkun Park et al., "Nanomechanical oscillations in a single-C60 transistor," *Nature* 407, no. 6800 (2000): 57-60.
- ¹³⁰ Chao-Cheng Kaun, Ryan Jorn, and Tamar Seideman, "Spontaneous oscillation of current in fullerene molecular junctions," *Physical Review B* 74, no. 4 (July 13, 2006): 045415.
- ¹³¹ Philippe Sautet, "Images of Adsorbates with the Scanning Tunneling Microscope: Theoretical Approaches to the Contrast Mechanism," *Chemical Reviews* 97, no. 4 (June 1, 1997): 1097-1116.

-
- ¹³² Chao-Cheng Kaun, Ryan Jorn, and Tamar Seideman, "Spontaneous oscillation of current in fullerene molecular junctions," *Physical Review B* 74, no. 4 (July 13, 2006): 045415.
- ¹³³ M. Abel et al., "Scanning tunneling microscopy and x-ray photoelectron diffraction investigation of C60 films on Cu(100)," *Physical Review B* 67, no. 24 (June 9, 2003): 245407.
- ¹³⁴ J. I. Pascual et al., "Seeing molecular orbitals," *Chemical Physics Letters* 321, no. 1-2 (April 21, 2000): 78-82.
- ¹³⁵ M. Grobis et al., "Spatially Dependent Inelastic Tunneling in a Single Metallofullerene," *Physical Review Letters* 94, no. 13 (April 6, 2005): 136802.
- ¹³⁶ Yoshihiro Matsumoto et al., "X-ray absorption spectroscopy and magnetic circular dichroism in codeposited C60-Co films with giant tunnel magnetoresistance," *Chemical Physics Letters* 470, no. 4-6 (March 5, 2009): 244-248.
- ¹³⁷ J. Shen, J. Giergiel, and J. Kirschner, "Growth and morphology of Ni/Cu(100) ultrathin films: An in situ study using scanning tunneling microscopy," *Physical Review B* 52, no. 11 (1995): 8454.
- ¹³⁸ T. Quast et al., "Excited-state photoemission with combined laser/synchrotron pulse excitation from C[sub 60] chemisorbed on Ni(110)," *Journal of Applied Physics* 83, no. 3 (1998): 1642.
- ¹³⁹ Tomihiro Hashizume et al., "Intramolecular structures of C60 molecules adsorbed on the Cu(111)-(1 x 1) surface," *Physical Review Letters* 71, no. 18 (November 1, 1993): 2959.
- ¹⁴⁰ M. Abel et al., "Scanning tunneling microscopy and x-ray photoelectron diffraction investigation of C60 films on Cu(100)," *Physical Review B* 67, no. 24 (June 9, 2003): 245407.
- ¹⁴¹ J. Weckesser et al., "Binding and ordering of C60 on Pd(110): Investigations at the local and mesoscopic scale," *The Journal of Chemical Physics* 115, no. 19 (2001): 9001.
- ¹⁴² M. Grobis, X. Lu, and M. F. Crommie, "Local electronic properties of a molecular monolayer: C60 on Ag(001)," *Physical Review B* 66, no. 16 (October 30, 2002): 161408.
- ¹⁴³ Tomihiro Hashizume et al., "Intramolecular structures of C60 molecules adsorbed on the Cu(111)-(1 x 1) surface," *Physical Review Letters* 71, no. 18 (November 1, 1993): 2959.
- ¹⁴⁴ P. W. Murray et al., "Growth of C60 on Cu(110) and Ni(110) surfaces: C60-induced interfacial roughening," *Physical Review B* 55, no. 15 (April 15, 1997): 9360.
- ¹⁴⁵ Philippe Sautet, "Images of Adsorbates with the Scanning Tunneling Microscope: Theoretical Approaches to the Contrast Mechanism," *Chemical Reviews* 97, no. 4 (June 1, 1997): 1097-1116.
- ¹⁴⁶ Chao-Cheng Kaun, Ryan Jorn, and Tamar Seideman, "Spontaneous oscillation of current in fullerene molecular junctions," *Physical Review B* 74, no. 4 (July 13, 2006): 045415.
- ¹⁴⁷ Manabu Kiguchi et al., "Atomic and electronic structures of heteroepitaxial C60 film grown on Ni(1 1 1), Cu(1 1 1)," *Applied Surface Science* 212-213 (May 15, 2003): 101-104.
- ¹⁴⁸ M. R. C. Hunt et al., "Charge transfer and structure in C60 adsorption on metal surfaces," *Physical Review B* 51, no. 15 (April 15, 1995): 10039.
- ¹⁴⁹ P. W. Murray et al., "Growth of C60 on Cu(110) and Ni(110) surfaces: C60-induced interfacial roughening," *Physical Review B* 55, no. 15 (April 15, 1997): 9360.
- ¹⁵⁰ M. Abel et al., "Scanning tunneling microscopy and x-ray photoelectron diffraction investigation of C60 films on Cu(100)," *Physical Review B* 67, no. 24 (June 9, 2003): 245407.
- ¹⁵¹ J. Shen, J. Giergiel, and J. Kirschner, "Growth and morphology of Ni/Cu(100) ultrathin films: An in situ study using scanning tunneling microscopy," *Physical Review B* 52, no. 11 (1995): 8454.
- ¹⁵² E. Kopatzki et al., "Homoepitaxial growth on Ni(100) and its modification by a preadsorbed oxygen adlayer," *Surface Science* 284, no. 1-2 (March 10, 1993): 154-166.
- ¹⁵³ M. C. Bartelt and J. W. Evans, "Transition to Multilayer Kinetic Roughening for Metal (100) Homoepitaxy," *Physical Review Letters* 75, no. 23 (December 4, 1995): 4250.
- ¹⁵⁴ E. Kopatzki et al., "Homoepitaxial growth on Ni(100) and its modification by a preadsorbed oxygen adlayer," *Surface Science* 284, no. 1-2 (March 10, 1993): 154-166.
- ¹⁵⁵ M. C. Bartelt and J. W. Evans, "Transition to Multilayer Kinetic Roughening for Metal (100) Homoepitaxy," *Physical Review Letters* 75, no. 23 (December 4, 1995): 4250.
- ¹⁵⁶ M. P. Seah and W. A. Dench, "Quantitative electron spectroscopy of surfaces: A standard data base for electron inelastic mean free paths in solids," *Surface and Interface Analysis* 1, no. 1 (1979): 2-11.

- [¹⁵⁷] A. Goldoni et al., "C70 adsorbed on Cu(111): Metallic character and molecular orientation," *The Journal of Chemical Physics* 116, no. 17 (2002): 7685.
- [¹⁵⁸] J. Weckesser et al., "Binding and ordering of C60 on Pd(110): Investigations at the local and mesoscopic scale," *The Journal of Chemical Physics* 115, no. 19 (2001): 9001.
- [¹⁵⁹] Joachim Stöhr, *NEXAFS spectroscopy* (Springer, 1992).
- [¹⁶⁰] T. R. Ohno et al., "C60 bonding and energy-level alignment on metal and semiconductor surfaces," *Physical Review B* 44, no. 24 (December 15, 1991): 13747.
- [¹⁶¹] V. Saltas and C. A. Papageorgopoulos, "Adsorption and decomposition of C60 on Ni(1 1 0) surfaces," *Surface Science* 488, no. 1-2 (August 1, 2001): 23-31.
- [¹⁶²] Farid El Gabaly et al., "Structure and morphology of ultrathinCo/Ru(0001) films," *New Journal of Physics* 9, no. 3 (3, 2007): 80-80.
- [¹⁶³] E. Lundgren et al., "Thin films of Co on Pt(111): Strain relaxation and growth," *Physical Review B* 62, no. 4 (July 15, 2000): 2843.
- [¹⁶⁴] L. Diekhoner et al., "Surface States of Cobalt Nanoislands on Cu(111)," *Physical Review Letters* 90, no. 23 (June 10, 2003): 236801.
- [¹⁶⁵] O. Pietzsch et al., "Spin-Polarized Scanning Tunneling Spectroscopy of Nanoscale Cobalt Islands on Cu(111)," *Physical Review Letters* 92, no. 5 (February 6, 2004): 057202.
- [¹⁶⁶] J. Wiebe et al., "Scanning tunneling spectroscopy on Co(0001): Spectroscopic signature of stacking faults and dislocation lines," *Physical Review B* 70, no. 3 (July 8, 2004): 035404.
- [¹⁶⁷] Raghani Pushpa and Shobhana Narasimhan, "Reconstruction of Pt(111) and domain patterns on close-packed metal surfaces," *Physical Review B* 67, no. 20 (May 23, 2003): 205418.
- [¹⁶⁸] A. Bauer et al., "Morphology and Curie Temperature Changes Upon Annealing of Co/W(110)," *Mater. Res. Soc. Symp. Proc.* 475 (1997).
- [¹⁶⁹] Ohring, Milton, *Materials Science of Thin Films, Second Edition* (Academic Press 2001).
- [¹⁷⁰] Jakob Bork et al., "Potential energy landscape of metallic Moiré patterns," *New Journal of Physics* 11, no. 11 (11, 2009): 113051.
- [¹⁷¹] Joachim Jacobsen et al., "Island Shape-Induced Transition from 2D to 3D Growth for Pt/Pt(111)," *Physical Review Letters* 74, no. 12 (March 20, 1995): 2295.
- [¹⁷²] Staffan Ovesson, Alexander Bogicevic, and Bengt I. Lundqvist, "Origin of Compact Triangular Islands in Metal-on-Metal Growth," *Physical Review Letters* 83, no. 13 (1999): 2608.
- [¹⁷³] Farid El Gabaly et al., "Structure and morphology of ultrathinCo/Ru(0001) films," *New Journal of Physics* 9, no. 3 (3, 2007): 80-80.
- ¹⁷⁴ C. Cepek, A. Goldoni, and S. Modesti, "Chemisorption and fragmentation of C60 on Pt(111) and Ni(110)," *Physical Review B* 53, no. 11 (March 15, 1996): 7466.
- ¹⁷⁵ C.H. Lin et al., "Anomalous Surface Diffusion of C60 and Anisotropic Growth of Nano Islands on Ni(111)," *Journal of Nanoscience and Nanotechnology* 8 (February 2008): 602-607.
- ¹⁷⁶ Ding-sheng Wang, Ruqian Wu, and A. J. Freeman, "Magnetocrystalline anisotropy of Co-Pd interfaces," *Physical Review B* 48, no. 21 (December 1, 1993): 15886.
- ¹⁷⁷ Patrick Bruno, "Tight-binding approach to the orbital magnetic moment and magnetocrystalline anisotropy of transition-metal monolayers," *Physical Review B* 39, no. 1 (January 1, 1989): 865.
- ¹⁷⁸ D. Givord et al., "Interface magnetic anisotropy," *Journal of Magnetism and Magnetic Materials* 157-158 (May 2, 1996): 245-249.
- ¹⁷⁹ J. Wiebe et al., "Scanning tunneling spectroscopy on Co(0001): Spectroscopic signature of stacking faults and dislocation lines," *Physical Review B* 70, no. 3 (July 8, 2004): 035404.
- ¹⁸⁰ S. N. Okuno, T. Kishi, and K. Tanaka, "Spin-Polarized Tunneling Spectroscopy of Co(0001) Surface States," *Physical Review Letters* 88, no. 6 (January 25, 2002): 066803.
- ¹⁸¹ L. Diekhoner et al., "Surface States of Cobalt Nanoislands on Cu(111)," *Physical Review Letters* 90, no. 23 (June 10, 2003): 236801.
- ¹⁸² O. Pietzsch et al., "Spin-Polarized Scanning Tunneling Spectroscopy of Nanoscale Cobalt Islands on Cu(111)," *Physical Review Letters* 92, no. 5 (February 6, 2004): 057202.

-
- ¹⁸³ J. Wiebe et al., "Scanning tunneling spectroscopy on Co(0001): Spectroscopic signature of stacking faults and dislocation lines," *Physical Review B* 70, no. 3 (July 8, 2004): 035404.
- ¹⁸⁴ Farid El Gabaly et al., "Structure and morphology of ultrathinCo/Ru(0001) films," *New Journal of Physics* 9, no. 3 (3, 2007): 80-80.
- ¹⁸⁵ Jakob Bork et al., "Potential energy landscape of metallic Moiré patterns," *New Journal of Physics* 11, no. 11 (11, 2009): 113051.
- ¹⁸⁶ J. Enkovaara, D. Wortmann, and S. Blugel, "Spin-polarized tunneling between an antiferromagnet and a ferromagnet: First-principles calculations and transport theory," *Physical Review B* 76, no. 5 (2007): 054437.
- ¹⁸⁷ J. Enkovaara, D. Wortmann, and S. Blugel, "Spin-polarized tunneling between an antiferromagnet and a ferromagnet: First-principles calculations and transport theory," *Physical Review B* 76, no. 5 (2007): 054437.
- ¹⁸⁸ T. Kishi et al., "Spin-dependent electronic structure and theoretical SP-STM images for Co(0001) film," *IEEE Transactions on Magnetics* 36, no. 5 (September 2000): 2972-2974.
- ¹⁸⁹ K. Baberschke, M. Donath, and W. Nolting, *Band-Ferromagnetism*, 1st ed. (Springer, 2001).
- ¹⁹⁰ J. de la Figuera et al., "Determination of buried dislocation structures by scanning tunneling microscopy," *Physical Review B* 63, no. 16 (April 6, 2001): 165431.
- ¹⁹¹ Farid El Gabaly et al., "The Importance of Threading Dislocations on the Motion of Domain Boundaries in Thin Films," *Science* 308, no. 5726 (May 27, 2005): 1303-1305.
- ¹⁹² W. L. Ling et al., "Strain Relief through Heterophase Interface Reconstruction: Ag(111)/Ru(0001)," *Physical Review Letters* 92, no. 11 (March 18, 2004): 116102.
- ¹⁹³ J. Wiebe et al., "Scanning tunneling spectroscopy on Co(0001): Spectroscopic signature of stacking faults and dislocation lines," *Physical Review B* 70, no. 3 (July 8, 2004): 035404.
- ¹⁹⁴ Y. Yayon, Xinghua Lu, and M. F. Crommie, "Bimodal electronic structure of isolated Co atoms on Pt(111)," *Physical Review B* 73, no. 15 (April 3, 2006): 155401.
- ¹⁹⁵ Y. Yayon et al., "Observing Spin Polarization of Individual Magnetic Adatoms," *Physical Review Letters* 99, no. 6 (2007): 067202.
- ¹⁹⁶ O. Pietzsch et al., "Spin-Polarized Scanning Tunneling Spectroscopy of Nanoscale Cobalt Islands on Cu(111)," *Physical Review Letters* 92, no. 5 (February 6, 2004): 057202.
- ¹⁹⁷ J. Wiebe et al., "Scanning tunneling spectroscopy on Co(0001): Spectroscopic signature of stacking faults and dislocation lines," *Physical Review B* 70, no. 3 (July 8, 2004): 035404.
- ¹⁹⁸ U. Bauer et al., "Effect of step decoration on the spin reorientation of Ni films grown on vicinal Cu(001)," *Physical Review B* 76, no. 18 (November 14, 2007): 184415.
- ¹⁹⁹ U. Bovensiepen, Hyuk J. Choi, and Z. Q. Qiu, "Step-induced magnetic anisotropy in vicinal Ni/Cu(001) and its effect on the spin-reorientation transition," *Physical Review B* 61, no. 5 (February 1, 2000): 3235.
- ²⁰⁰ Sarnjeet S. Dhesi et al., "Anisotropic Spin-Orbit Coupling and Magnetocrystalline Anisotropy in Vicinal Co Films," *Physical Review Letters* 87, no. 6 (July 18, 2001): 067201.
- ²⁰¹ J. Wiebe et al., "Scanning tunneling spectroscopy on Co(0001): Spectroscopic signature of stacking faults and dislocation lines," *Physical Review B* 70, no. 3 (July 8, 2004): 035404.
- ²⁰² Farid El Gabaly et al., "Noble metal capping effects on the spin-reorientation transitions of Co/Ru(0001)," *New Journal of Physics* 10, no. 7 (7, 2008): 073024.
- ²⁰³ Farid El Gabaly et al., "Imaging Spin-Reorientation Transitions in Consecutive Atomic Co Layers on Ru(0001)," *Physical Review Letters* 96, no. 14 (April 11, 2006): 147202.
- ²⁰⁴ S. Blugel, M. Weinert, and P. H. Dederichs, "Ferromagnetism and antiferromagnetism of 3d-metal overlayers on metals," *Physical Review Letters* 60, no. 11 (March 14, 1988): 1077.
- ²⁰⁵ Farid El Gabaly et al., "Structure and morphology of ultrathinCo/Ru(0001) films," *New Journal of Physics* 9, no. 3 (3, 2007): 80-80.
- ²⁰⁶ B. A. Parkinson et al., "Periodic lattice distortions as a result of lattice mismatch in epitaxial films of two-dimensional materials," *Applied Physics Letters* 58, no. 5 (1991): 472.
- ²⁰⁷ Tomihiro Hashizume et al., "Intramolecular structures of C60 molecules adsorbed on the Cu(111)-(1 x 1) surface," *Physical Review Letters* 71, no. 18 (November 1, 1993): 2959.

-
- ²⁰⁸ J. I. Pascual et al., "Seeing molecular orbitals," *Chemical Physics Letters* 321, no. 1-2 (April 21, 2000): 78-82.
- ²⁰⁹ Eric I. Altman and Richard J. Colton, "Determination of the orientation of C60 adsorbed on Au(111) and Ag(111)," *Physical Review B* 48, no. 24 (December 15, 1993): 18244.
- ²¹⁰ M. Abel et al., "Scanning tunneling microscopy and x-ray photoelectron diffraction investigation of C60 films on Cu(100)," *Physical Review B* 67, no. 24 (June 9, 2003): 245407.
- ²¹¹ Saman Alavi et al., "Current-triggered vibrational excitation in single-molecule transistors," *Chemical Physics* 281, no. 2-3 (August 1, 2002): 293-303.
- ²¹² Philippe Sautet, "Images of Adsorbates with the Scanning Tunneling Microscope: Theoretical Approaches to the Contrast Mechanism," *Chemical Reviews* 97, no. 4 (June 1, 1997): 1097-1116.
- ²¹³ J. Wiebe et al., "Scanning tunneling spectroscopy on Co(0001): Spectroscopic signature of stacking faults and dislocation lines," *Physical Review B* 70, no. 3 (July 8, 2004): 035404.
- ²¹⁴ D. Drakova, M. Nedjalkova, and G. Doyen, "Theory of tip-dependent imaging of adsorbates in the STM: CO on Cu(111)," *International Journal of Quantum Chemistry* 106, no. 6 (2006): 1419-1431.
- ²¹⁵ L. Bartels, G. Meyer, and K. -H. Rieder, "High-resolution spectroscopy of weakly chemisorbed species using a low-temperature scanning tunneling microscope (STM): CO/Cu(111)," *Chemical Physics Letters* 297, no. 3-4 (November 27, 1998): 287-292.
- ²¹⁶ Norbert Memmel, "Monitoring and modifying properties of metal surfaces by electronic surface states," *Surface Science Reports* 32, no. 3-4 (1998): 91-163.
- ²¹⁷ Kenta Amemiya et al., "O K-edge x-ray magnetic circular dichroism of atomic O adsorbed on an ultrathin Co/Cu(100) film: Comparison with molecular CO on Co/Cu(100)," *Physical Review B* 64, no. 13 (2001): 132405.
- ²¹⁸ D Arvanitis et al., "Magnetic X-ray circular dichroism on in situ grown 3d magnetic thin films on surfaces," *Journal of Synchrotron Radiation* 8, no. Pt 2 (March 1, 2001): 120-124.
- ²¹⁹ Kenta Amemiya et al., "O K-edge x-ray magnetic circular dichroism of atomic O adsorbed on an ultrathin Co/Cu(100) film: Comparison with molecular CO on Co/Cu(100)," *Physical Review B* 64, no. 13 (2001): 132405.
- ²²⁰ Norbert Memmel, "Monitoring and modifying properties of metal surfaces by electronic surface states," *Surface Science Reports* 32, no. 3-4 (1998): 91-163.
- ²²¹ Joachim Stöhr, *NEXAFS spectroscopy* (Springer, 1992).
- ²²² Ló et al., "Induced Ring Currents in Polymerized C60 and C70 Molecules," *Journal of Computational and Theoretical Nanoscience* 4 (April 2007): 257-263.
- ²²³ V. Lebedev et al., "Magnetic-field-induced slowing-down of molecular rotation in C60 crystals," *Physics of the Solid State* 44, no. 4 (April 17, 2002): 641-643.
- ²²⁴ B. G. Briner et al., "Charge-density oscillations on Be(1010): Screening in a non-free two-dimensional electron gas," *Physical Review B* 58, no. 20 (November 15, 1998): 13931.
- ²²⁵ O. Yu. Kolesnychenko et al., "Real-space imaging of an orbital Kondo resonance on the Cr(001) surface," *Nature* 415, no. 6871 (January 31, 2002): 507-509.
- ²²⁶ K. von Bergmann et al., "Spin-Polarized Electron Scattering at Single Oxygen Adsorbates on a Magnetic Surface," *Physical Review Letters* 92, no. 4 (January 27, 2004): 046801.



Symmetry Point	Description	Recip. Lattice Coordinates
Γ	Center of Brillouin zone	0
A	Center of hexagonal face	$1/2 \cdot \mathbf{b}_3$
H	Corner point	$1/3 \cdot \mathbf{b}_1 + 1/3 \cdot \mathbf{b}_2 + 1/2 \cdot \mathbf{b}_3$
K	Middle of edge joining 2 rectangular faces	$1/3 \cdot \mathbf{b}_1 + 1/3 \cdot \mathbf{b}_2$
L	Middle of edge joining a hexagonal & rectangular face	$1/2 \cdot \mathbf{b}_2 + 1/2 \cdot \mathbf{b}_3$
M	Center of rectangular face	$1/2 \cdot \mathbf{b}_2$

Information obtained from <http://cst-www.nrl.navy.mil/users/mehl/phonons/hcp/>

Appendix B

C₆₀ line spacing & height calculations:

C₆₀ on 3rd ML Co moiré terrace

	Area (nm ²)	Center (nm)	Width (nm)	Height (Counts)	
1	5.23342	8.940943	0.876309	3.801969	11.27626
2	11.69063	7.813317	1.205626	6.17313	10.19507
3	10.86339	6.79381	1.460027	4.736795	9.749469
4	8.20349	5.818863	1.146675	4.554476	8.656336
5	5.124801	4.953229	1.020685	3.196432	10.04452
6	15.03545	3.948777	1.530543	6.253903	
1	9.626431	1.711481	1.044552	7.35318	13.41832
2	12.30192	3.053313	1.291994	7.597181	9.120516
3	3.744149	3.965365	0.634798	4.706059	7.113345
4	4.98787	4.676699	0.668188	5.956025	8.865337
5	9.363086	5.563233	0.994849	7.50934	12.33222
6	11.13941	6.796456	1.133721	7.839639	10.63093
7	3.53235	7.859549	0.597155	4.719722	
1	10.18106	2.319762	1.114058	5.817888	11.57523
2	14.95344	3.477285	1.660639	5.732526	11.12691
3	9.015963	4.589977	1.252814	4.58148	9.43065
4	5.813797	5.533042	1.030943	3.590091	9.277509
5	10.38329	6.460793	1.286669	5.137457	
					10.18751 average spacing
					1.539314 std. dev.

C₆₀ on Ru(0001) Substrate Surface

	Area (nm ²)	Center (nm)	Width (nm)	Height (Counts)	
1	41.41965	1.870427	2.711108	9.726122	10.10661
2	13.55822	2.881088	6.14E-04	14062.98	10.33661
3	24.41762	3.914749	1.880467	8.266428	
1	12.6719	3.052589	1.479301	6.834792	10.3421
2	1.257734	4.086799	0.465633	2.155185	10.35401
3	12.84791	5.122201	1.439328	7.122177	
1	13.16995	1.624758	1.376362	7.63469	11.89386
2	4.813173	2.814144	0.744484	5.158411	7.91114
3	3.887035	3.605258	0.685	4.527599	10.83254
4	13.06864	4.688512	1.448015	7.201075	12.28667
5	6.008805	5.917179	0.832008	5.762362	
1	15.97844	1.508956	1.459052	6.971776	11.9944
2	11.5856	2.7084	1.406891	5.242498	9.35768
3	4.055402	3.644168	0.840252	3.07259	10.2354
4	20.16933	4.667707	1.904161	6.743228	11.3399
5	9.674651	5.801697	0.999702	6.160907	
				10.5081	average spacing
				1.176735	std. dev.

C₆₀ along Bottom Terrace of Co-Ru step edge

	Area (nm ²)	Center (nm)	Width (nm)	Height (Counts)	
1	11.19036	1.791874	1.079263	6.600805	11.17638
2	16.20622	2.909512	1.616204	6.383601	10.23393
3	4.265204	3.932905	0.896823	3.027701	10.94695
4	24.33012	5.0276	2.073559	7.469782	
1	24.42554	1.139929	1.664011	11.71192	12.91044
2	6.712781	2.430973	0.721081	7.42777	7.93074
3	3.599641	3.224047	0.475237	6.043513	
1	9.659216	1.598654	1.217598	6.329623	10.66716
2	3.931746	2.66537	0.749463	4.18577	10.51273
3	9.148216	3.716643	1.130691	6.455538	10.52313
4	3.226875	4.768956	0.637359	4.039598	
1	12.06521	0.435702	1.093893	8.80035	12.25565
2	7.40773	1.661267	0.74264	7.958784	8.31863
3	3.970786	2.49313	0.490723	6.456254	10.69012
4	12.96601	3.562142	1.172248	8.825247	
					10.56053 average spacing
					1.449293 std. dev.

C₆₀ along Bottom Terrace of Co step edge

	Area (nm ²)	Center (nm)	Width (nm)	Height (Counts)	
1	21.97257	1.847652	1.988185	7.035651	13.5385
2	9.299991	3.201502	1.256308	4.712665	10.24191
3	8.953148	4.225693	0.90364	6.307546	
1	12.08745	2.206914	1.291498	7.467596	8.7655
2	14.21146	3.083464	1.520917	5.948579	8.751525
3	11.79527	3.958617	1.212787	7.760028	
1	14.94202	1.936254	1.282479	7.41719	12.72709
2	15.78768	3.208963	1.332133	7.544855	
1	8.894543	2.44717	0.997754	7.112796	12.74017
2	9.28755	3.721186	0.999438	7.41456	
					11.12745 average spacing
					2.143868 std. dev.

C₆₀ and Co(0001) Film Height Data

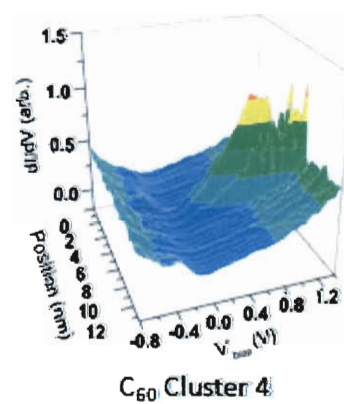
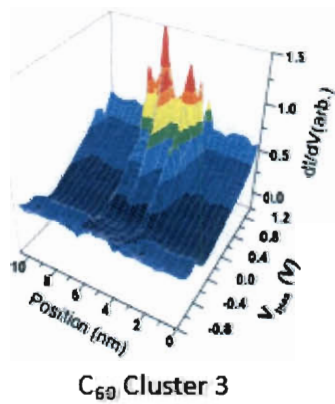
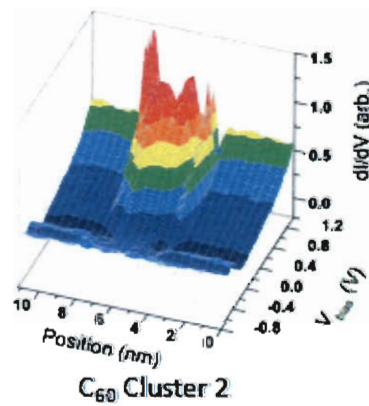
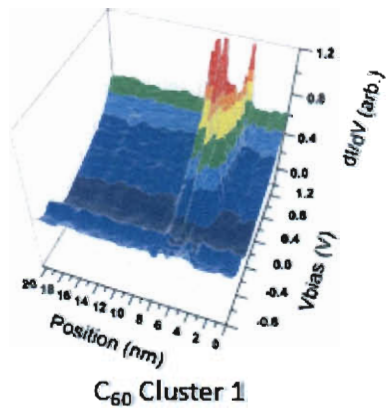
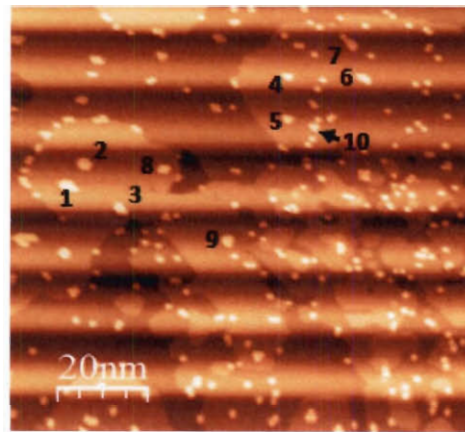
		Area (nm ²)	Center (nm)	Width (nm)	Height (Counts)		
ratio:		1	267.866	0.182432	0.103447	2066.042	Co1-unrecon
88.81013	hcp	2	58.17974	0.233591	0.022357	2076.33	Co1-recon1
11.18987	fcc	3	7.33051	0.29606	0.01149	599.405	Co1-recon2
77.79289	hcp	4	596.9258	0.398871	0.081295	5858.649	Co2-recon1
22.20711	fcc	5	170.4011	0.446464	0.048597	2797.732	Co2-recon2
		6	847.5597	0.641352	0.096463	7010.505	Co3
		7	73.66092	0.85549	0.06281	1101.755	C ₆₀ -Co1-unrecon
		8	674.3134	0.97719	0.068466	7858.22	C ₆₀ -Co1-recon2
		9	258.8821	1.087728	0.277759	593.3549	C ₆₀ -Co2-recon1
		10	65.33146	1.334298	0.181537	229.1065	C ₆₀ -Co3
		11	16.28859	1.637926	0.075095	138.0867	ignore (streaks in image)

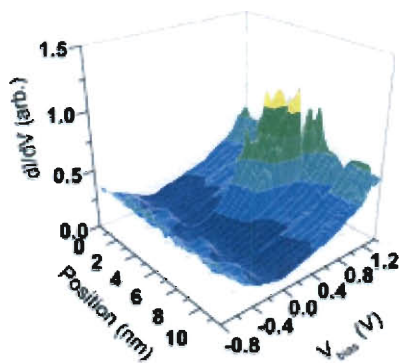
Percent of C₆₀ on each Co Monolayer

Layer	% Total Area	#C ₆₀	C ₆₀ -MLs
Ru	9.7%	56	0.0468
Co-1	32.3%	224	0.0564
Co-2	30.7%	191	0.0507
Co-3	27.3%	90	0.0269

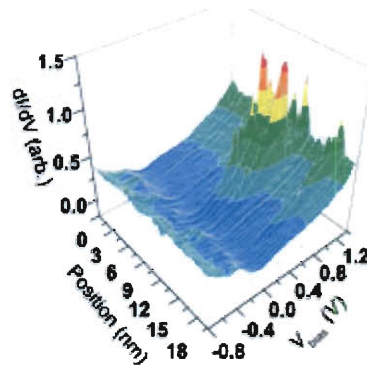
Appendix C

Line Sections taken from different locations on spin-polarized spectral map of C₆₀ on Co(0001).

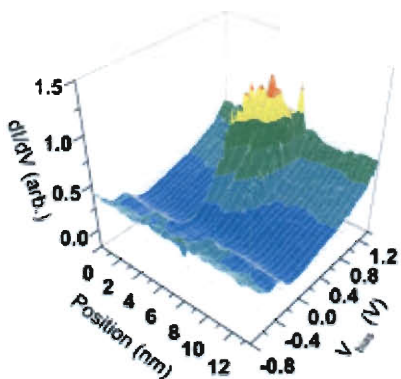




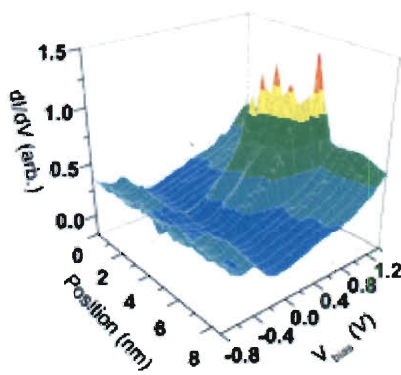
C_{60} Cluster 5



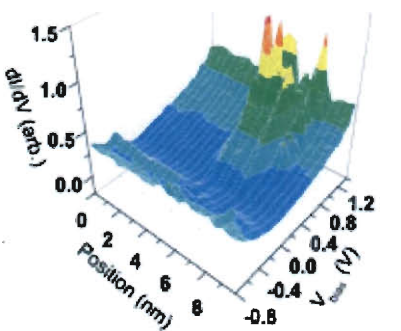
C_{60} Cluster 6



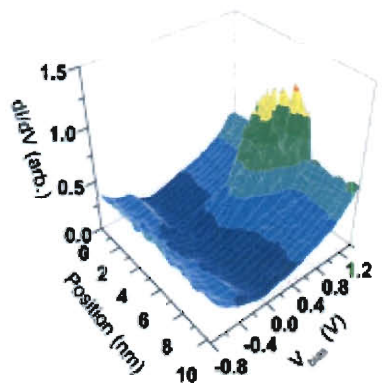
C_{60} Cluster 7



C_{60} Cluster 8



C_{60} Cluster 9



C_{60} Cluster 10

Appendix D Comparison of XAS spectra for crystalline C_{60} and $C_{60}/Co/Cu(100)$

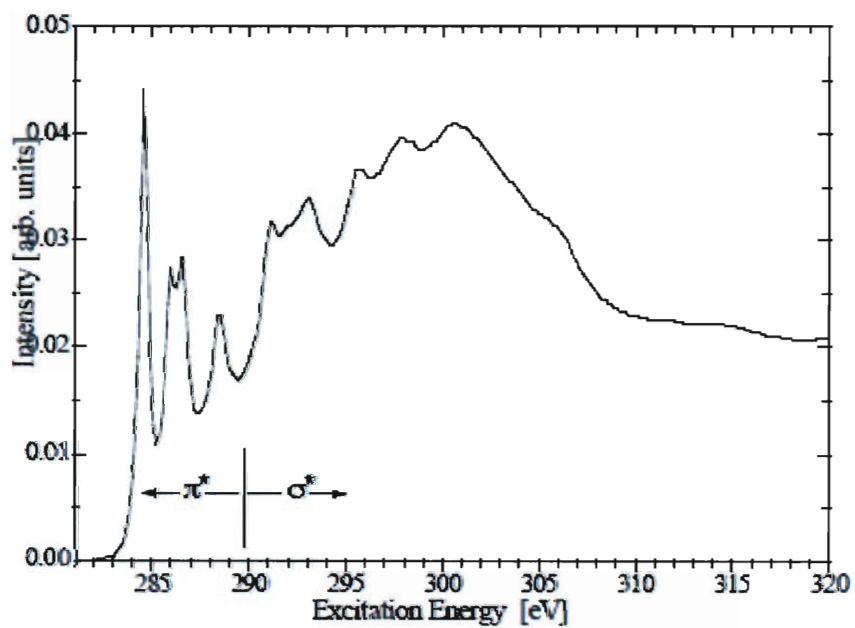


Figure D.1. X-ray absorption spectrum (XAS) for crystalline C_{60} (C, 1s-peak). The four features below 290 eV are electronic transitions to unoccupied π^* bands; features above 290 eV are transitions to unoccupied σ^* bands and vacuum. Image modified from [1].

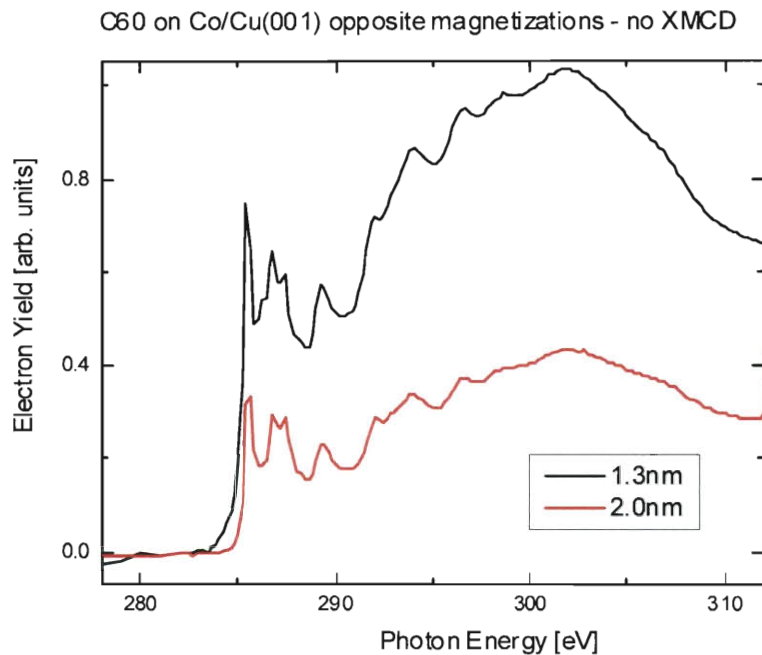


Figure D.2. Experimental X-ray absorption spectrum (XAS) data collected for the C_{60} /6-ML Co/Cu(100) (C, 1s-peak) collected by Marvin Cummings, (advisor Dr. Enrique V. Barrera), Rice University, in collaboration with Dr. Hendrick Ohldag and Dr. Dennis Nordland at the *Stanford Synchrotron Radiation Laboratory, Beamline 8-2*. As in figure C.1, the four features below 290 eV are electronic transitions to unoccupied π^* bands; features above 290 eV are transitions to unoccupied σ^* bands and vacuum. Compared with figure C.1, the π^* peaks in this figure are suppressed relative to the σ^* peaks indicating e^- charge transfer from the Co surface to C_{60} at the surface. [2]

[1] T Hamilton et al., "Determining the sp^2/sp^3 bonding concentrations of carbon films using X-ray absorption spectroscopy," *Canadian Journal of Physics* 86 (December 1, 2008): 1401-1407.

[2] Joachim Stöhr, *NEXAFS spectroscopy* (Springer, 1992).